1-1-2014

Synthesis And Characterization Of Discrete Fexni2-Xp Nanoparticles; Assembly Of Phosphide Nanoparticles Into Porous Networks

Asha Hitihami Mudiyanselage
Wayne State University,

Follow this and additional works at: http://digitalcommons.wayne.edu/oa_dissertations

Part of the Chemistry Commons

SYNTHESIS AND CHARACTERIZATION OF DISCRETE FE$_x$NI$_{2-x}$P NANOPARTICLES; ASSEMBLY OF PHOSPHIDE NANOPARTICLES INTO POROUS NETWORKS

by

ASHA HITIHAMI MUDIYANSELAGE

DISSERTATION

Submitted to the Graduate School

of Wayne State University,

Detroit, Michigan

in partial fulfillment of the requirements

for the degree of

DOCTOR OF PHILOSOPHY

2015

MAJOR: CHEMISTRY

Approved by:

_____

Advisor   Date

_____

_____

_____

DEDICATION

To my beloved parents, husband, and son

ACKNOWLEDGEMENTS

I would like to express my deepest gratitude to my advisor Prof. Stephanie L. Brock. I want to thank her for giving me the opportunity to start my research career at Wayne State University in her laboratory. Her knowledge, enthusiasm and passion for science inspired me to pursue my career in material science. She understood my competence as well as weaknesses and guided me to strengthen my skills and develop my personality. I greatly appreciate her understanding and help during difficult times. Under her guidance I grew as a professional scientist and as an individual. Once again I want to thank Dr. Stephanie L. Brock for the wonderful experience that I had in her laboratory.

I would like to thank my dissertation committee members, Prof. Matthew J. Allen, Prof. Andrés Cisneros, and Prof. Zhixian Zhou, for their valuable time, suggestions, and comments.

I want to express my deepest appreciation to my Collaborators, Prof. Mark Bussell and his group at Western Washington University for hydrodesulfurization catalytic measurements, Prof. Takela Seda at Western Washington University for Mössbauer spectroscopy measurements and data interpretation, and Prof. Gavin Lawes and Maheshika Perera in the Department of Physics and Astronomy at Wayne State University for magnetic measurements.

I am very grateful for Dr. Mie Zei for the training on transmission electron microscopy. I want to thank Dr. Mary Jane Heeg for the training on powder X-ray diffractometry. I want to thank Christopher Thrush for help with the X-ray photoelectron spectroscopy measurements and Corey Lambert for ICP-MS measurements. I would like to thank Judy Westrick for her hard work on maintaining the Lumigen instrument center in Chemistry Department. I thank Nestor Ocampo for all the support in IT related issues.

I wish them good luck. A bunch of thanks go to all the friends in Chemistry Department and Sri Lankan community.

A special thanks to my amazing family. Words cannot express how grateful I am for all the sacrifices that they made for me to come this far. Even though they lived far away they always encouraged me to do well and understood for being very busy and not spending much time with them. Finally, and most importantly, I would like to thank my beloved husband. Without him I would not have come here to pursue my graduate studies. I am grateful for his love, support, encouragement, and patience throughout these years. I want to thank my precious son for bringing happiness and meaning to my life.

TABLE OF CONTENTS

LIST OF TABLES

LIST OF FIGURES

xii

LIST OF SCHEMES

CHAPTER 1

INTRODUCTION[1]

Materials that have at least one dimension in the size range 1-100 nm are referred to nanomaterials. Due to the large surface-to-volume ratio and changes in electronic/magnetic interactions, nanocrystals exhibit distinct magnetic, catalytic, and optical properties compared to their bulk materials.[1-4] Formalized synthesis of nanoparticles dates back to 1857.[5] Sir Michael Faraday prepared the first pure gold nanoparticles by reducing a solution of gold chloride with white phosphorous. Since then, nanotechnology has played an important role in many aspects of our day-to-day life. Current research on nanomaterials is focused on the discovery of new functional materials, development of synthetic methods to prepare them with controlled size, shape, and composition, and development of assembly techniques to integrate these nanomaterials into devices while maintaining their inherent properties.

This dissertation research is focused on synthesis, characterization and assembly of metal phosphide nanoparticles of relevance to catalysis, magnetism, and optoelectronic applications. These include (1) synthesis of discrete $Fe_xNi_{2-x}P$ ternary nanocrystals, and (2) 3-dimensional nanostructures (gels and aerogels) of InP and Ni_2P. With respect to ternary phosphide nano crystals incorporation of iron into Ni_2P is purported to improve the hydrotreating catalytic properties, whereas addition of nickel to Fe_2P extends the Curie temperature (T_C) to above room temperature, an important parameter for room temperature applications such as magnetic data storage and magnetic refrigeration.[6, 7] In this work, a solution phase synthesis method for $Fe_xNi_{2-x}P$ ($0<x<2$) was developed and the reaction parameters governing phase and size were

---

[1] Portions of the text in this chapter were reprinted or adapted with permission from: *ACS Nano*, 2013, 7, 1163-1170 and *Chem. Mater*. 2014, 26, 6251-6256

systematized. Composition dependent hydrodesulfurization (HDS) catalytic activities and magnetic properties of $Fe_xNi_{2-x}P$ nanoparticles were studied and compared to bulk phases. With respect to nanoparticle integration a sol-gel method was established for assembly of phosphide nanoparticles (InP and Ni_2P) into aerogels. Also an alternative ligand-based 3-dimensional assembly method was developed for Ni_2P. InP is a direct band gap semiconductor (1.35 eV) that exhibits quantum confinement effects when prepared as sizes < 15 nm and is useful in optoelectronic applications. The connectivity and interfacial interactions with complementary components are important considerations in optoelectronic applications. On the other hand Ni_2P is an emerging catalytic material for a range of catalytic processes, [8-12] and when designing a catalyst having a high accessible surface area is a key factor.

This chapter discusses background information relevant to this dissertation research. Topics include nanoparticles and their growth in solution, metal phosphides, optical, magnetic, catalytic properties, and sol-gel assembly of nanoparticles.

1.1 Nanoparticles (NPs)

The electronic structure, optical, and magnetic properties of crystalline solids are largely impacted when size is reduced below 100 nm.[4] Due to the increase in the fraction of total atoms on the surface of NPs, which largely effects the free energy, considerable changes in thermodynamic properties have been observed. Melting point depression and solid-solid phase transition elevation are few examples.[13, 14] The increased surface-to-volume ratio of NPs leads to increase in active site densities of catalysts and therefore enhanced catalytic activities.[15] The appearance of super-paramagnetism in ferro- or ferri- magnetic NPs when size is decreased below the domain size, and surface plasmon resonance in Au NPs are other physical phenomena that arise on the nanoscale.[16, 17] With respect to semiconductors, the changes in density of states

yields quantum size effects when the size is below excitonic Bohr radius, typically < 10 nm in diameter.[4, 18] In order to effectively evaluate how particle size impacts these properties, synthetic methods that enable formation of narrowly polydisperse discrete NPs are needed.

1.2 Growth of NPs in Solution

In this dissertation research, the solution-phase arrested-precipitation (SPAP) method was employed for NP synthesis. SPAP synthesis of NPs gives excellent control over size and shape, and particle growth is controlled by the precursor reactivity and coordinating ligands.[19] A wide range of materials, from spherical nanoparticles to nanorods, nanowires, core-shell, dumbbell, and more complex morphologies have been accessed using SPAP syntheses.[19] In a typical synthesis, inorganic compounds (e.g. cadmium oxide, indium chloride) or organometallic compounds (e.g. iron(0) pentacarbonyl, Bis(1,5-cyclooctadiene)nickel(0)) are injected into a hot organic surfactant solvent.[20, 21] These organic surfactant molecules include long-chain carboxylic and phophonic acids (e.g. oleic acid, n-octadecylphosphonic acid), alkanethiols (e.g. 1-dodecanethiol), alkylphosphines (e.g. trioctylphosphine, TOP), alkylphosphine oxides (e.g. trictylphosphine oxide, TOPO), and alkylamines (e.g. hexadecylamine).[19] Trioctylphosphine is a co-solvent of choice for phosphide NP synthesis, since it provides a source of active phosphorous (i.e. it is a co-solvent and a precursor).

La Mer's model of nucleation and growth can be used to explain solution phase NC growth, as depicted in Figure 1.1.[22] The rapid injection of precursors into the hot coordinating solvent results in thermal decomposition of precursors leading to supersaturation of monomers. The supersaturation of monomers is partially relieved by the nucleation burst and growth initiation. Particle growth then proceeds by the addition of monomers to nuclei. When the monomer concentration reaches a critical concentration, known as the nucleation threshold, in

lieu of formation of new nuclei, the addition of monomers to existing nuclei becomes favorable. A further decrease in monomer concentration leads to growth of nanoparticles by Ostwald ripening. During Ostwald ripening, larger particles grow by the dissolution of high-surface energy smaller particles. According to La Mer's model, in order to achieve particle size monodispersity a high rate of nucleation, a high initial rate of growth to reduce monomer concentration below nucleation threshold, and a slow rate of nanoparticle growth are required. Longer reaction times produce larger particles due to the Ostwald ripening process.
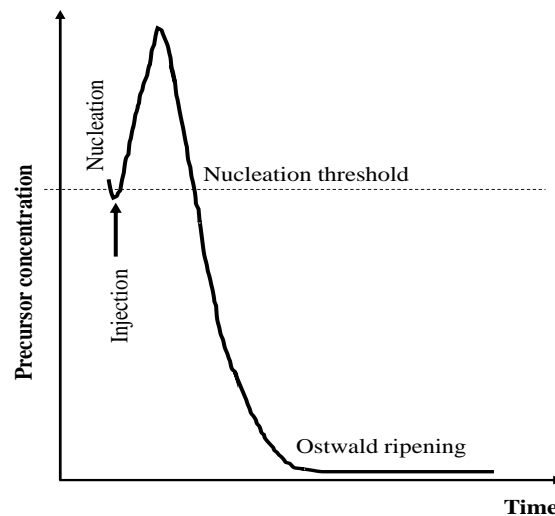
Figure 1.1 Schematic illustration of La Mer's model for nucleation and growth (adapted from Klimov)[22]

Temperature plays an important role in tuning the kinetics of nucleation and growth. The activation energy for homogenous nucleation is higher than that for particle growth. Therefore, the relative rates of nucleation and growth can be controlled by ramping the temperature.[22] Lower nucleation temperatures result in lower monomer concentration, hence larger particles.

Higher growth temperatures increase the rate of the Ostwald ripening process, yielding larger particles.

In addition to reaction temperature and time, surfactant molecules can impact the size dispersion of NCs.[19, 22] The surfactant/precursor ratio, the strength of the interactions between surfactant and monomer, and the surfactant steric bulk all effect rates of nucleation and growth. Surfactants adhere strongly to nanoparticles and inhibit the growth by passivating the surface. However, the effects of surfactants on growth kinetics are specific to the ligand surface interaction. When surfactant molecules selectively bind to different crystalline facets anisotropic structures can be generated as monomers add preferentially to the unpassivated surface.

1.3 Metal Phosphide (MP) NPs

Metal phosphides (MPs) show a wide range of properties including ferromagnetism (MnP, Fe_2P, Fe_3P), superconductivity (Rh_2P, $BaNi_2P_2$), catalysis (Co_2P, MoP, WP, Ni_2P), ability to intercalate lithium (Ni_5P_4), and semiconductivity (GaP, InP, FeP_2, MoP_2, WP_6, and CoP_8). MPs exist in a wide range of stoichiometrics (e.g. for Ni Ni_3P, Ni_5P_2, $Ni_{12}P_5$, Ni_2P, Ni_5P_4, NiP, NiP_2, and NiP_3).[21, 23-34] The reduction of the size of the materials to the nanoscale will benefit many applications including catalysis (increase in active sites due to increased surface area), lithium-ion batteries (reduced charge transport distance), and magnetic refrigeration (increase in cycling rate due to reduced thermal hysteresis).[35, 36] Due to the existence of multiple stoichiometric phases, the synthesis of nanoscale MPs is challenging. Therefore, nanoscale properties of MPs are poorly understood relative to metals, metal oxides, and chalcogenide NCs.

MP nanocrystal syntheses were first reported for semiconductors, InP and GaP.[37] This was further expanded to other phosphides including CoP_8, Fe_3P, MoP_2, Ni_2P, and WP_3.[38, 39] The development of MP nanocrystal syntheses has continued over the last two decades and several

different preparation routes are reported. These methods include; solvothermal, decomposition of aryl- or alky-phosphines in the presence of a metal precursor, and chemical vapor deposition (CVD) by the decomposition of a single precursor.[40-42]

In 2003 Brock and co-workers reported the synthesis of phase-pure FeP nanoparticles with controlled size using the SPAP method.[43] In this synthesis iron(III) acetylacetonate (Fe(acac)$_3$) was reacted with tris(trimethylsilyl)phosphine (P(SiMe$_3$)$_3$) at 240-320 °C in the presence of trioctylphosphine oxide (TOPO) as the coordinating solvent. To evaluate the effect of coordinating ligands on size and crystallinity of FeP nanoparticles, three additional capping groups have been used in the FeP synthesis. The presence of dodecylamine and myristic acid facilitated the formation of monodisperse particles at 260 °C (average size is 4.65±0.7 nm). But use of hexylphosphonic acid led to formation of smaller (1 nm) amorphous particles. The synthesis of MnP nanoparticles using a similar manner was reported by the same group using Mn$_2$(CO)$_{10}$ as the Mn precursor.[44] In this study, average particle size appeared to be sensitive to reaction temperature and time. Heating at 220 °C for 24 h resulted in formation of 5.11±0.48 nm particles, whereas heating at 250 °C for 18 h followed by heating at 220 °C for an additional 18 h produced 6.67±0.33 nm MnP particles. This preparation method was not limited to MnP, FeP and CoP nanoparticles have also been synthesized using this method.[43] An important development was the discovery that less active and less expensive alkyl-phosphines, such as trioctylphosphine (TOP), can also serve as a phosphorous source in metal phosphide synthesis. This discovery was probably inadvertent, since TOP was commonly used as a coordinating ligand in metal NP synthesis.[43]

Synthesis of Fe$_2$P nanorods via continuous delivery of iron-phosphane (Fe-TOP) complex into a hot surfactant solution (oleylamine at 300 °C) using a syringe pump was reported by

Hyeon and co-workers.[45] In this synthesis, different injection rates were employed to deliver an Fe-TOP complex, and it was observed that the rate of injection is inversely proportional to the length of the nanorods. Fe_2P nanorods with sizes of 5 x 88, 6 x 107, and 6 x 290 nm were observed for 10, 5, and 3 mL/h injection rates, respectively. These rods were formed along [001]) direction (*c* direction). The preferential growth of rods was attributed to the different binding affinities of two surfactants (oleylamine and TOP) for different facets. Later, generalized syntheses for MnP, Co_2P, FeP, and Ni_2P nanorods were reported by the same group.[46]

When TOP is used, high temperatures are required to break P-C bond and generate active 'P' for phosphide formation. However, the P-C bond cleavage in TOP can be catalyzed by metals.[37] Taking advantage of this attribute, Schaak and co-workers used a 'conversion strategy' to prepare several different MPs (Ni_2P, PtP_2, Rh_2P, Au_2P_3, Pd_5P_2, PdP_2, FeP, CoP, and AgP_2).[47, 48] They first prepared metal nanoparticles then converted these pre-formed particles into crystalline phosphide phases by reaction with TOP at 290-370 °C. This 'conversion strategy' led to formation of NPs with uniform sizes and well-defined shapes. Additionally, formation of hollow structures are reported through the Kirkendall effect, in which differences in diffusion rates of P into the particles vs. metal out of the particles results in a redistribution of the particle mass. Schaak and co-workers showed the versatility of TOP for conversion of metals into phosphides by application to metal nanoparticles; surfaces of bulk powders, foils and wires; thin films; lithographically patterned substrates, and supported NPs.[48]

Even though syntheses for many MP NPs are reported in the literature, there are few reports addressing the roles of the various synthetic parameters in determining the phases and compositions of metal phosphides until work on Fe_xP_y nanoparticle synthesis by Brock and co-workers reported in 2009.[20] In this study the preferences for two phases, FeP vs. Fe_2P, was

studied as a function of reaction temperature, time, amounts of precursors (Fe(CO)$_5$, TOP), and the sequence of the addition of these precursors. During the synthesis, pre-formed Fe particles at 200 °C were converted into iron phosphides by reacting with TOP at high temperatures (> 300 °C). The shorter reaction times favored the formation of the iron rich Fe$_2$P phase and longer reaction times resulted in FeP formation. This can be ascribed to the availability of more 'active P' at longer reaction times. When the precursor molar ratio of Fe/P was increased from 0.067 to 0.34, formation of the Fe$_2$P phase was found to dominate. In this work, optimum reaction conditions for Fe$_2$P and FeP formation are reported and the phase purity of these materials was confirmed with magnetic measurements.

In 2011 Brock and co-workers extended the Fe$_x$P$_y$ phase control strategy to systematically investigate the nickel phosphide phases Ni$_2$P and Ni$_{12}$P$_5$.[49] The 'conversion strategy' that Schaak and co-workers employed was used with variations to study the 'synthetic levers' that govern phase, size, and shape of nickel phosphides. In addition to optimizing reaction conditions for Ni$_2$P and Ni$_{12}$P$_5$ formation, the size and morphology control of these phases was carefully investigated. As the P:Ni precursor ratio increases from 0.28 to 5.6, transformation of morphology from hollow to solid particles is observed. High reaction temperature, longer heating time, and excess TOP favor the more phosphorous-rich Ni$_2$P phase over the more metal-rich phase, Ni$_{12}$P$_5$. This can be again correlated to the amount of available 'reactive P' in the reaction mixture. Use of excess oleylamine resulted in formation of metal-rich Ni$_{12}$P$_5$. Oleylamine, a primary amine, is a good reducing agent and favors formation of Ni in lower oxidation states.[50]

Carenc and co-workers observed that the rate of nucleation of Ni(0) can be increased by using excess oleylamine.[50] In their study Ni nanoparticle size decreased with increasing

oleylamine. In contrast, in the study of size controlled synthesis of Ni_2P by Brock and co-workers, the average particle size increases as the oleylamine amount increases.[15] This unexpected size increase is attributed to the use of a larger amount of TOP. When the P:Ni ratio is greater than 2.24, amorphous Ni_xP_y alloy particles form as the intermediate particles and final Ni_2P particle size is determined by these alloy particle size.[49] The presence of excess oleylamine decreases the reaction rate of TOP with Ni(0). Thus, the rate of formation of Ni_xP_y nuclei is decreased and formation of larger particles resulted.

While binary metal phosphide nanomaterials are now receiving considerable attention, ternary and quaternary phases represent even more attractive targets as the expansion of the complexity of the materials is expected to improve inherent properties. As an example, the quaternary phase $MnFeP_{1-x}As_x$ demonstrates an increased magnetocaloric effect (MCE) relative to simpler binary and ternary phases, making this more promising for magnetic refrigeration.[51-54] Additionally, introduction of a second metal into binary transition metal phosphides has also led to enhancement of Curie temperature (T_c) ($Fe_{1.95}Ni_{0.05}P$), superconductivity (ZrRuP), and increased hydrodesulfurization (HDS) and hydrodenitrogenation (HDN) catalytic activities ($Co_{0.08}Ni_2P$ and $Fe_{0.03}Ni_{1.97}P_{2.00}/SiO_2$).[55-57]

There are few reports of syntheses of ternary MP NCs. In 2008 Hyeon co-workers reported the synthesis of bimetallic iron-nickel phosphide ($Fe_{1.8}Ni_{0.2}P$, $Fe_{1.6}Ni_{0.4}P$, and $Fe_{1.5}Ni_{0.5}P$) nanorods by reacting Fe-TOP and Ni-TOP (prepared by mixing $Fe(CO)_5$/$Ni(acac)_2$ with TOP at 130 °C) at 315 °C using a continuous injection method.[58] These nanorods had a low degree of polydispersity and demonstrated composition-dependent magnetic properties (see Chapter 1.4.8). In 2011 Han and co-workers synthesized ternary NPs of $Co_{2-x}Fe_xP$.[59] The metal precursors, cobalt(II) carbonate and iron(III) acetylacetonate, were treated with oleic acid to form

metal oleates and these were heated (290 or 320 °C) with TOP before oleylamine injection. Formation of rice-shaped NCs and split nanostructures were observed at 290 and 320 °C respectively. A change in the magnetic behavior of Co_2P from paramagnetic to ferromagnetic with the incorporation of Fe is observed in ternary $Co_{2-x}Fe_xP$ (x=0.3 and 0.5). The synthesis of $Fe_{2-x}Mn_xP$ nanoparticles by the thermal decomposition of single source precursor $FeMn(CO)_8(\mu\text{-}PH_2)$ in the presence of hexadecylamine and oleic acid at 300 °C was reported by Whitmire and co-workers in 2011.[59] Below 1473 K bulk $Fe_{2-x}Mn_xP$ crystallizes in the orthorhombic structure in the range of $0.31 \leq x \leq 0.62$ and otherwise adopts hexagonal structure. The $Fe_{2-x}Mn_xP$ ($0.15 \leq x \leq 0.7$) nanocrystals crystallized in the metastable hexagonal structure and this has been attributed to the kinetically controlled synthesis of NPs giving rise to disorder of the metal.

1.4 Magnetism

Magnetism arises due to the motion of negatively charged electrons. Therefore, all materials can show magnetism but the magnitude will be different depending on the orientation of magnetic moments. Five different kinds of magnetic behaviors can be identified based on the orientation of magnetic moments and are illustrated in Figure 1.2.
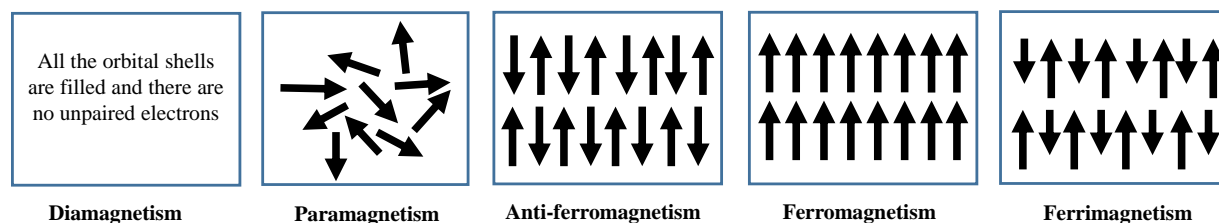
Figure 1.2 Schematic representation of magnetic moment alignments in different types of magnetism[60]

1.4.1 Diamagnetism

When all the electrons are paired, the net magnetic moment reaches zero. These kinds of materials are called diamagnetic. The magnetic susceptibility (χ), which is defined as the ratio of magnetization (M) to the field (H) is given in Equation 1.1 and for diamagnetic materials χ is very small and negative ($\sim 10^{-6}$).[60] Therefore the magnetization of diamagnetic materials as function of applied field is linear with a negative slope (Figure 1.3) and is completely reversible.

$$\chi = \frac{M}{H} \tag{1.1}$$
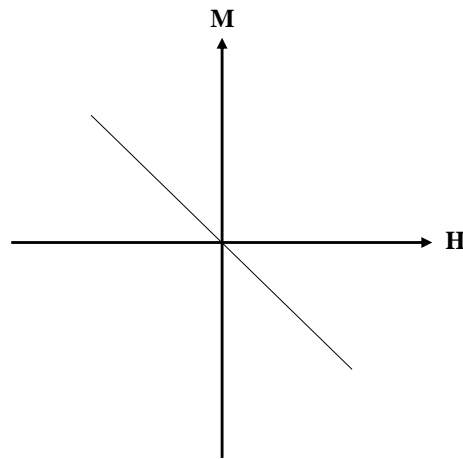
Figure 1.3 Typical curve of magnetization (M) as a function of applied magnetic field (H) for diamagnetic materials

1.4.2 Paramagnetism

Paramagnetism arises when there are unpaired electrons. The magnetic moments in a paramagnetic material are randomly oriented and when an external field is applied, a net positive magnetization results due to the partial orientation of magnetic moments (Figure 1.4). For paramagnetic materials χ is small and positive ($10^{-3} - 10^{-5}$)[60] and is inversely proportional to

temperature as shown by the Curie law (Equation 1.2), where C is the Curie constant. The plot of reciprocal susceptibility as function of temperature is given in Figure 1.5.

$$\chi = \frac{C}{T} \tag{1.2}$$
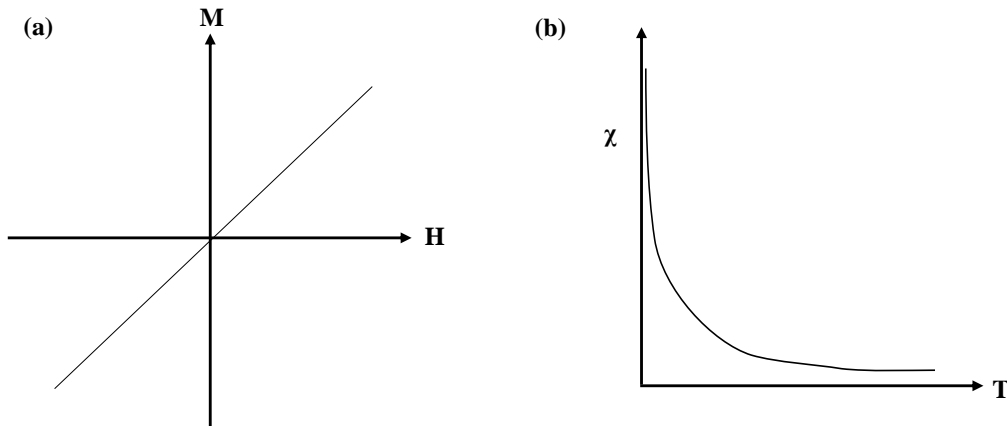
Figure 1.4 Typical curves of (a) magnetization (M) as a function of applied magnetic field (H) and (b) variation in susceptibility with temperature for paramagnetic materials
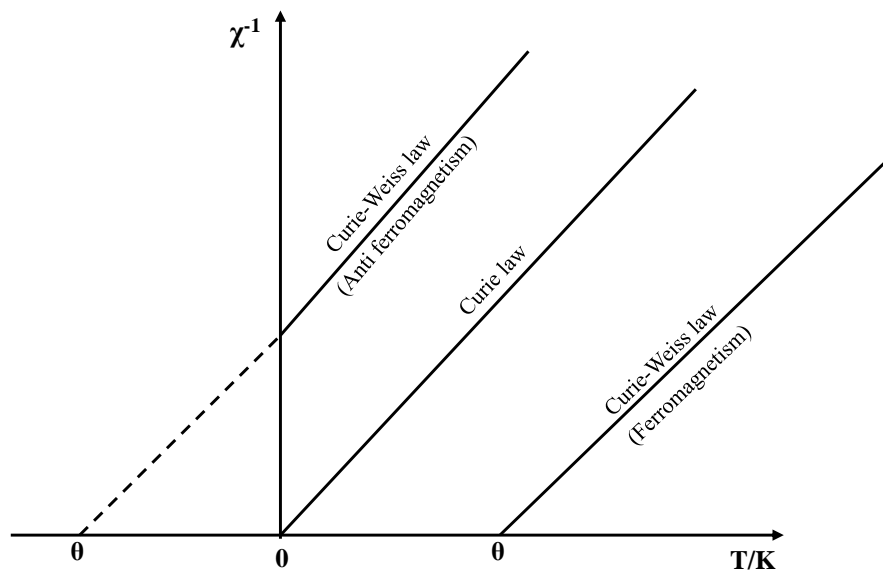
Figure 1.5 Plot of reciprocal susceptibility as a function of temperature for paramagnetic materials

1.4.3 Anti-ferromagnetism

Anti-ferromagnetism results when magnetic moments are aligned antiparallel giving rise to a zero overall magnetic moment. These materials have very small positive susceptibilities (0 - 10^{-2}) and the susceptibility increases as the temperature increases.[60] Typical magnetization vs. applied magnetic field and susceptibility as a function of temperature plots for anti-ferromagnetic materials are shown in Figure 1.6a. Like paramagnets, anti-ferromagnets show linear (positive) magnetization as a function of temperature. Above a critical temperature known as the Nèel temperature (T_N) anti-ferromagnetic materials become a paramagnetic (Figure 1.6b).
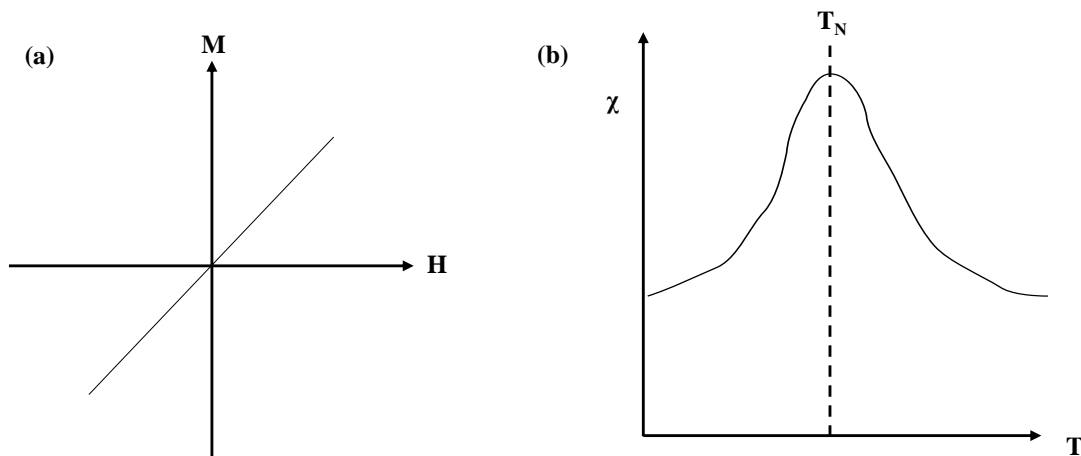
Figure 1.6 Typical magnetization and susceptibility plots for anti-ferromagnetic materials as a function of applied magnetic field and temperature

The Curie law does not take into account the interactions between adjacent moments. Therefore when there are interactions between nearby magnetic moments a modified Curie law, the Curie-Weiss law, is used for evaluating the temperature-dependent magnetization as shown in Equation 1.3, where θ is the Weiss constant. A plot of reciprocal susceptibility vs. temperature

for anti-ferromagnetic materials is linear with an x-intercept that corresponds to θ. For anti-ferromagnetic materials, θ should be negative (Figure 1.5).[60]

$$\chi = \frac{C}{T-\theta} \qquad (1.3)$$

1.4.4 Ferromagnetism

When magnetic moments interact with each other and align parallel in the same direction a large net magnetization (in the absence of an applied field) can be observed and these kinds of materials are known as ferromagnets. Iron and nickel are examples of ferromagnetic metals. Ferromagnets are the most important class of magnetic materials since they can be utilized in a range of magnetic-related applications. The magnetic susceptibilities of ferromagnetic materials are large and positive ($\chi \gg 1$) and the variation in χ as a function of temperature is given in Figure 1.7a.[60] When the thermal energy is sufficient to overcome electronic exchange the magnetic moments become randomized. The temperature at which this happens is known as the Curie temperature (T_C). Below T_C magnetic moments are ordered, and above disordered moments are present exhibiting as paramagnetic materials. Like anti-ferromagnetic materials, ferromagnets also show Curie-Weiss behavior in the paramagnetic region ($T \gg T_C$), but with a positive θ (Figure 1.5).[60]
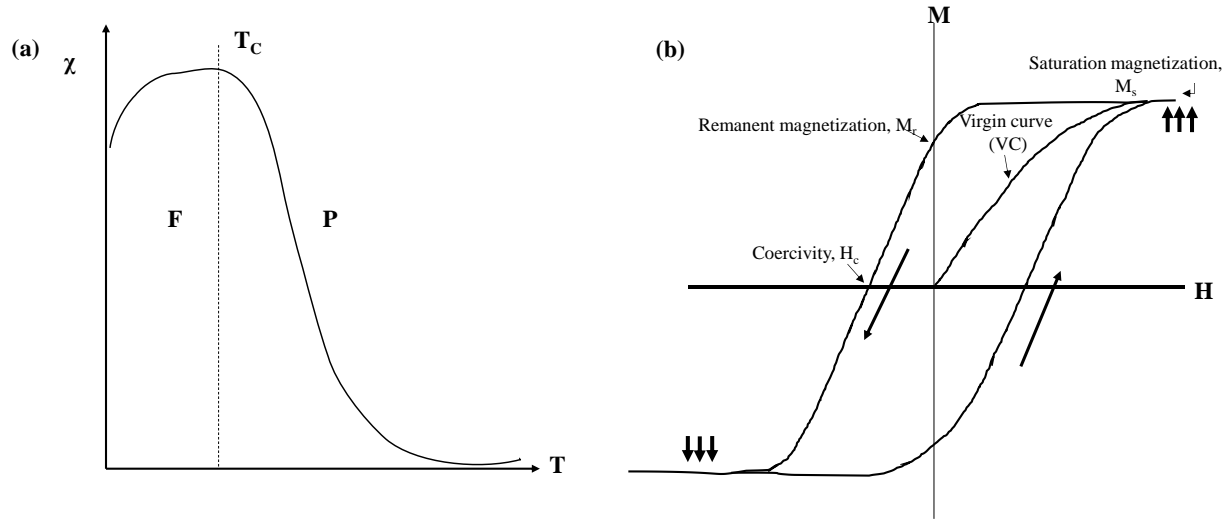
Figure 1.7 (a) The behavior of the magnetic susceptibility with temperature and (b) magnetization as a function of applied field for ferromagnetic materials

A typical magnetization vs. applied field plot for ferromagnets is shown in Figure 1.7b. As the applied field increases the magnetization increases until it reaches the saturation magnetization (M_s) and this initial curve is called the virgin curve (VC). At M_s spins are aligned with the field. As the magnitude of the applied field decreases, the magnetization decreases non linearly exhibiting hysteresis. Thus, after the removal of the external field ferromagnets can retain some degree of magnetization. The magnetization at zero field is called the remanent magnetization (M_r). The magnitude of the field that has to be applied in the opposite direction to bring the magnetization of the sample to zero is known as the coercive field (H_c). Magnetization, coercivity, and the shape of the hysteresis loop are important parameters for determining materials for magnetic applications. For example, a large remanent magnetization is required for magnetic recording applications whereas for permanent magnets a large coercivity is necessary.[17]

1.4.5 Ferrimagnetism

Ferrimagnetism occurs when unequal magnetic moments are aligned antiparallel. They exhibit ferromagnetic type behavior (spontaneous magnetization, T_C, hysteresis, and remanence), but the net magnetic moment is smaller than for ferromagnets.

1.4.6 Size Effects in Ferro- and Ferri- Magnetic Materials

1.4.6.1 Magnetic Domains

Groups of spins oriented along the same direction that behave cooperatively and are separated by domain walls from other groups are known as magnetic domains (Figure 1.8).[17] Magnetic domain walls have a characteristic width and energy associated with their formation and existence. In bulk materials reversal of magnetization occurs when domain walls migrate enabling domains oriented with the external field to grow at the expense of unaligned domains. However, as the particle size decreases the formation of domain walls becomes energetically unfavorable. Thus, particles become single domain, and once the particle size is reduced below a critical diameter (D_c) a coherent spin rotation is required to change the spin orientation. This is a higher energy process than domain wall migration. Therefore nanoparticles can show larger coercivities relative to bulk materials. However, as particle size is reduced the spins also become sensitive to thermal fluctuations giving rise to super-paramagnetism (Figure 1.9a). In the super-paramagnetic state hysteresis disappears ($H_C=0$, Figure 1.9b). The temperature at which super-paramagnetism appears is known as the blocking temperature (T_B) and is a sensitive function of the NP size and anisotropy as well as the time-scale of the measurement (i.e., T_B is frequency-dependent).
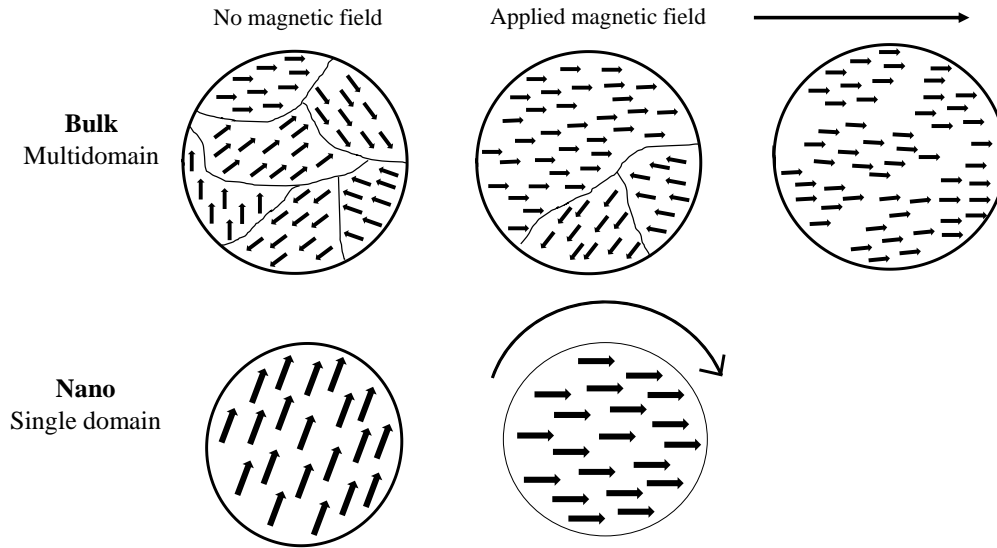
Figure 1.8 Magnetic moment alignments of bulk and nano ferromagnetic and ferrimagnetic materials
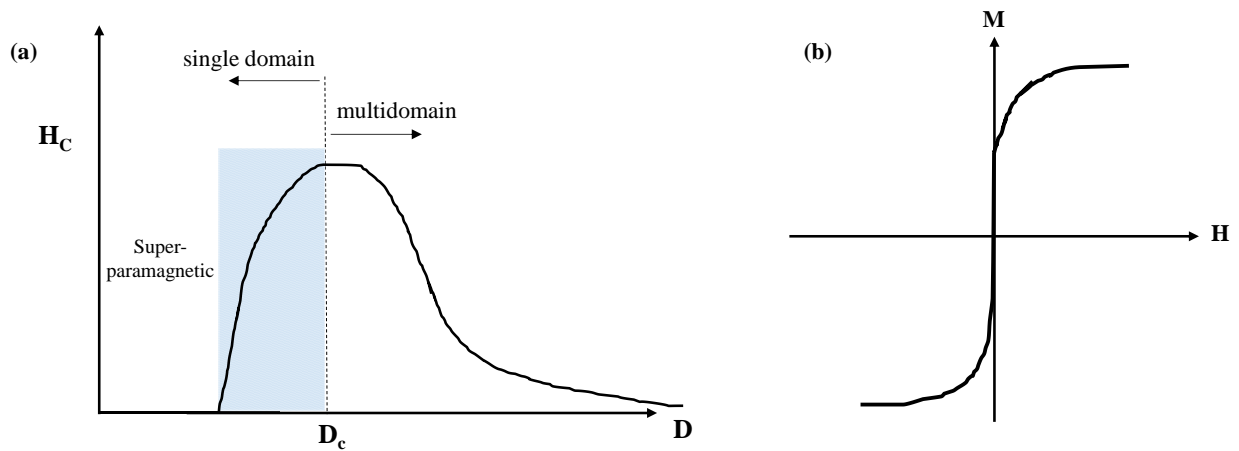
Figure 1.9 (a) Illustration of coercivity (H_C) as particle size decreases and (b) a plot of magnetization vs. applied field for super-paramagnetic materials

For experimental determination of T_B, zero-field-cooled (ZFC) and field-cooled (FC) plots are employed (Figure 1.10). To obtain ZFC plots, the magnetic particles are cooled in the absence of a magnetic field, freezing the magnetic moments in random orientations. An external

magnetic field is applied and the temperature is ramped up. Thermal motion enables alignment via coherent spin rotation. At T_B, when the thermal energy, is sufficient enough to re-orient spins randomly, the magnetization decreases. FC plots are collected by cooling the sample in an applied field and then increasing the temperature in the presence of an applied magnetic field direction. When the material is cooled in a magnetic field, the magnetic moments are frozen along the applied field. With the increase of the temperature magnetization remains constant until T_B is approached, at which point the moments randomize and a decrease in magnetization occurs. Both ZFC and FC curves show paramagnetic behavior (M α 1/T) above T_B. The derivative plots of ZFC and FC can be used to estimate T_C. For accurate determination of T_C, M vs. H curves are collected around the estimated T_C (from derivative plots of ZFC and FC) and M^2 vs. H/M plots, known as Arrott plots, are used. At T_C, a linear curve that passes through the origin is observed in M^2 vs. H/M plot.
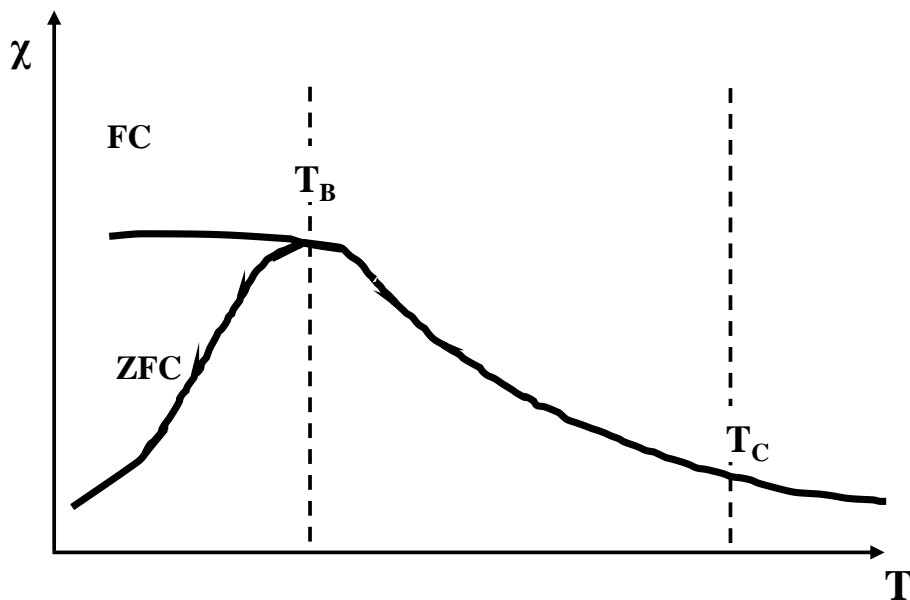
Figure 1.10 Magnetization as a function of temperature measured on zero-field-cooled (ZFC) and field-cooled (FC) samples exhibiting super-paramagnetism

1.4.6.2 Anisotropy

The behavior of magnetization in ferromagnets or ferrimagnets can be effected by one or a few anisotropic types. The common anisotropy types are: (a) crystal anisotropy, (b) shape anisotropy, (c) stress anisotropy, (d) externally induced anisotropy, and (e) exchange anisotropy. Two main types of anisotropies that can effect magnetization of nanomaterials are crystalline and shape anisotropies.[17]

Magnetocrystalline anisotropy arises when magnetic moments energetically favor aligning along a specific crystallographic direction. This is caused by spin-orbit coupling. This favorable axis is called the easy axis and is specific to a given material. The direction of the easy axis is independent of its shape and size. For example, in hcp-Co, c is the easy axis.[17] The magnetocrystalline energy is minimum along the easy axis.

Shape anisotropy appears due to the deviation of the shape from a sphere. As an example, magnetized needle-shaped particles produces magnetic charges or poles at the surface as shown in Figure 1.11. These poles can produce a magnetic field called a demagnetizing field and its direction is opposite to the direction of the applied field and in a results decrease in the total magnetization of the material. Shape anisotropy effects coercivity significantly.[61] The magnitude of the demagnetizing field will be determined by the saturation magnetization of the material.[17]
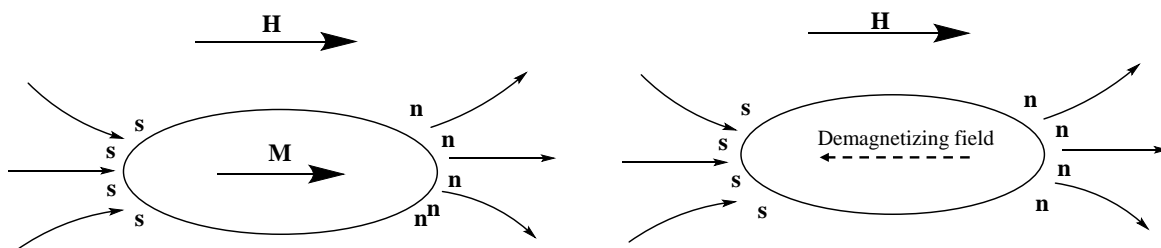
Figure 1.11 Illustration of occurrence of demagnetizatizing field due to the shape anisotropy

1.4.7 Magnetic Refrigeration (MR)

Magnetic refrigeration (MR) is based on the magnetocaloric effect (MCE).[62] MCE measures the adiabatic temperature change of a magnetic material in a varying magnetic field. MCE is intrinsic to the material and arises from changes in magnetic entropy (ΔS_M). A large ΔS_M, no hysteresis, and a broad phase transition temperature range are ideal features of magnetic refrigerants. The rare-earth metal gadolinium and gadolinium-based salts (e.g. Gd_5Si_2Ge) are the most actively studied magnetic refrigerants. However, the commercial use of gadolinium-based MR is limited due to the high cost.[62]

1.4.8 Magnetic properties of Fe_2P

Like many other transition metal phosphides iron phosphides exist in a wide range of stoichiometries including Fe_3P, Fe_2P, FeP, FeP_2, and FeP_4.[20] Iron-rich phosphide phases exhibit magnetic properties whereas phosphorous rich phases show semiconductivity.[63-66] Both Fe_3P and Fe_2P are ferromagnetic, FeP shows metamagnetic character, and FeP_2 and FeP_4 are semiconductors. Among iron phosphide phases Fe_2P has received much attention after several research reports on enhanced MCE in related quaternary MnFe(PAs)-based phases.[51-54, 67]

Fe_2P crystallizes in the hexagonal space group P62m. There are two different metal sites in the hexagonal crystal structure: (a) the M(1) site, surrounded by four phosphorous atoms in a tetrahedral geometry and (b) the M(2) site, surrounded by five phosphorous atoms and has a square pyramidal geometry (Figure 1.12). The Curie temperature (T_C) is 217 K and the magnetic transition from ferromagnetic to paramagnetic is first order (i.e. abrupt).[68] Fe_2P has a large magnetocrystalline anisotropy (2.32×10^7 erg cm^{-3}) and the magnetic easy axis is along c.[58, 69] Fe_2P has a MCE of 2.54 J/kg K at 1T. Polarized neutron diffraction studies have revealed that the two metal sites in the crystal structure, Fe(I) and Fe(II), show 0.92 μ_B and 1.70 μ_B magnetic

moments, respectively. The effects of incorporation of cationic and anionic dopants on magnetic properties of Fe_2P both experimentally and theoretically have been studied by several groups.[69-72] The substitution of phosphorous by Si and B drastically increased the T_C of Fe_2P. This increase in T_C is ascribed to an increase in stability of Fe(I) moment and sustains the exchange coupling between two Fe sites when doped with Si and B.[69]
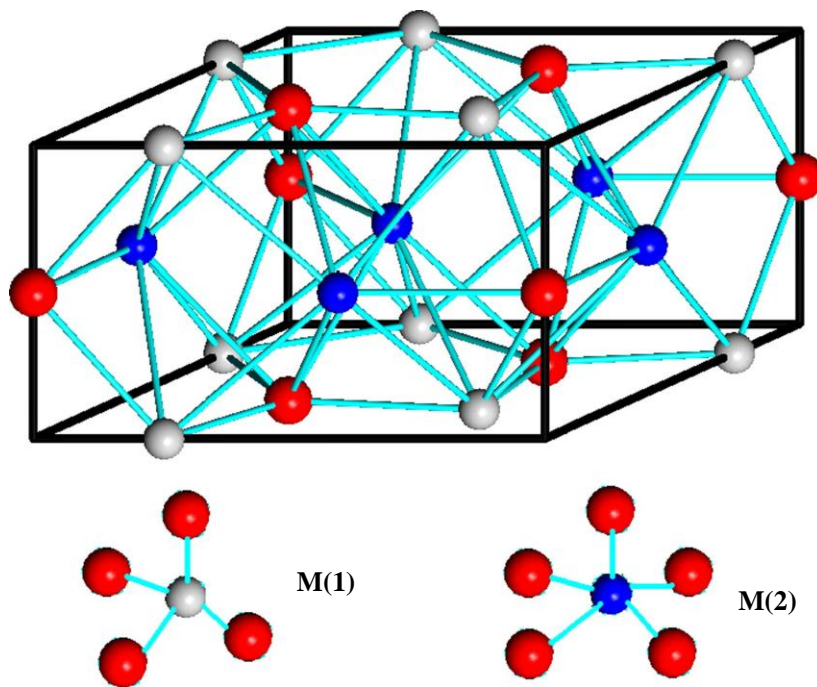
Figure 1.12 Fe_2P-typexagonal crystal structure (Copyright 2014 Elsevier B. V.)[73]

The ferromagnetism of Fe_2P is strongly affected by substitution of iron by other transition metals. Less than 2% incorporation of manganese and chromium destroys the ferromagnetic nature of Fe_2P and results in formation of anti-ferromagnetic ternary phases.[74] On the other hand, substitution of cobalt and nickel enhanced the T_C as shown in Table 1.1.[7, 24, 72] Korringa-Kohn-Rostoker method with coherent potential approximation (KKR-CPA) calculations on $Fe_{2-x}M_xP$ (M=Ni, Co) has shown that spin polarization, which measures the degree of spins aligned in a given direction, of Fe_2P increases when doped (<5 %) with Ni or Co. Therefore an increase in T_C

is observed for $Fe_{2-x}M_xP$ (M=Ni, Co). Moreover, substitution of Co and Ni does not affect the magnetic moments of the Fe(I) and Fe(II) sites or the easy axis (*c* axis). However, a decrease in magnetocrystalline anisotropy was observed when doped with Ni.[70]

Table 1.1 Composition dependent T_C for $Fe_{2-x}M_xP$ (M=Ni, Co)[7, 24, 72]

Sample composition	T_C (K)
$Fe_{1.24}Co_{0.76}P$	459
$Fe_{1.84}Ni_{0.16}P$	342
$Fe_{1.95}Ni_{0.05}P$	313
$Fe_{1.9}Ni_{0.1}P$	295
$Fe_{1.98}Ni_{0.02}P$	260

Magnetic properties of nanostructures depends on their size (D_c) and shape (anisotropy) as described in Chapter 1.4.6, and these factors can be changed to tune the magnetic properties. Therefore magnetic properties can be tuned by changing their size (D_C) and shape (anisotropy). Hyeon and co-workers reported size-dependent blocking temperatures for Fe_2P nanorods as shown in Table 1.2.[45] Kuo and co-workers also observed size dependent T_B for Fe_2P/Fe_2O_3 core/shell particles.[75]

Table 1.2 Dependence of T_B on nanorod dimensions[58]

Nanorod dimensions (nm)	Aspect ratio	T_B (K)
5 x 43	8.6	75
5 x 88	17.6	120
6 x 107	17.8	250
6 x 290	48.3	236

In 2009 Brock and co-workers reported that for phase-pure Fe_2P nanorods with ~8 x 70 nm dimensions T_C is in between 215 and 220 K (217 K for bulk) and T_B=179 K.[20] Brock and co-workers also showed Fe impurities occur easily in Fe_2P. Hyeon and co-workers observations of T_B values higher than the T_C of Fe_2P are likely due to the presence of ferromagnetic impurities such as Fe and Fe_3P since T_B cannot be higher than T_C.

As mentioned earlier, in addition to the size, doping also effects magnetic properties of Fe_2P. Hyeon and co-workers reported that $Fe_{2-x}Ni_xP$ (x= 0.2, 0.4, and 0.5) ternary nanorods with similar aspect ratios (~4.0) showed composition dependent magnetic properties.[58] As the amount of Ni increases they observed a decrease in T_B and a decrease in coercive field measured at 2 K. 20% doping has resulted in a decrease in T_B 76 K to 27 K. However, the T_C has not been reported for these nanorods.

1.5 Hydrodesulfurization Catalysis

More than 50% of global production of fossil fuels is used in transportation. The combustion of fossil fuel produces harmful gases such as NO_x (which, combined with hydrocarbons, can increase the ozone level in the troposphere), SO_x (causes acid rain and respiratory ailments), and greenhouse gases.[76] In addition, the presence of sulfur in automotive

engine exhaust can poison noble metal catalysts in catalytic converters.[76] Therefore, the removal of sulfur from petroleum feedstocks hydrodesulfurization (HDS) is an important process. The sulfur containing molecules in petroleum feedstocks can be divided into four main groups: (a) alkyl benzothiophenes (BTs), (b) dibenzothiophenes (DBTs), (c) alkyl DBTs with only one alkyl substituent at either 4- or 6- position, and (d) alkyl DBTs with two alkyl substituent at the 4- and 6- positions (Figure 1.13).[76] The substituted DBTs are known as refractory compounds and their removal is known as deep HDS. Due to steric hindrance of sulfur by alkyl groups at the 4- and/or 6- positions these compounds show relatively low reactivities to HDS.

The HDS process can occur via two different pathways as shown for DBT in Figure 1.14: (a) the hydrogenation (HYD) pathway and (b) the direct desulfurization (DDS) pathway. The first pathway, HYD, takes place in two steps. During the first step, one or both of the aromatic rings will be hydrogenated and then at the second step removal of sulfur takes place. In the second pathway, DDS, sulfur is removed directly and no hydrogenation step is involved.[76] Therefore, among the two pathways DDS is the more economical route. However, as mentioned above, the removal of sulfur from refractory compounds is difficult due to steric hindrence and HYD is the dominant pathway for successful HDS of refractory compounds.

Thiophene   **Benzothiophene**   **Dibenzothiophene**

4 or 6-methyl dibenzothiophene   **4, 6-dimethyl dibenzothiophene**
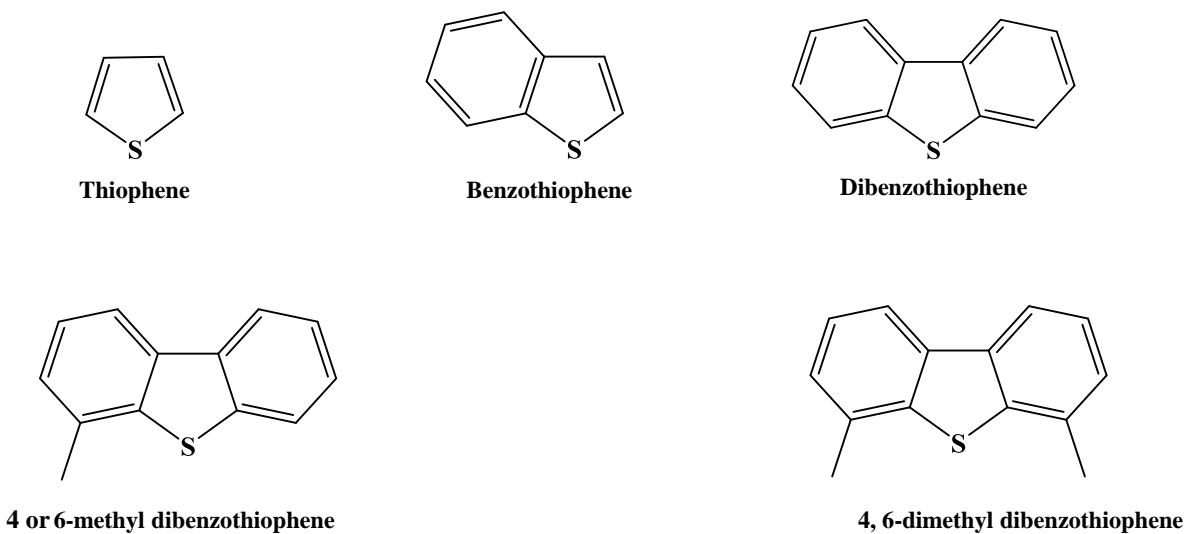
Figure 1.13 Structures of sulfur compounds in petroleum feedstocks

Hydrogenation (HYD)

Bicyclohexyl (BCH)

Cyclohexylbenzene (CHB)

dibenzothiophene (DBT)

Biphenyl (BP)

Direct Desulfurization (DDS)
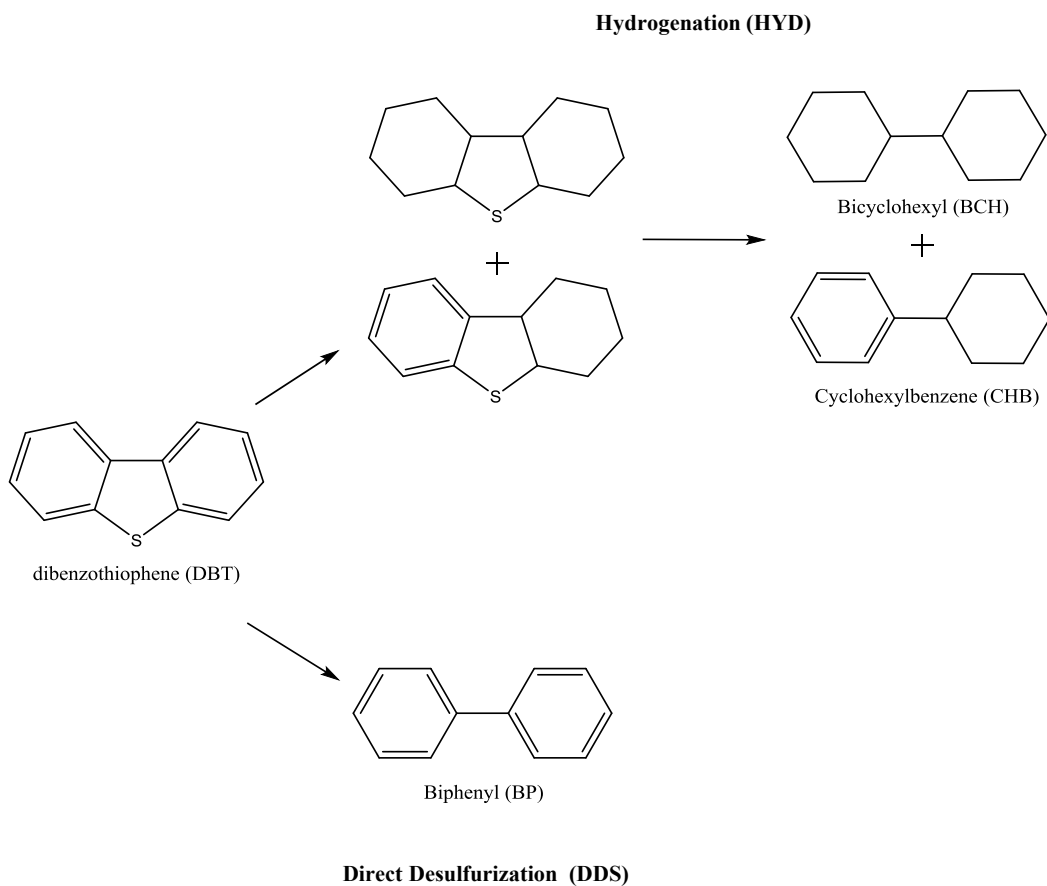
Figure 1.14   Products for DBT HDS reaction pathways

Molybdenum sulfide-based alumina-supported catalysts are used in the commercial HDS process. The structure of MoS_2 is shown in Figure 1.15.[77] Usually Co or Ni atoms are used as promoters in these catalysts. The role of the promoting atom is to weaken the Mo-S bond strength by donating electrons to Mo. The electron donation from Co or Ni brings the strength of Mo-S bonds to its optimum range for HDS catalysis.
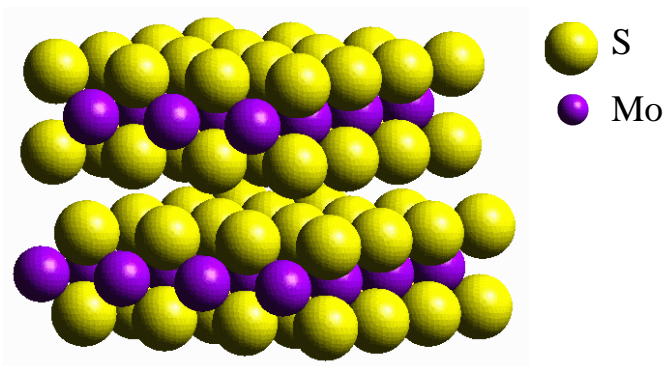
Figure 1.15 Structure of Mo_2S[77]

Due to the introduction of stringent environmental regulations and the increased use of unconventional crude oil sources with high impurity contents (especially sulfur, 5 w%) there is a strong need to improve the industrial HDS process.[77] The enhancement of the catalytic activities of existing Mo-S based catalysts has been a major focus during the last few decades wherein a two-fold increase in activity has been achieved. However, improvement of these catalysts is limited due to the inherent layered structure of MoS_2 and the fact that the active sites are located on edges.[77, 78]

1.5.1 Ni₂P as an HDS Catalyst

Metal-rich transition metal phosphides have proven to be excellent catalysts for a number of processes including hydrogenation of acetylene to ethylene by nickel and rhodium

phosphides, hydrogenation of butadiene to butane by Ni_2P, HDS and hydrodenitrogenation (HDN) by cobalt, nickel, and molybdenum phosphides.[8-12]

Among binary metal phosphides, Ni_2P is an emerging material for a range of important catalytic processes, including hydrodesulfurization (HDS), hydrodenitrogenation (HDN), hydrodeoxygenation (HDO), the water-gas-shift (WGS) reaction and the hydrogen evolution reaction (HER).[79, 80] Ni_2P is the most active, even out performing a commercial alumina-supported Ni-Mo-S catalyst when normalized to equal number of active sites.[81] Ni_2P crystallizes in the Fe_2P structure type (Chapter 1.4.8) and consists of two atomic layers along the [0001] direction.[8] The combination of these stoichiometric layers (Ni_3P and Ni_3P_2) gives Ni_2P stoichiometry. As previously described, the metal has two different coordination environments: tetrahedral (M1) and square pyramidal (M). In HDS, the Ni(1) sites are purported to facilitate the direct desulfurization (DDS) pathway in HDS and the Ni(2) sites hydrogenation (HYD) pathway.[82]

Most of the supported metal phosphide HDS catalysts are prepared using the temperature programmed reduction (TPR) method. This method involves three steps: (a) impregnation of the support with the Ni precursor ($Ni(NO_3)_2$) and phosphrous precursor (($NH_4)_2HPO_4$ or $NH_4H_2PO_4$), (b) calcination, and (c) temperature programmed reduction with H_2.[83] Even though this is a simple method to produce supported Ni_2P catalysts, there are several limitations associated with this method: (a) the average particle size of the nanoparticles depends on the incipient wetness sample loading and the surface area of the support, (b) particle size cannot be controlled precisely leading to formation of polydisperse and irregular shaped particles, and (c) the TPR method is incompatible with more active supports such as alumina due to aluminum phosphate formation. Several other approaches have been reported to prepare Ni_2P for HDS

including reduction of Ni or NiO particles with phosphines and H_2, treatment of amorphous Ni-B alloy on a silica-alumina support with a phosphine and H_2, thermal decomposition of nickel thiophosphate ($NiPS_3$), reaction of metal salts with trioctyl phosphine or triphenylphosphine, and by reacting $NiCl_2.6H_2O$ with elemental red or yellow phosphorous.[9] The recent developments in solution-phase synthesis of Ni_2P (Chapter 1.2) give the opportunity to quantitatively evaluate the effects of particle size, shape, and surface functionality on HDS catalytic activity.

The HDS catalytic activity of binary metal phosphides can be improved by the incorporation of a second metal, i.e., formation of a ternary phase. Recent investigations have shown that $Co_{0.08}Ni_{1.92}P_{2.00}$ (composition is normalized to Co+Ni=2) supported on silica prepared by TPR method has an activity for HDS of 4, 6-dimethyldibenzothiophene (4,6-DMDBT) 34% higher than that of the optimized nickel phosphide catalyst $Ni_{2.00}P_{1.60}/SiO_2$, whereas $Fe_{0.03}Ni_{1.97}P_{1.98}/SiO_2$ (excess P is from the precursor) has 40% more activity.[55, 56] Since the polydispersity of samples produced by the TPR method is high, the size dependent activity of $Fe_xNi_{2-x}P$ has not been systematically studied.

1.7 Optical Properties of NCs

Quantum size effects arise from the changes in the electronic energy levels as size decreases.[4] The density of electronic states of NPs lie between the continuous energy bands of bulk materials and the discrete energy levels of atoms and molecules. In the bulk, both metals and semiconductors have continuous energy bands due to the overlap of large numbers of atomic orbitals (Figure 1.16). For metals, the Fermi level lies the center of the bands whereas for semiconductors it lies between bands. As these energy bands develop, the center of the band develops first and edges develop last. As a result, for metals, the energy gaps between the HOMO and LUMO (valence band and conduction band) remain small at the Fermi levels even in

the nano regime. Quantum size effects are more prominent for semiconductor NPs than for metal NPs because the edges of the bands determine the optical and electrical properties and these properties strongly depend on the size. The ability to manipulate properties on the nanoscale by tuning the size opens up the possibility to develop materials with desired properties for specific applications.
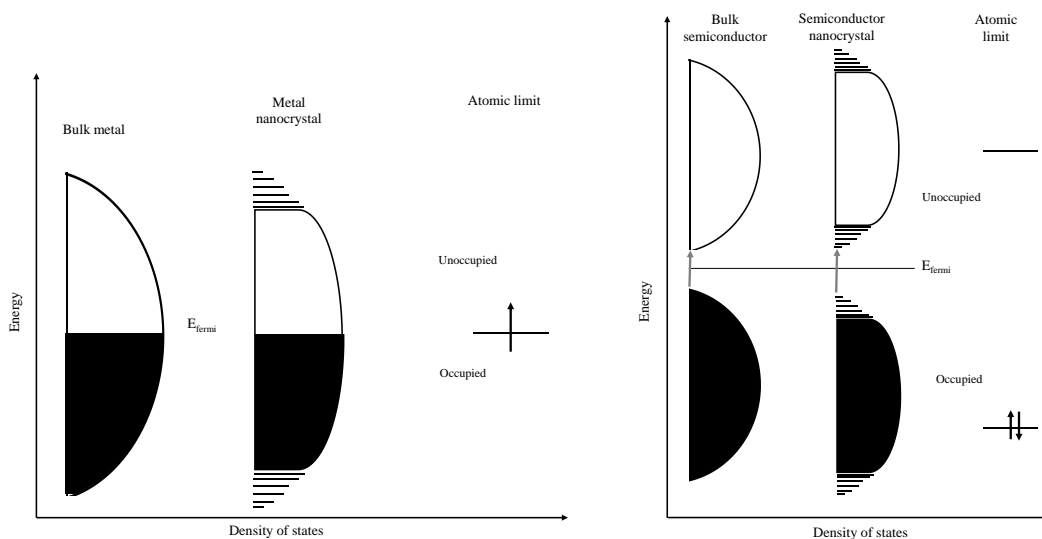
Figure 1.16 Density of states of metals and semiconductors (adapted from Alivisatos)[4]

1.8 Nanoparticle Assembly Methods

Nanomaterials are used in many different fields such as in medicine for bio imaging and in energy related applications as components of photovoltaics, light emitting diodes, catalysts, and thermoelectrics.[19] In addition to making improvements to the existing materials and developing routes to prepare new nanomaterials there is considerable interest in the development of new assembly techniques for nanotechnology. Several bottom-up nanocrystal assembly methods have been developed for constructing one-dimensional (1D), two-dimensional (2D) and three-dimensional (3D) architectures.[84-88] Common bottom-up assembly methods include; layer-

by-layer (LbL) assembly and self-organization of close-packed nanocrystals. LbL assembly is a versatile and relatively inexpensive tool. In the LBL process the substrate is alternatively exposed to negatively and positively charge polymers or particles.[88] In contrast, self-organization of close-packed NPs is achieved by the controlled removal of the solvent from the nanoparticle solution.[89] The materials formed via these methods are being evaluated in many biological and material applications. However, the dense nature of the assemblies and the poor transport properties due the presence of interfacial organic ligands limits their applicability in catalysis, gas sensing, and optoelectronic applications.

1.8.1 Sol-Gel Assembly of Gels and Aerogels

The sol-gel method can be used to prepare high surface area porous aerogel nanostructures. The first aerogel was reported by Kilster in 1931 by supercritical drying of silica 'jellies'.[90] Since this first report, the sol-gel method has been further developed to prepare many different kinds of gels and aerogels.[91-93]

The method of wet gel drying determines the porous structure of the dried gel. Drying from the wet gel solvent under ambient conditions results in formation of gels with low surface areas due to the existence of strong capillary forces (Figure 1.17).[92] The use of alkanes to dry wet gels under ambient conditions lowers the surface tension of the solvent and minimizes the pore collapse and the resultant gels are known as ambigels and have a comparable pore structure as the wet gel. This method of drying is safe and economical in production of gels on a large scale. Supercritical drying, due to the absence of liquid-vapor interfaces preserves the porous structure of the original wet gel and produces aerogels. Supercritical CO_2 can be used to dry at relatively low temperatures (30-40 °C) and pressures and is therefore a convenient supercritical drying

solvent. However, the immiscibility of liquid CO_2 with most organic solvents an extra step of solvent exchange is required.
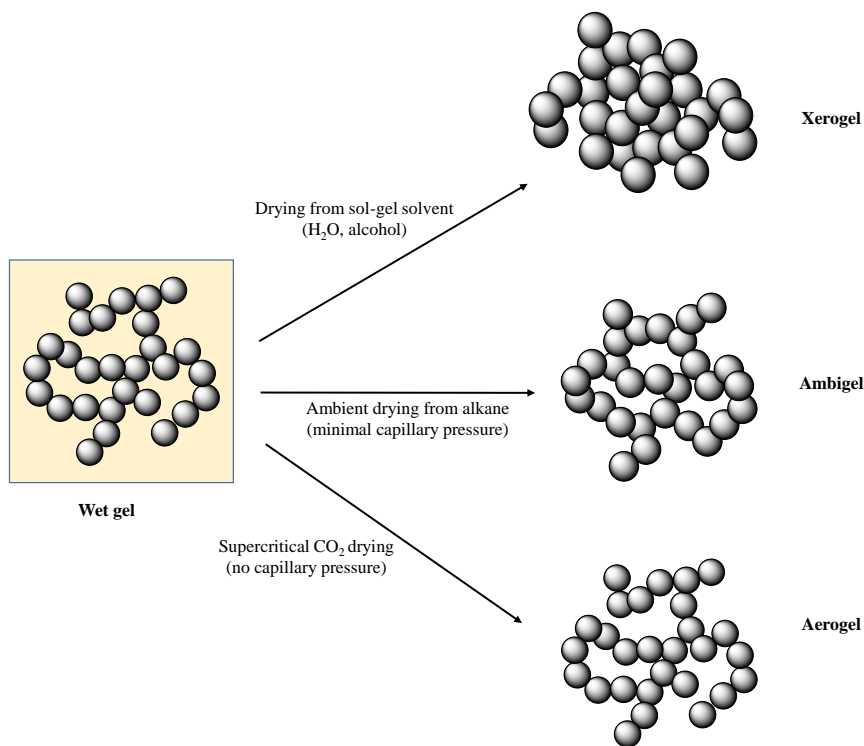
Figure 1.17 Wet gel drying methods (adapted from Rolison)[92, 94]

Gacoin reported the applicability of the sol-gel method to prepare wet gels of CdS nanoparticles.[94] In 2004 Brock and co-workers reported the formation of metal chalcogenide aerogels by controlled oxidation of thiolate capped chalcogenide nanocrystals.[95] Metal chalcogenide gelation involves, synthesis of NCs, surface ligand exchange with a thiolate, and controlled oxidation of thiolates to form the gel network. The proposed gelation mechanism for CdSe is depicted in Figure 1.18.[96] The gel network of CdSe is held together by interparticle Se-Se bonds that were formed from oxidation of surface Se^{2-} species. This process can be reversed

by using a thiolate or a mild reducing agent such as NaBH$_4$. This mechanism has been extended to other metal chalcogenides and chalcogen−chalcogen bonds are responsible for gel formation in each case. Later the applicability of this method to other chalcogenides such as CdS, CdSe, CdTe, ZnS, PbS, PbTe, and Bi$_2$Te$_3$ was demonstrated and the potential use of these materials in applications such as gas sensing, heavy water remediation, thermoelectrics, and photovoltaics has been studied.[85, 97-102]
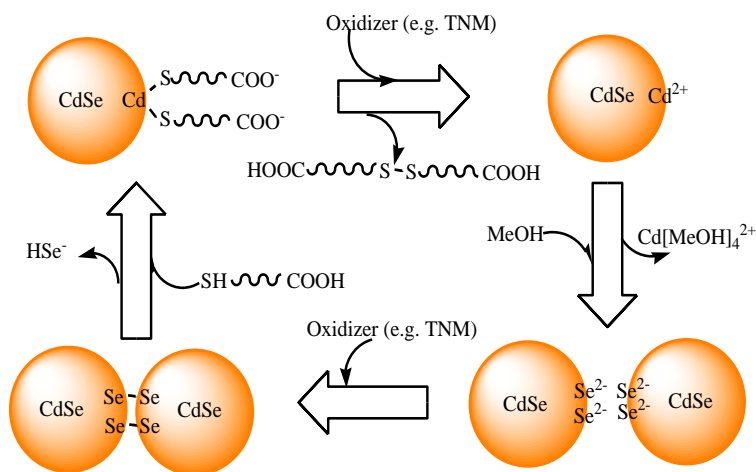
Figure 1.18 The proposed gelation mechanism for CdSe NCs (Copyright 2014 John Wiley and Sons)[96]

1.9 Thesis Statement

The development of new alternative refrigeration technologies such as thermoelectric refrigeration, thermoacoustic refrigeration, absorption/desorption refrigeration, and magnetic refrigeration are being evaluated as alternatives to conventional gas compression (CGC) because CGC has reached its limit of energy efficiency.[103] The development of magnetic refrigeration (MR) technology was started after the discovery of the magnetocaloric effect (MCE) in 1881.[104]

MR has several advantages over CGC technology. The higher cooling efficiency (30-60% of a Carnot cycle, vs. 15-10% for CGC), compact design (all solid-state) and environmental friendliness (no leaking of greenhouse gases) are a few of them.[105] The rare-earth metal gadolinium and gadolinium-based salts (e.g., $Gd_2(SO_4)_3.8H_2O$) are used in MR and are the most active magnetic refrigerants to date. However, commercial use is limited due to cost of Gd ($4000/kg).[105] Transition metal-based compounds have attracted attention after several reports of MCE in $MnFeP_{1-x}As_x$, and research is expanding to other metal pnictides (pnicogen=Group 15 elements).[106] The parent compound Fe_2P is ferromagnetic and shows considerable MCE at its Curie temperature (T_C). Moreover, Fe_2P has a similar isothermal entropy change (2.54 J/kg K) as gadolinium metal under a magnetic field change of 1 T.[57] However, the lower T_C of Fe_2P (217 K vs. 294 K for Gd), makes it inappropriate for use in room temperature MR. Incorporation of Ni into Fe_2P can enhance the T_C above room temperature. The highest T_C achieved was 342 K for $Fe_{1.84}Ni_{0.16}P$.[107] While the bulk magnetic properties of $Fe_xNi_{2-x}P$ have been studied, the magnetic properties of nanoscale materials are poorly understood, in part due to a lack of synthetic methods that enable control of size and composition. It is anticipated that due to the reduced thermal hysteresis on the nanoscale the cycling rate in MR will be improved. Also the formation of nanoparticles can moderate coercivity and lead to super-paramagnetism, enabling property tuning beyond that achievable by composition modulation. The aim of this part of dissertation research is to examine the influence of Ni on the magnetic properties of nanoscale Fe_2P. In order to do that, a synthetic protocol to prepare monodisperse $Fe_xNi_{2-x}P$ nanocrystals with various compositions across all x is established. Magnetization (*M*) data as a function of temperature (*T*) and field (*H*) are acquired and the Curie temperature (T_C) and Blocking temperature (T_B) will be compared to bulk $Fe_xNi_{2-x}P$.

Due to the depletion of Saudi Arabian crude oil and consequent increase in oil prices, countries around the world have turned their attention to non-conventional fuel sources. Canadian crude oil, derived from oil sands, has received attention because of its abundance and low cost. For example, in April 2014 the USA has utilized nearly twice as much Canadian crude oil (83,083 thousand barrels) than Saudi Arabian crude oil (47,364 thousand barrels).[108] The higher impurity levels (especially sulfur) compared to Saudi Arabian crude oil limits wide use of Canadian crude oil around the world. Meanwhile, environmental regulations in many countries, including the US, are requiring reduced amounts of sulfur in fuel oil. The commercially used molybdenum sulfide-based hydrodesulfurization (HDS) catalysts with Ni or Co promoters have been studied intensively to improve the activities and achieve the lower levels of sulfur as required by stringent environmental regulations. However, while a two-fold increase in activity has been achieved over the last three decades; further enhancement is limited, in part due to the layered crystal structure of MoS_2.[77] Therefore, new efficient catalysts capable of removing the most refractory thiophenes need to be explored. Isotropic structures, metallic nature, and higher sulfur resistance make metal phosphides very promising hydrotreating catalysts. Among binary phases studied (Co_2P, MoP, WP, Fe_2P), Ni_2P has shown the highest catalytic activity.[81] However, several recent studies have shown that the hydrotreating properties of monometallic phosphides can be improved by incorporating a second metal, attributed to synergetic effects. A catalyst having a composition of $Fe_{0.03}Ni_{1.97}P_{1.98}/SiO_2$ has shown a 40% increase in hydrodesulfurization (HDS) catalytic activity relative to the optimized nickel phosphide catalyst.[6] However, no systematic study has been done on particle size effects on HDS activity of $Fe_xNi_{2-x}P$, because the traditional temperature programmed reduction (TPR) method does not enable sufficient particle size control. The aim of this part of my dissertation research is to

establish the effect of composition of $Fe_xNi_{2-x}P$ monodisperse nanoparticles on HDS activity. Mesoporous silica-encapsulated $Fe_xNi_{2-x}P$ nanoparticles will be synthesized and HDS activities will be tested for relevant Ni-rich compositions and compared to TPR-prepared materials.

The aim of this part of the dissertation research is to establish techniques to integrate nano materials into solid state functional devices while maintaining their nanoscale characteristic properties, using aerogels as a model architecture. Aerogels have interconnected 3-dimensional networks of pores and nanoscale building blocks enabling individual particles to be accessed within the 3-D structure. Interconnected 3-D porous assemblies of nanocrystals are important in applications where connectivity, large accessible surface areas, and interfacial interactions with complimentary components are desired (e. g. hybrid photovoltaics, catalysis, sensing). The synthesis and properties of metal oxide, carbon and metal chalcogenide gels and aerogels have been reported in the literature; however, there are no reports on the synthesis of metal phosphides gels and aerogels. The aim of the last part of my dissertation research is to establish a sol-gel method for assembly of NCs of InP (semiconductor) and Ni_2P (catalyst) into 3-D structures and evaluate the mechanism of formation and consequences for the physico-chemical properties of the gels.

The dissertation is laid out as follows: Chapter 2 presents a detailed description of experimental and characterization techniques that were employed in this research work. Chapter 3 discusses the synthesis and characterization of discrete $Fe_xNi_{2-x}P$ ternary NPs and magnetic properties of Fe-rich phases. Chapter 4 describes mesoporous silica encapsulation of Ni-rich $Fe_xNi_{2-x}P$ NPs and their hydrodesulfurization activities. Chapter 5 describes the formation of gels and aerogels based on InP and Ni_2P NP assembly. Finally, Chapter 6 presents the main conclusions of this dissertation and a prospectus for the future.

CHAPTER 2

EXPERIMENTAL AND MATERIAL CHARACTERIZATION TECHNIQUES[2]

Metal phosphide nanocrystals ($Fe_xNi_{2-x}P$, Ni_2P, and InP) were synthesized using solution-phase arrested-precipitation techniques under argon atmosphere. The materials were characterized using Powder X-Ray Diffraction (PXRD), Transmission Electron Microscopy (TEM), Energy Dispersive Spectroscopy (EDS), Surface Area and Porosimetry, Thermogravimetric Analysis (TGA), X-Ray Photoelectron Spectroscopy (XPS), Inductively Coupled Plasma-Mass Spectrometry (ICP-MS), and Magnetic Susceptibility. This chapter includes a detailed description of the synthetic and characterization techniques used in this dissertation research.

2.1 Reagents

Nickel(II) acetylacetonate ($Ni(acac)_2$, 95%, Alfa Aesar), iron(0) pentacarbonyl ($Fe(CO)_5$, 99.99%, Sigma Aldrich), trioctylphosphine (TOP, 97%, Strem), oleylamine (C18 content 80-90%, Acros America), octylether (90%, TCI America), chloroform (99.9%, Fisher), absolute ethanol (AAPER Alcohols and Chemicals), indium(III) chloride ($InCl_3$, 99%, Alfa-Aesar), tris(trimethylsilyl)phosphine ($P[Si(CH_3)_3]_3$, 98%, Strem), 11-mercaptoundecanoic acid (MUA, Aldrich 95%), tetramethylammoniumhydroxide pentahydrate (TMAH, Acros, 99%), hydrogen peroxide (H_2O_2, 3%), ethyl acetate (Fisher, 99.9%), 1-dodecanethiol (≥98%, Aldrich), 4-fluorothiophenol (98%, Aldrich), tetranitromethane (TNM, Sigma Aldrich), triethylamine (technical grade, Strem), hexanes (technical grade, Fisher), tetraethyl orthosilicate (TEOS,

---

Aldrich), sodium hydroxide (≥98%, Aldrich), and methanol were used as received. Trioctylphosphine oxide (TOPO, 90%, Aldrich) was purified through vacuum distillation.

2.2 Synthetic Methods

2.2.1 Synthesis of Metal Phosphide Nanoparticles, Ligand Exchange, and Assembly of Gels and Aerogels

A detailed description of the synthesis of specific metal phosphide nanoparticles is given in Chapters 3-5. Nanoparticles were synthesized using solution-phase arrested-precipitation methods under inert atmosphere using Schlenk line techniques. Nanoparticle isolation and ligand exchange were carried out in the lab ambient. Gels were synthesized using the sol-gel method and the metal-assisted gelation method as described in Chapter 5. The wet gels were supercritically dried to form aerogels.

2.2.2 Supercritical Drying of Gels

When wet gels dry under ambient conditions, the forces acting on the liquid/gas interfaces during liquid evaporation from the pore walls causes the pores to shrink and ultimately collapse, resulting in the loss of more than 90% of the gel volume. Liquid evaporation from the wet gel takes place in several steps. First, the pores shrink by an equal volume to that occupied by the solvent, then solvent flows from the gel body onto the surface. As the drying proceeds, the pore volume gets smaller and the gel becomes stiff, which will eventually increase the surface tension leading to cracking in the gel structure. Further drying leads to collapse of the pore network. However, when a solvent is in its supercritical state, liquid/gas interfaces do not exist. Therefore the removal of the solvent at its supercritical state prevents the pore collapse and leads to maintenance of the gel pore structure.[91]

For the supercritical drying process, the wet gel is placed in an autoclave filled with the drying solvent. Then the temperature is slowly raised to exceed the supercritical state (T_c, P_c, and V_c) of the corresponding solvent. Finally, the pressure is released slowly at a constant temperature above T_c.

In this dissertation research, a SPI-DRY model CO_2 critical point dryer with a Fisher Scientific ISOTEMP 10065 recirculating temperature bath was used for aerogel formation. CO_2 is a more suitable solvent than alcohols to use in critical point drying due to its lower T_c (31.1 °C) as shown by the phase diagram of CO_2 in Figure 2.1.[93] Due to the immiscibility of CO_2 with the solvents used in gel formation (ethanol and methanol) an additional solvent exchange step was carried out prior to the drying. The wet gel solvent was thoroughly exchanged three times with 3-5 mL aliquots of fresh acetone without disturbing the gel network, then the sample vials were placed in the chamber maintained at 19 °C. The solvent exchange of acetone for CO_2 was carried out over a 4 h period by filling the chamber with liquid CO_2 and subsequently draining the solvent for a total of four times. For the supercritical drying step, two-thirds of the chamber was filled with liquid CO_2 and the temperature was raised to 39 °C. With the increase of the temperature, the pressure inside the chamber increased (89−103 atm) enabling the supercritical state to be achieved. The gel was kept at that temperature and pressure for 1 h and then the pressure was released to dry the gel over 30-40 min.
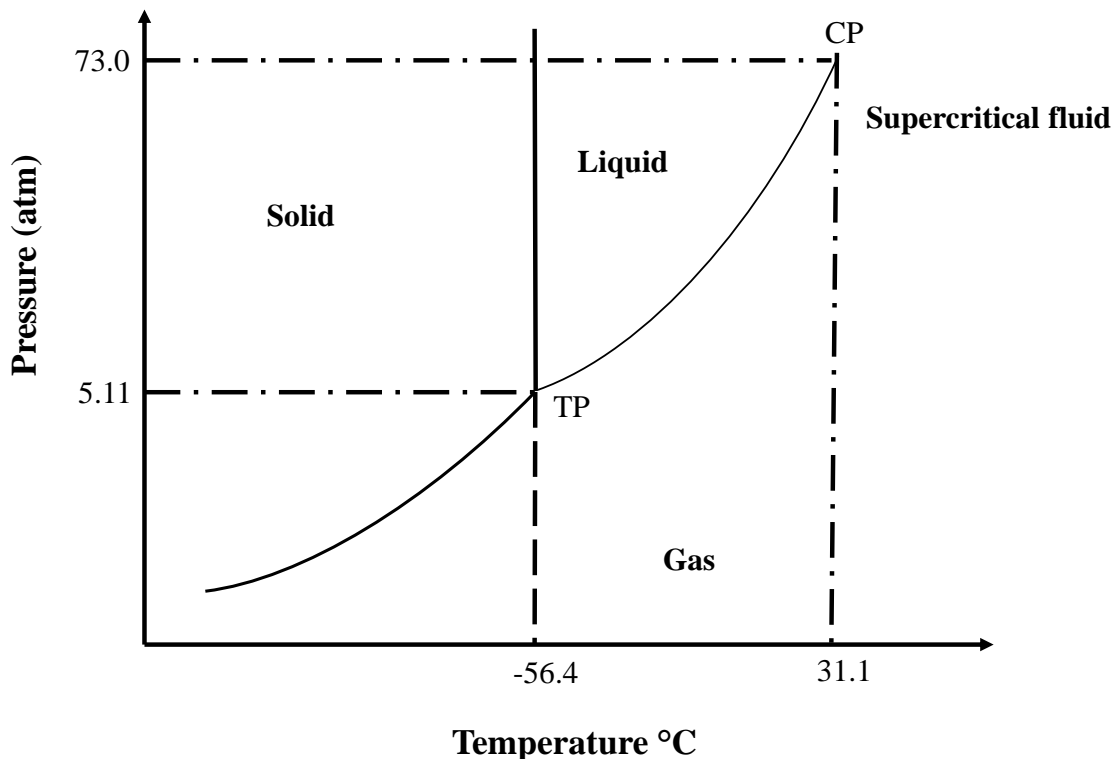
Figure 2.1 The phase diagram of CO_2 (adapted from Pajonk)[93]

2.3 Characterization Techniques

2.3.1 Powder X-Ray Diffraction (PXRD)

Powder X-ray diffraction is useful in determining the crystal structure of materials. The Powder X-ray diffraction pattern of a material is determined by two factors: (a) the size and the shape of the unit cell and (b) the atomic numbers and positions of the atoms in the unit cell. Therefore the powder diffraction patterns serve as "finger prints" for specific phases and can be used to identify materials.[60]

X-rays are electromagnetic radiation with a wavelength of 1 Å (10^{-10} m). X-rays are generated when high energy electrons collide with a metal target. A Schematic design of a filament X-ray tube is shown in Figure 2.2.[60] There are three main components of an X-ray tube:

(a) an electron generating source (cathode), (b) a metal target (anode), and (c) an evacuated chamber with windows for the X-rays. Tungsten is the most common cathodic filament found in X-ray tubes. In a vacuum, when the filament is heated by an application of a filament current, electrons are generated. The generated electrons are accelerated towards the anode (copper is the most common metal target) by applying a high voltage. When high energy electrons collide with the metal target, X-rays are generated. The produced X-rays then pass through X-ray transparent windows. The X-ray absorption characteristics of a material depend on its atomic weight, and beryllium is used in X-ray transparent window materials because of its smaller (4) atomic number. The fraction of the incident electron beam that is converted into X-rays is small, and the rest of the energy is converted into heat. Therefore the cathode needs to be continuously cooled to prevent melting of the target. The X-rays resulting from an X-ray tube have two constituents: (a) white radiation and (b) monochromatic X-ray radiation. White radiation is generated when accelerating electrons lose energy due to collisions, which is then converted into broad spectrum electromagnetic radiation. For X-ray powder diffraction experiments monochromatic X-rays are used.[60]
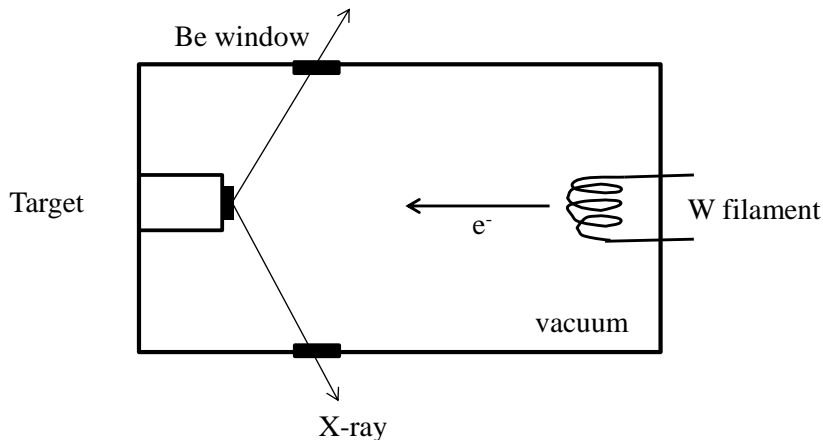
Figure 2.2 Schematic representation of an X-ray tube (adapted from West)[60]

When high energy electrons strike a Cu metal target with sufficient energy to ionize a Cu 1s (K shell) electron, an outer shell (2p or 3p) electron will drop down to occupy the vacancy in the 1s shell and the energy difference between the two shells will be released as X-rays (Figure 2.3). These energy levels are quantized. Thus, the transitions have fixed energies and the generated monochromatic X-rays will be characteristic for the material. For Cu, the most intense transition is 2p → 1s, which is called Kα and has a wavelength of 1.5418 Å. There are two possible spin states for 2p ($p_{1/2}$ and $p_{3/2}$) with slightly different energies. Therefore the Kα transition (2p → 1s) is a doublet, $K\alpha_1$=1.54051 Å and $K\alpha_2$=1.54433 Å. The Kβ arises from 3p → 1s transition (1.3922 Å). Due to the higher intensity, the Kα line is used in diffraction experiments. To eliminate the interference from Kβ and white radiation, a filter is used. Usually an element that has an atomic number one or two lower than the target material is used. Nickel is capable of absorbing Cu Kβ and most of the white radiation. Therefore, for Cu containing diffractometers nickel is a suitable filter.[60]
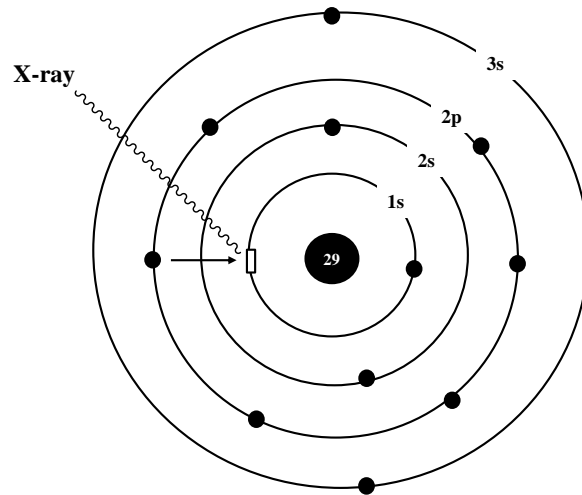
Figure 2.3 Generation of Kα X-rays (adapted from West)[60]

Since X-rays have compatible wavelengths (ca. 1 Å) to interatomic separations (2-3 Å), crystals with ordered repeating units should be capable of diffracting X-rays similar to the diffraction of light by an optical grating. The atoms or the ions in the crystals act as secondary point sources and scatter the X-rays.

Bragg's Law can be used to treat X-ray diffraction by crystals. Consider two parallel X-rays, 1 and 2, incident on crystal points on two parallel planes that are separated by a distance d (Figure 2.4).[60] If the angle of the incident beam is θ and the beam is diffracted by a similar θ angle, the additional distance travelled by the second wave (2Δ) is given by Equation 2.1.

$$2\Delta = 2d \sin \theta \qquad (2.1)$$

Constructive interference of two waves occurs when the two diffracted waves are in phase. That is, when the path-length difference is an integral wavelength (Equation 2.2).

$$2\Delta = n\lambda \ \ (n=1, 2, 3, \ldots) \qquad (2.2)$$

By combining Equation 2.1 and 2.2 Bragg's Law can be derived and θ is referred to as Bragg's angle (Equation 2.3).[60] Because the d-spacing reflects interatomic distances in the crystal, the Bragg angle can be used to determine the unit cell size and shape.

$$n\lambda = 2d \sin \theta \qquad (2.3)$$
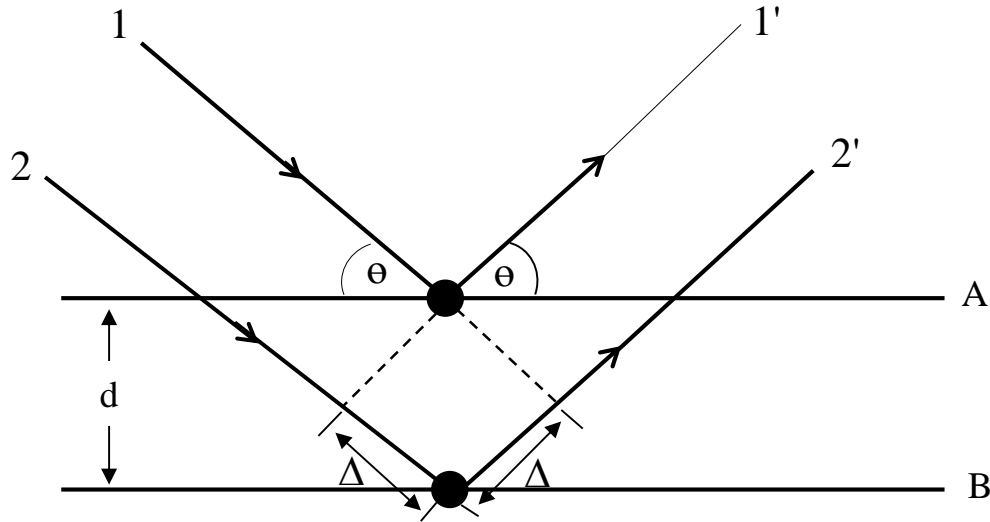
Figure 2.4 Illustration of x-ray diffraction by two atoms in two parallel crystal planes (adapted from West)[60]

The X-rays scattered by an atom are a result of individual wave scattering by each electron present in the atom. The intensity of the scattered beam depends on the scattering factor or form factor (*f*) of atoms (or ions) present in the crystal. The scattering factor is determined by the atomic number; the higher the atomic number the higher the scattering factor, and hence, the intensity.[60]

The basic principle of the powder X-ray diffraction experiment is shown in Figure 2.5.[60] The crystals in a powdered sample are oriented in every possible direction. Thus, for each set of planes at least one or a few crystals must be oriented at the Bragg angle relative to the incident beam. When the monochromatic X-rays hit the sample, the diffraction occurs and the diffracted beam is detected by the detector.
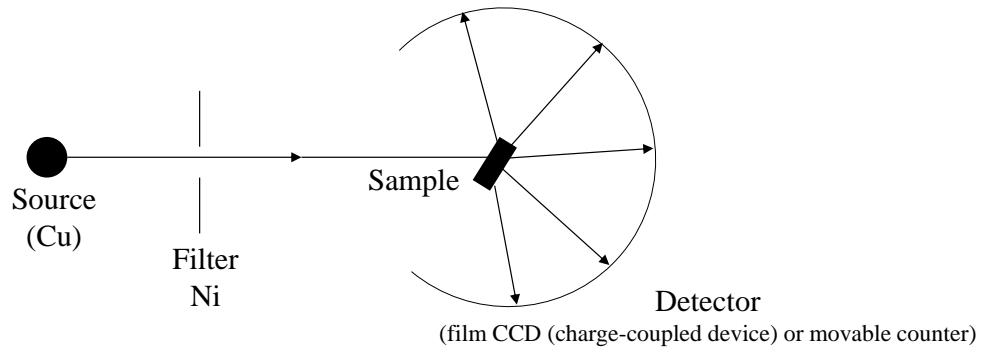
Figure 2.5 Schematic of a powder X-ray diffraction experiment (adapted from West)[60]

The PXRD pattern of a nanoparticle sample is shown in Figure 2.6. The peak positions and relative intensities are unique for the phase, whereas the breath of these reflections is inversely proportional to the crystallite size of the material. The Scherrer formula (Equation 2.4) can be used to calculate the average crystallite size where, t is the average crystallite size, λ is the X-ray wavelength, B is the full width at half maximum, θ is the Bragg angle, and K is shape factor.[60] Typically for spherical particles, K is 0.9. The peak broadening arises because there is insufficient number of lattice planes in nanomaterials insure complete destructive interference near the Bragg angle.

$$t = \frac{K\lambda}{B\cos\theta} \tag{2.4}$$
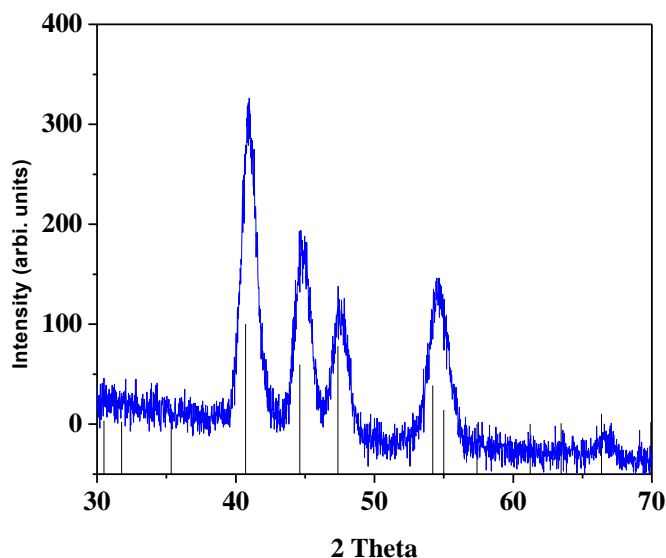
Figure 2.6 Representative PXRD pattern for Ni$_2$P nanoparticles. The ICDD-PDF overlay of Ni$_2$P (PDF# 74-1385) is shown as vertical lines

In this dissertation study a Rigaku RU 200B rotating anode X-ray diffractometer with a Cu Kα (1.5418 A°) rotating anode source was employed to study the phase and crystallite size of the nanoparticles and aerogels. The X-rays are generated at 40 kV and 150 mA and the diffracted beam is detected with a scintillation counter detector. The samples were deposited on a low background quartz (0001) holder coated with a thin layer of grease. X-ray diffraction patterns were identified by comparison to phases in the International Centre for Diffraction Data (ICDD) powder diffraction file (PDF) database (release 2000). A representative pattern for Ni$_2$P is shown in Figure 2.6.

2.2 Transmission Electron Microscopy (TEM)

Transmission electron microscopy is an efficient and versatile materials characterization technique for providing information about nanomaterial shape, size, and structure. The basic operational principle of a TEM is similar to that of an optical microscope, but electrons and

magnetic lenses are used instead of photons and glass lenses. There are several advantages of electron microscopy over optical microscopy, the main one being its high resolution. The distance between two resolvable points (δ) (smaller δ results higher resolution) is proportional to the wavelength (λ) of electromagnetic radiation used as shown in Equation 2.5, where μ is the refractive index of the viewing medium and β is the semi-angle of collection of the magnifying lens.[109] For example, the wavelength of the green region in the visible spectrum is 550 nm, hence δ is ~300 nm. This distance corresponds to several hundreds of atom diameters. On the other hand the wavelength of the electrons in the electron microscope depends on the accelerating voltage (V) and can be manipulated easily by changing the applied voltage, as shown in Equation 2.6, where h is Planck's constant, m_0 is the mass of the electron, and eV is the kinetic energy.[109] For 100 eV applied voltage δ is ~ 4 pm, which is smaller than the distance between atoms of elements. Moreover, since electrons are charged particles they can be directed easily and the strong interactions with both the nucleus and the electrons of the elements of the specimen enable high sensitivity.

$$\delta = \frac{0.61\lambda}{\mu \sin \beta} \tag{2.5}$$

$$\lambda = \frac{h}{(2m_0 eV)^{1/2}} \tag{2.6}$$

The basic components of a typical TEM are shown in Figure 2.7.[110] The electron source (gun) can be either a thermoionic source (tungsten filament or lanthanum hexaboride (LaB_6)) or a field emitter (fine tungsten needle). The electrons emitted are accelerated through a high voltage (100-400 kV) in an vacuum to prevent electron scattering. The electron beam is directed by three sets of electromagnetic lenses: (a) condenser lenses (to control the size and angular spread of the incident electron beam), (b) objective lenses (to focus the electron beam passing

through the specimen itself), and (c) intermediate and projector lenses (to expand the beam onto the viewing screen).
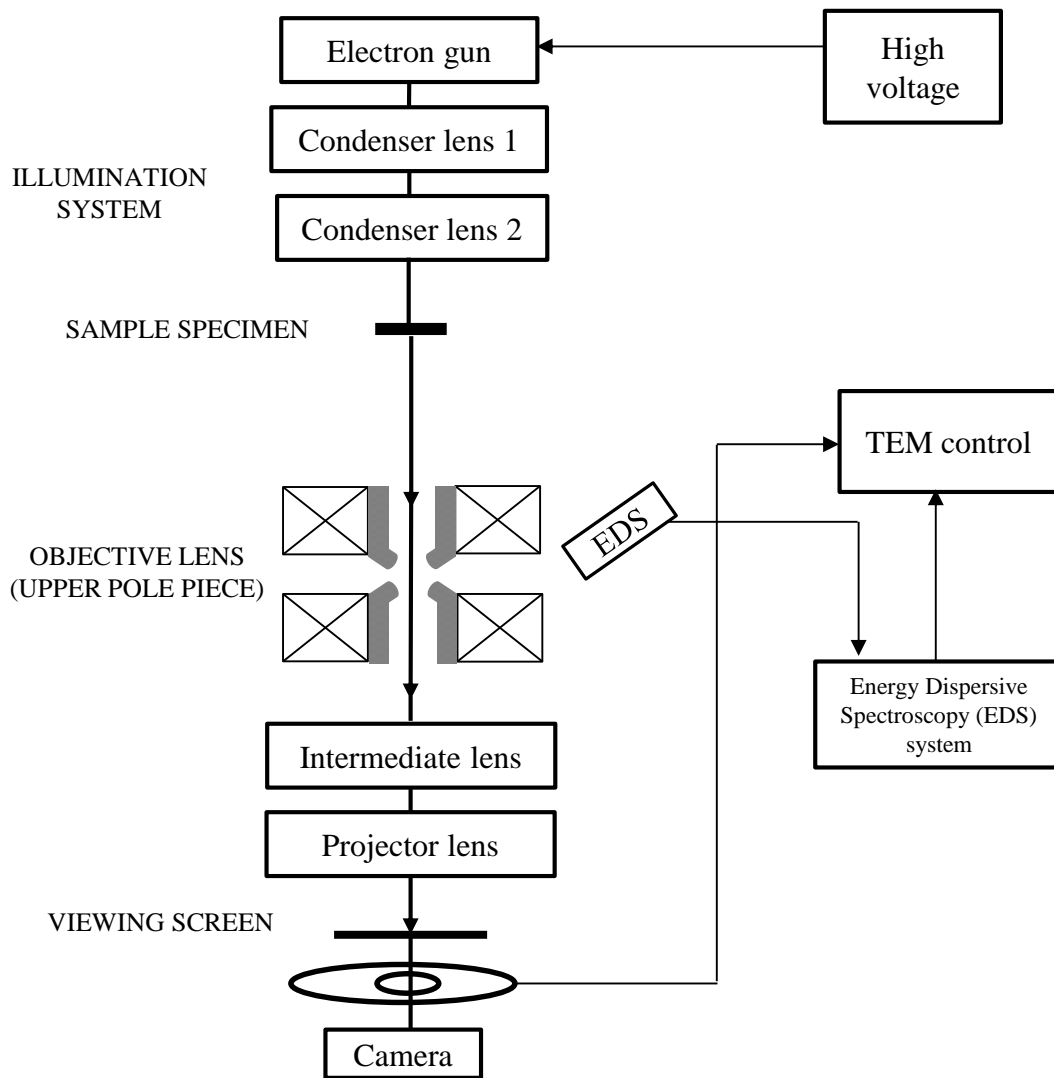
Figure 2.7 Illustration of a typical TEM (adapted from Fultz)[110]

There are two different basic modes of imaging in TEM: (a) dark field and (b) bright field. In bright field imaging mode, the diffracted beam is blocked by the objective aperture and only the undiffracted (direct) beam passes through (Figure 2.8a).[109] The sample appears dark and the background appears bright in this mode of imaging. The contrast of the image depends on the

electron density of the elements that make up the sample and the thickness of the sample specimen. In dark field imaging mode, the diffracted beam is selected (Figure 2.8b).[109] In this mode, the diffracting area appears brighter and background appears darker and we only see contrast due to crystalline features.
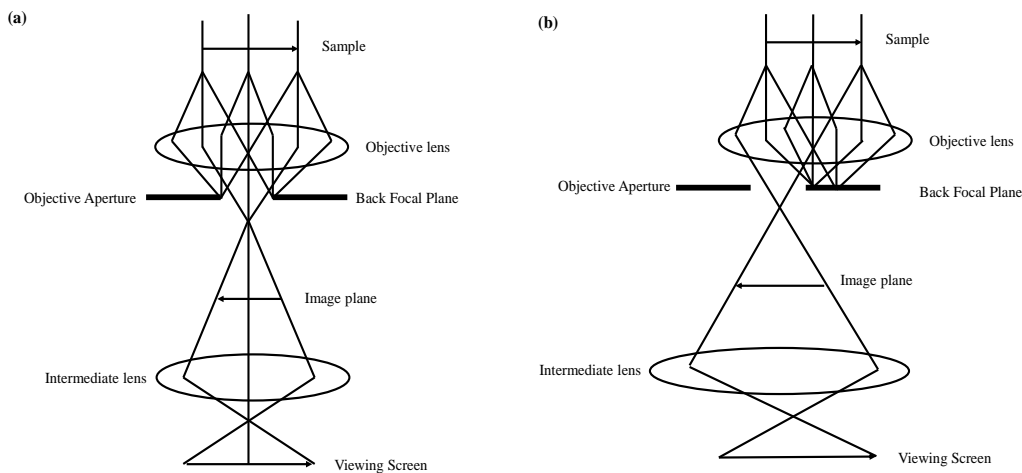
Figure 2.8 Ray diagrams showing (a) bright field and (b) dark field imaging modes (adapted from Williams)[109]

In addition to imaging, TEM also operates as a diffractometer to create diffraction patterns by electron diffraction. For Selected Area Electron Diffraction (SAED) in order to project the diffraction pattern onto the viewing screen an additional aperture (intermediate aperture) is placed in the image plane and only the diffracted beam of the selected area is allowed to pass through. The SAED pattern can be seen on the viewing screen as a ring pattern or as a set of spots. The rings are observed for polycrystalline samples and the spots are for single crystal samples. The diameter of the rings or the distance between two opposite spots can be used to calculate d-spacing of the crystal lattice.

In this dissertation research, a JEOL 2010 HR TEM electron microscope operating at an accelerating voltage of 200 kV and a current of 106-108 μA with a LaB_6 thermoionic source in bright field mode was employed to study the morphology of nanoparticles and aerogels. Nanoparticle and aerogel specimens were prepared by placing a drop of a dilute chloroform or acetone dispersion of nanoparticles on a carbon-coated copper grid and evaporating the solvent.

2.3.3 Energy Dispersive Spectroscopy (EDS)

When a sample is bombard with high energy electrons, several processes can take place including X-ray generation (Figure 2.9).[109] The energy of the generated X-rays are characteristic of the bombarded elements as discussed in Chapter 2.3.1 and can be therefore used to identify elements. This is the basic principle behind EDS. Frequently an EDS unit is coupled with either a TEM or a SEM. A schematic representation of the EDS system is shown in Figure 2.10.[109]
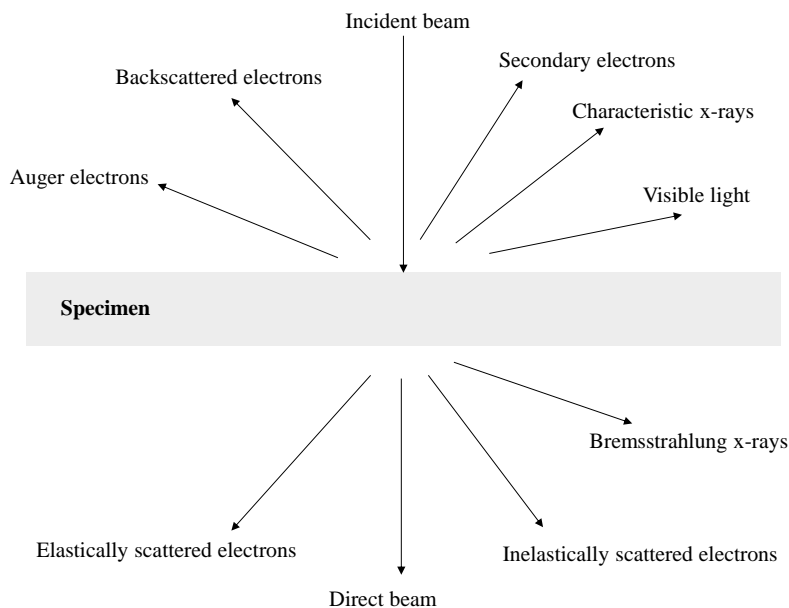
Figure 2.9 Signals generated when a sample is bombarded with a high energy electron beam (adapted from Williams)[109]
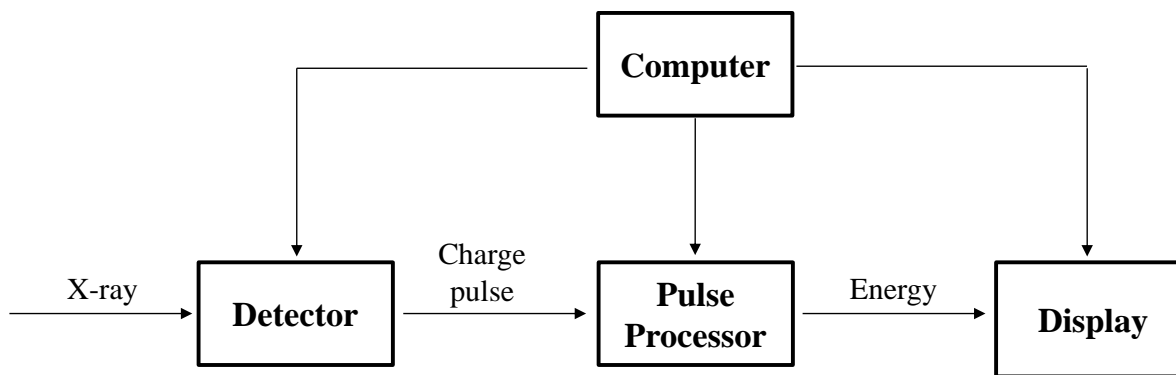
Figure 2.10 Schematic representation of the EDS system (adapted from Williams)[109]

The detector in the EDS generates a charge pulse that is proportional to the X-ray energy. This pulse is subsequently converted to a voltage by the pulse processor. The resulting spectrum is a plot of X-ray counts (intensity) vs. energy as shown by the representative plot of $Fe_xNi_{2-x}P$ nanoparticles in Figure 2.11. EDS is a semi-quantitative method and in this dissertation work EDS was used to determine the approximate compositions of nanoparticles.
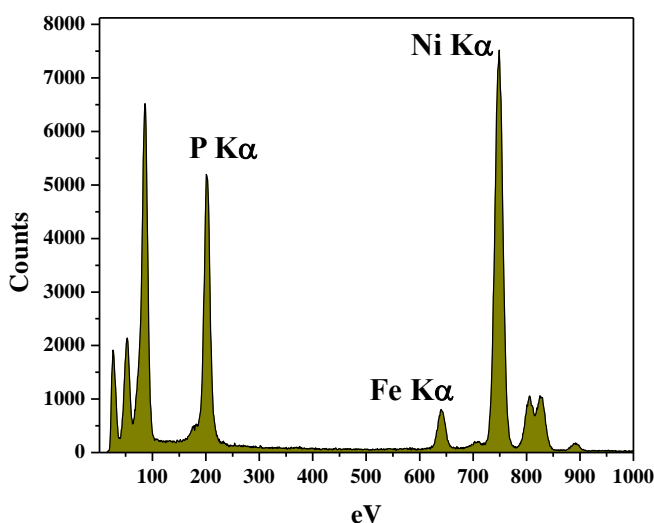
Figure 2.11 EDS spectrum of a $Fe_xNi_{2-x}P$ nanoparticle sample. The characteristic Kα lines of P, Fe, and Ni are indicated

In this dissertation research an EDAX, Inc., detection unit attached to the JEOL 2010 TEM was employed to determine approximate compositions of nanoparticles. The percentage atomic weights of the probed elements of the samples were determined using EDAX Genesis software version 1.0.

2.3.2 Surface Area and Porosimetry

Surface area and porosimetry are two important physical properties that can influence performance for a broad range of applications. Surface area and porosimetry can be determined based on the adsorption/desorption of gases onto solids. Depending on the forces acting between the gas molecules and the solid atoms or ions, either physisorption (van der Waal forces) or chemisorption (chemical bond formation) can take place. The quantity of gas adsorbed by a solid is a function of the sample mass, temperature, and the nature of the gas and the solid. The adsorption/desorption of a gas by a solid can be treated using several approaches. The Langmuir theory is commonly used for chemisorption and BET theory is used for physisorption.

In 1916 Irving Langmuir developed a theory to evaluate the surface area of materials.[111] Langmuir theory assumes monolayer adsorption of gas molecules onto solids and that collisions between gas molecules and the solid are inelastic. The quantity of gas adsorbed, V_a at pressure, P is given by Equation 2.7 and V_m is the quantity of gas adsorbed to form a monolayer and b is an empirical constant.[112]

$$V_a = \frac{V_m bP}{1+bP} \tag{2.7}$$

Equation 2.7 can be re-arranged as shown in Equation 2.8. The intercept and slope of a plot of P/V_a vs. P can be used to calculate V_m and b. Then the specific surface area, S, can be computed from Equation 2.9.[112]

$$\frac{P}{V_a} = \frac{1}{V_m b} + \frac{P}{V_m} \qquad (2.8)$$

$$S = \frac{V_m \sigma N_A}{m V_0} \qquad (2.9)$$

In Equation 2.9, σ is area of the surface occupied by a gas molecule (16.2 x 10^{-20} m^2 for N$_2$), N$_A$ is the Avogadro constant, m is mass of the sample, and V$_0$ is molar volume of the gas (22414 cm^3 for N$_2$). Thus, the specific surface area in units of m^2/g can be obtained from Equation 2.10.[112]

$$S = \frac{4.35 V_m}{m} \qquad (2.10)$$

The Langmuir theory was further developed by Braunauer, Emmett, and Teller by incorporating the multilayer adsorption concept, which is known as BET theory.[112] To apply BET theory, the equation for V$_a$ is modified as given in Equation 2.11, where c is a constant and P$_0$ is the saturation pressure of the gas. Equation 2.11 can be re-arranged such that a plot of P/[V$_a$(P$_0$-P)] vs. (P/P$_0$) yield a straight line. V$_m$ and c are obtained from the intercept and the slope of the plot, and then the surface area can be calculated using Equation 2.10.

$$V_a = \frac{V_m c P}{(P_0 - P)[1 + (c-1)\frac{P}{P_0}]} \qquad (2.11)$$

Barrett, Joyner, and Halenda developed the BJH method to calculate pore size distributions.[112] The basis of the BJH method is the Kelvin equation, which treats pores as cylinders and assumes pore filling and emptying occur in a stepwise manner (Equation 2.12).[112] In Equation (2.12), P* and P$_0$ are the critical condensation and the saturation pressures, respectively, γ is the liquid surface tension, υ is the molar volume of the condensed adsorptive, θ

is the contact angle between the solid and the condensed phase (it is zero for N_2), r_m is the mean radius of curvature of the liquid meniscus, R is the ideal gas constant; and T is absolute temperature.

$$\ln \frac{P^*}{P_0} = \left(\frac{2\gamma\upsilon \cos\theta}{RTr_m}\right) \qquad (2.12)$$

Depending on the nature of the material there are six basic types of adsorption isotherms as shown in Figure 2.12. Type 1 is characteristic of microporous (< 2 nm) materials.[112] Types 2 and 4 isotherms are observed for either mesoporous (2-50 nm) or non-porous materials. When absorption molecules have a stronger affinity for each other than for the solid, Type 3 and 5 can be seen. Type 6 is indicative of a non-porous uniform surface.
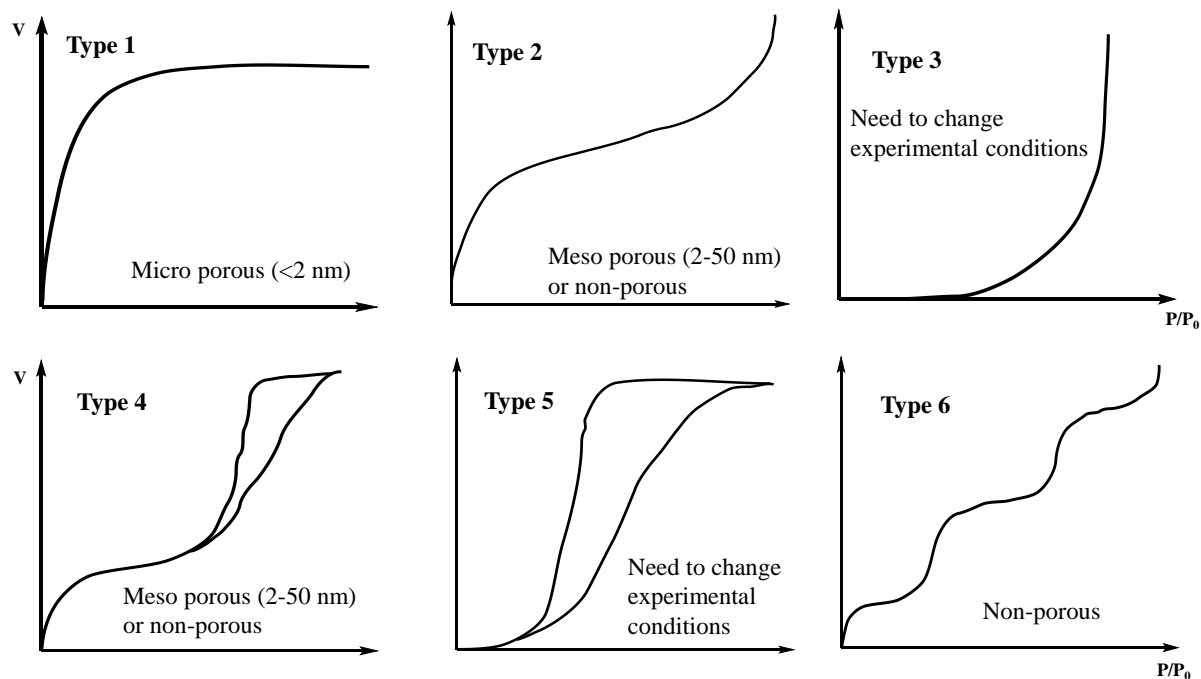
Figure 2.12 Types of adsorption isotherms (adapted from Webb)[112]

In this dissertation study a Micromeritics TriStarII 3020 surface area analyzer was used for surface area and pore size analysis. The surface areas of nanoparticles and aerogels were

obtained by applying the Brunauer-Emmett-Teller (BET) model to nitrogen adsorption-desorption isotherms acquired at 77 K. Samples were degassed at 150 °C for 24 h prior to the analysis. The Barrett-Joyner-Halenda (BJH) model was employed to analyze the pore size distribution of aerogels and silica encapsulated $Fe_xNi_{2-x}P$ nanoparticles.

2.3.3 Thermogravimetric Analysis (TGA)

Thermogravimetric analysis provides useful information about temperature-induced chemical and physical events such as decomposition, oxidation, vaporization, and sublimation. In TGA the sample is subjected to a programmed temperature profile under a specific atmosphere (inert gas, air, etc…) and the change in the sample mass as a function of temperature is measured. A typical TGA data plot is shown in Figure 2.13 revealing weight losses due to pyrolysis of organic ligands.
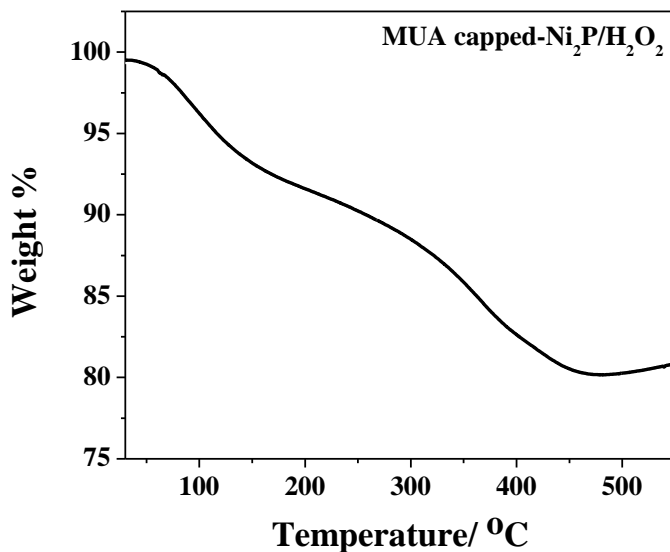
Figure 2.13 Thermogravimetric analysis of a Ni_2P aerogel produced by reaction of 11-mercaptoundeconoic acid (MUA)-capped Ni_2P nanoparticles with H_2O_2

In this dissertation research, a Perkin-Elmer Pyris 1 thermogravimetric analyzer was used to determine ligand decomposition temperature and weight losses of nanoparticles and aerogels. Samples were heated under nitrogen flow from 25 to 500 °C in a ceramic crucible with a temperature ramp rate of 10 °C/min.

2.3.4 X-Ray Photoelectron Spectroscopy (XPS)

X-ray photoelectron spectroscopy is a characterization technique used for determination of composition, oxidation state, and chemical environment of elements on the sample surface. The sample of interest is irradiated by monochromatic soft X-rays and the energy of the emitted electrons are analyzed. Mg (Kα = 1253.6 eV) and Al (Kα = 1486.6 eV) are the most commonly used X-ray target materials. Upon irradiation with X-rays, electrons will be ejected from different energy levels of the sample (Figure 2.14).[113] The kinetic energy (KE) of the ejected electrons is given in Equation 2.13, where $h\nu$ is the energy of the photon, BE is the binding energy of the atomic orbital of the electron, and ϕ is the spectrophotometer work function.

$$KE = h\nu - \text{BE} - \phi \tag{2.13}$$
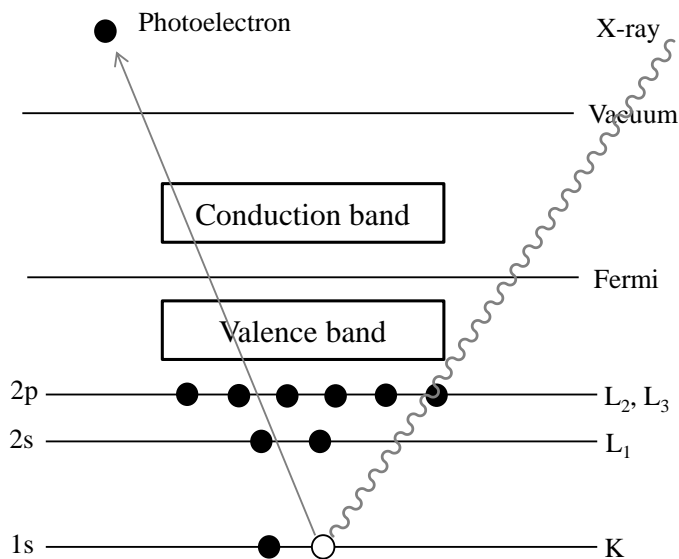
Figure 2.14 Schematic illustration of the XPS process (adapted from Skoog)[113]

Electron binding energy (in eV) vs. number of photo-electrons detected (intensity) is plotted in the XPS spectrum. An example of a survey XPS spectrum for an InP aerogels as well as the high resolution spectra for the 2p region are shown in Figure 2.15. These binding energies are characteristics for each element and can be used to identify the elements and their oxidation states.
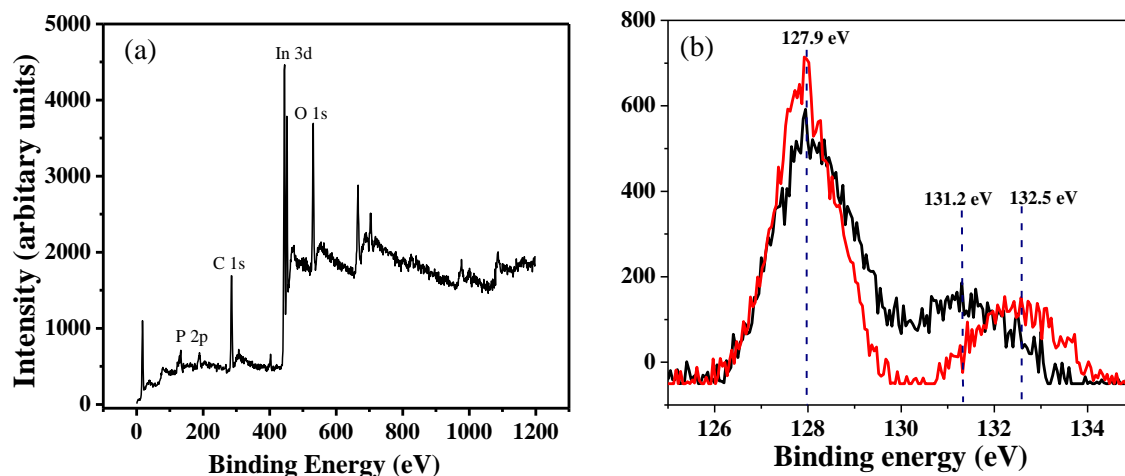
Figure 2.15 (a) XPS survey spectrum of an InP aerogel and (b) high resolution XPS spectra for P 2p region for InP nanoparticles (black line) and aerogel (red line)

In this dissertation work a PerkinElmer PHI 5500 with a monochromatic Al Kα X-ray radiation source (1486.6 eV) and Auger-Scan system control (RBD Enterprises, Bend, OR) was employed. The samples were prepared by pressing powder samples on to a piece of indium foil. Survey scans were collected to 1200 eV with a 1 eV/step resolution. High resolution scans were collected over the range 125-137 eV (for P 2p) and 440-448 eV (for In 3d). The binding scales were adjusted to the C 1s peak of graphite (present as a background signal in the spectrometer) at 284.6 eV. To prevent any possibility of adventitious oxidation of nanoparticles and aerogels, the samples were handled under air free conditions except for the rapid transfer to the XPS chamber.

2.3.5 Inductively Coupled Plasma-Mass Spectrometry (ICP-MS)

Inductively Coupled Plasma-Mass Spectrometry is a technique used for elemental analysis. The low detection limits (parts per billion), high accuracy and precision, selectivity, and ability to analyze multiple analytes simultaneously are key advantages of ICP-MS over other

elemental analysis techniques. A typical ICP-MS consists of two main components; (a) ICP source and (b) mass spectrometer. The ICP torch is connected to a radio frequency generator. When the power is supplied, the argon gas passing through the ICP torch gets ionized, due to the collision of these ions with other argon atoms, an argon plasma is generated. The sample to be analyzed is introduced into the plasma as an aerosol. Elements in the sample are converted into gaseous atoms and then into ions. The generated ions are separated by mass and detected by the mass spectrometer. The ions formed in ICP are typically positive. Thus this technique is more suitable for analysis of elements that form positive ions.

In this dissertation study an Agilent 7700 ICP-MS instrument was used to determine elemental compositions of $Fe_xNi_{2-x}P$ nanoparticles and $Fe_xNi_{2-x}P@mSiO_2$ core@shell nanoparticles. The samples were digested in concentrated nitric acid and diluted with nano pure water. An external standard series was used for calibration.

2.3.6 Magnetic Susceptibility Measurements

Superconducting Quantum Interference Device (SQuID) technology to perform DC magnetization measurement. A magnetometer is used to measure magnetic properties such as magnetization and magnetic susceptibility. The SQuID detector combines the physical phenomena of flux quantization and Josephson tunneling. In DC SQuID two superconductors are separated by thin insulating layers, which will result in formation of two parallel Josephson junctions. The superconductor can be made of lead/gold or lead/indium alloy or pure niobium.

A schematic drawing of a DC SQuID is shown in Figure 2.17. There are two Josephson junctions in the DC SQuID. In the absence of an applied magnetic field, the input current I splits into the two Josephson junctions equally. Therefore the current flow in each branch is $I/2$ and they flow in opposite directions. When an external magnetic field is applied, a screening current

I_s begins to flow. As a result, a magnetic field will be generated, which will cancel the applied field. The generated current, I_s, is in the same direction as one of the currents flowing in the loops. Thus, the total current flows in the two loops are $I/2 + I_s$ and $I/2 - I_s$. When the total current in either of the loops exceeds the critical current, I_c, a voltage appears across the junction. Since flux is quantized, when the external flux is increased until it reaches $\phi_0/2$, the magnetic flux quantum SQuID prefers to increase the flux to reach ϕ_0 by changing the direction of screening current. Therefore the current oscillates as a function of the applied flux and hence voltage (V=IR, where V is voltage, R is resistance, and I is current). Therefore by measuring the change in voltage, the change in flux can be estimated and this is the basis of SQuID.
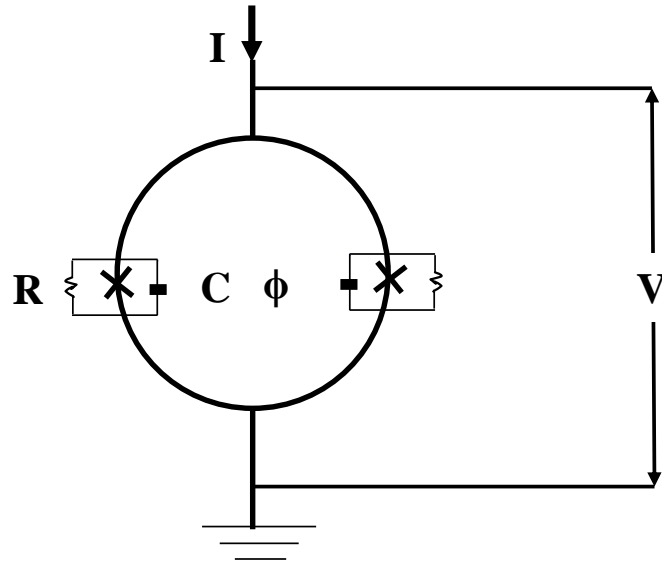
Figure 2.16 Schematic of a DC SQUID magnetometer (adapted from Clarke)[114]

In DC magnetization measurements, the magnetization (M) of the sample is measured in an applied field (H) at a specific temperature (T). In the process of the measurement, the sample is moved through a set of copper coils and the induced signal is analyzed. AC susceptibility measurements do not directly measure magnetic moments of the sample. Since samples with very different magnetic moments and the same susceptibilities can show a similar response to

changes in the magnetic field, during AC susceptibility measurements in addition to the large applied field a small alternating magnetic field is applied. Both the amplitude and the phase of the magnetic moment are recorded. The susceptibility (χ) is given by the ratio of the change in magnetic moment (*dM*) and the amplitude of the change in moment by the amplitude of the alternating field (*dH*).

In this dissertation research a Quantum Design PPMS, Model 6000 controlled by PPMS MultiVu software with ACMS option was employed for DC magnetization and AC susceptibility measurements. Powder samples of $Fe_xNi_{2-x}P$ nanocrystals (previously stored under inert atmosphere) were placed on a silica capsule. Temperature dependent DC magnetization measurements were acquired under zero-field-cooled (ZFC) and field-cooled (FC) conditions from 50 to 350 K in an applied magnetic field of 1000 Oe. Arrott plots were generated near the expected Curie temperature (T_C) range to identify T_C.

2.3.7 **Mössbauer Spectroscopy**

Mossbauer spectroscopy measurements were carried out in Dr. Takela Seda's laboratory at Western Washington University. A constant-acceration spectrometer (Wissel GMBH, Germany) with a source in a horizontal transition mode with a 50 mCi Co source was employed to record Mössbauer spectra of $Fe_xNi_{2-x}P$ nanoparticles. The spectra were acquired at room temperature and approximately 0.03 g of sample was used in each composition. The time require for data acquisition vary depending on the iron content of the sample. To normalize velocity scale metallic iron was used. NORMOS (WISSEL GMBH) least-square fitting program was employed for Mössbauer spectra fitting. The fractional occupancy of two metal sites, M(1) and M(2) was determined from peak areas of fitted quadruple sub-spectra corresponding to two metal sites.

CHAPTER 3

SYNTHESIS AND CHARACTERIZATION OF DISCRETE $Fe_xNi_{2-x}P$ NANOCRYSTALS: COMPOSITIONAL EFFECTS ON MAGNETIC PROPERTIES

3.1 Introduction

Iron phosphides exist in a wide range of stoichiometries (Fe_3P, Fe_2P, FeP, FeP_2, and FeP_4) and they show distinct properties depending on the phase.[20] As previously described in Chapter 1, Fe_2P is ferromagnetic and potentially useful in magnetic refrigeration if the Curie temperature, T_C, can be augmented to near room temperature. One way to achieve this is to dope with Ni. Even though $Fe_xNi_{2-x}P$ is known to exist over all x in the bulk, the synthesis of nanoscale ternary $Fe_xNi_{2-x}P$ phases with control of composition is challenging due to the fact that metal precursors can react at different rates giving rise to phase segregation or inhomogenities in the solid solution formation from one particle to the next. Thus, there are few reports on the synthesis of discrete ternary iron-nickel phosphide nanocrystals in the nano regime, and they are limited to few selected stoichiometries.[58] This chapter discusses in detail the synthesis of unsupported discrete ternary $Fe_xNi_{2-x}P$ phases as well-formed nanoparticles with control of size, shape, and composition. The magnetic properties are also reported for Fe-rich $Fe_xNi_{2-x}P$ (x= 0. 2, 1.4, and 1.8) nanoparticles and compared to bulk materials.

I performed the synthesis and characterization of $Fe_xNi_{2-x}P$ nanoparticles and magnetic property measurements were carried out by Maheshika Perera (in the group of Gavin Lawes) in the Department of Physics and Astronomy at Wayne State University. Mössbauer spectroscopy measurements were collected and interpreted by Prof. Takele Seda in the Department of Physics and Astronomy at Western Washington University.

3.2 Experimental

All the chemicals used in this Chapter are listed in Chapter 2.1.

3.2.1 Synthesis of $Fe_xNi_{2-x}P$ Nanoparticles

Reactions were carried out under argon using standard Schlenk line techniques as shown in Scheme 3.1. To synthesize ternary phases of $Fe_xNi_{2-x}P$, stoichiometric amounts of nickel precursor (nickel(II) acetylacetonate) and iron precursor (iron(0) pentacarbonyl) were used. In a typical synthesis, $Ni(acac)_2$ (2-x moles) was combined with trioctylphosphine (TOP), octylether and oleylamine and heated at 230 °C under argon atmosphere to form precursor particles of Ni-P. In the second stage of the reaction, $Fe(CO)_5$ (x moles) was introduced and heating was continued at 230 °C to form Fe-Ni-P alloy particles. The temperature of the reaction was raised to 350 °C and the reaction was heated for an additional 10 h for the subsequent conversion of precursor nanoparticles into crystalline phosphide phases. After cooling the reaction mixture to room temperature, the nanoparticles were isolated by precipitation with excess ethanol followed by centrifugation. Isolated nanoparticles were dispersed in chloroform (2 mL) with sonication, re-precipitated with ethanol (30-40 mL) and centrifuged. This process was repeated two more times, after which the nanoparticles were dried under active vacuum to obtain a free flowing powder.

Scheme 3.1 Synthesis of $Fe_xNi_{2-x}P$ nanoparticles
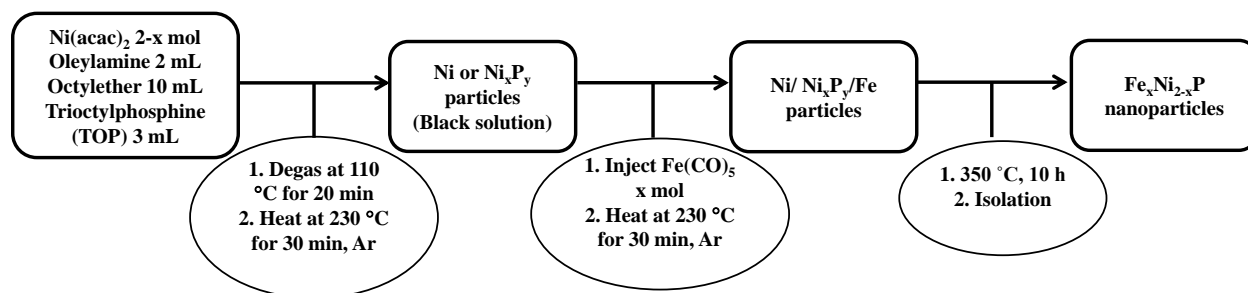
3.3 Results and Discussion

3.3.1 Synthesis of $Fe_xNi_{2-x}P$ Nanoparticles

To study the structure and morphology evolution of $Fe_xNi_{2-x}P$ six compositions were targeted: x=0.2, 0.8, 1.0, 1.2, 1.4, and 1.8. Previously reported syntheses of Ni_xP_y (Ni_2P and $Ni_{12}P_5$) by Brock and co-workers occur via formation of intermediate precursor particles at a lower temperature from the reaction of $Ni(acac)_2$ with trioctylphosphine (TOP), followed by conversion into the relevant crystalline phosphide phase by increasing temperature.[49] In our ternary $Fe_xNi_{2-x}P$ nanoparticle synthesis, we followed a similar approach. This synthesis procedure involves three steps: (a) synthesis of crystalline Ni or amorphous Ni_xP_y intermediate particles (IP-1), (b) injection of an $Fe(CO)_5$ precursor to form amorphous Ni-Fe-P alloy intermediate particles (IP-2), and (c) conversion of IP-2 into crystalline $Fe_xNi_{2-x}P$ nanoparticles. Previous studies on the Ni_xP_y system revealed that for a solution with a fixed number of moles of oleylamine (OA) to metal ratio (OA:Ni=3.0) changing the P:Ni ratio by changing the TOP amount leads to formation of Ni_xP_y alloy particles when the P:Ni ratio is larger than 2.24, whereas formation of crystalline Ni particles occurs at lower concentrations. Higher P:Ni ratios tended to produce smaller intermediate particles (ca. 10.2±0.9 nm) whereas lower P:Ni ratios lead to larger intermediate particles (ca. 26.8±1.9 nm). The larger phosphide particles that result at lower P:Ni ratios are also subject to formation of hollow cores via the Kirkendall effect. Higher P:Ni ratios favor the more P-rich phase in the crystallized product (Ni_2P). For the synthesis of $Fe_xNi_{2-x}P$ the initial P: Ni ratio was kept above 3.4 in all cases to prevent formation of more nickel-rich impurity phases and OA:Ni molar ratio was varied over the range 2.4-22. The PXRD pattern of IP-1 for the $Fe_{1.0}Ni_{1.0}P$ targeted composition is shown in Figure 3.1a (OA:Ni=4.35; P:Ni=6.8). Crystalline fcc-Ni has three characteristic peaks (44°, 52°, and 67°

corresponding to (111), (200), and (220) reflections). For IP-1, only a single reflection corresponding to the (111) is observed, suggesting amorphous Ni_xP_y alloy particles have formed in the first stage of the reaction. IP-1 particles are spherical with narrow polydispersity and an average particle size of 9.44 ± 0.68 nm (Figure 3.1b and c). According to in situ EDS in TEM, both Ni and P are present even after washing the product three times (Table 3.1). However, washing did reduce the phosphorous associated with IP-1, presumably due to removal of residual TOP from the particle surface. The fact that significant P remains is consistent with Ni-P alloy formation. Moreover, IP-1 did not show any response to a magnet, which again suggests formation of amorphous Ni-P alloy particles instead of super-paramagnetic Ni particles. At the second stage of the reaction, after injecting Fe precursor and heating at 230 °C for 30 min, IP-2 exhibited a similar PXRD pattern (Figure 3.1d) to IP-1. However, Ni, Fe, and P were all detected by EDS suggesting formation of alloy particles of Ni-Fe-P (Table 3.1). Moreover, the incorporation of Fe resulted in materials that were attracted to a magnet (magnetic stir bar) suggesting formation of a ferro- or ferrimagnetic phase. The IP-2 particles remained spherical and their average particle size was 9.54 ± 0.66 nm (Figure 3.1e and f). In the final step, the reaction mixture was heated at 350 °C for 10 h for the complete conversion of IP-2 into crystalline phosphide phases. The chemical composition of the product phases was determined by EDS.
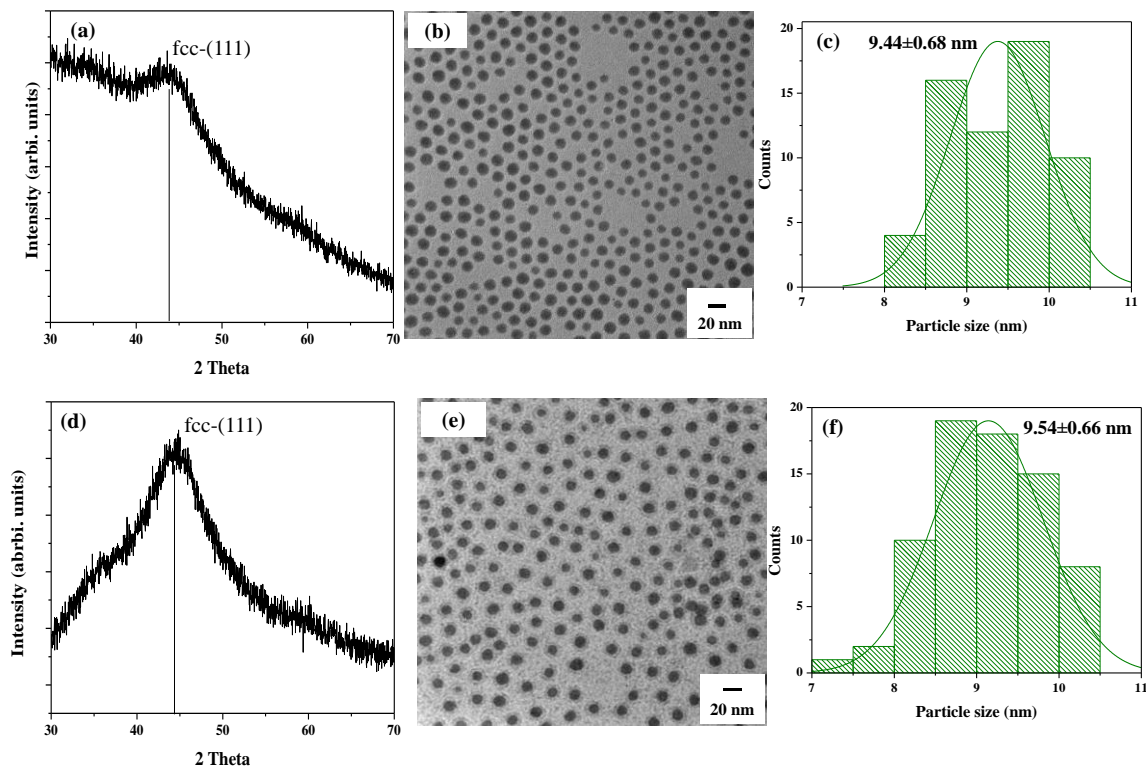
Figure 3.1 (a) and (d) PXRD patterns, (b) and (e) TEM micrographs, and (c) and (f) particle size distributions of IP-1 and IP-2 (x=1.0, OA:Ni=4.35, and P: Ni=6.8)

Table 3.1 EDS compositions of intermediate particles (x=1.0)

Sample	Fe	Ni	P
IP-1 as prepared	–	51.6	48.4
IP-1 after washing	–	60.4	39.6
IP-2 after washing	17.7	45.1	37.2
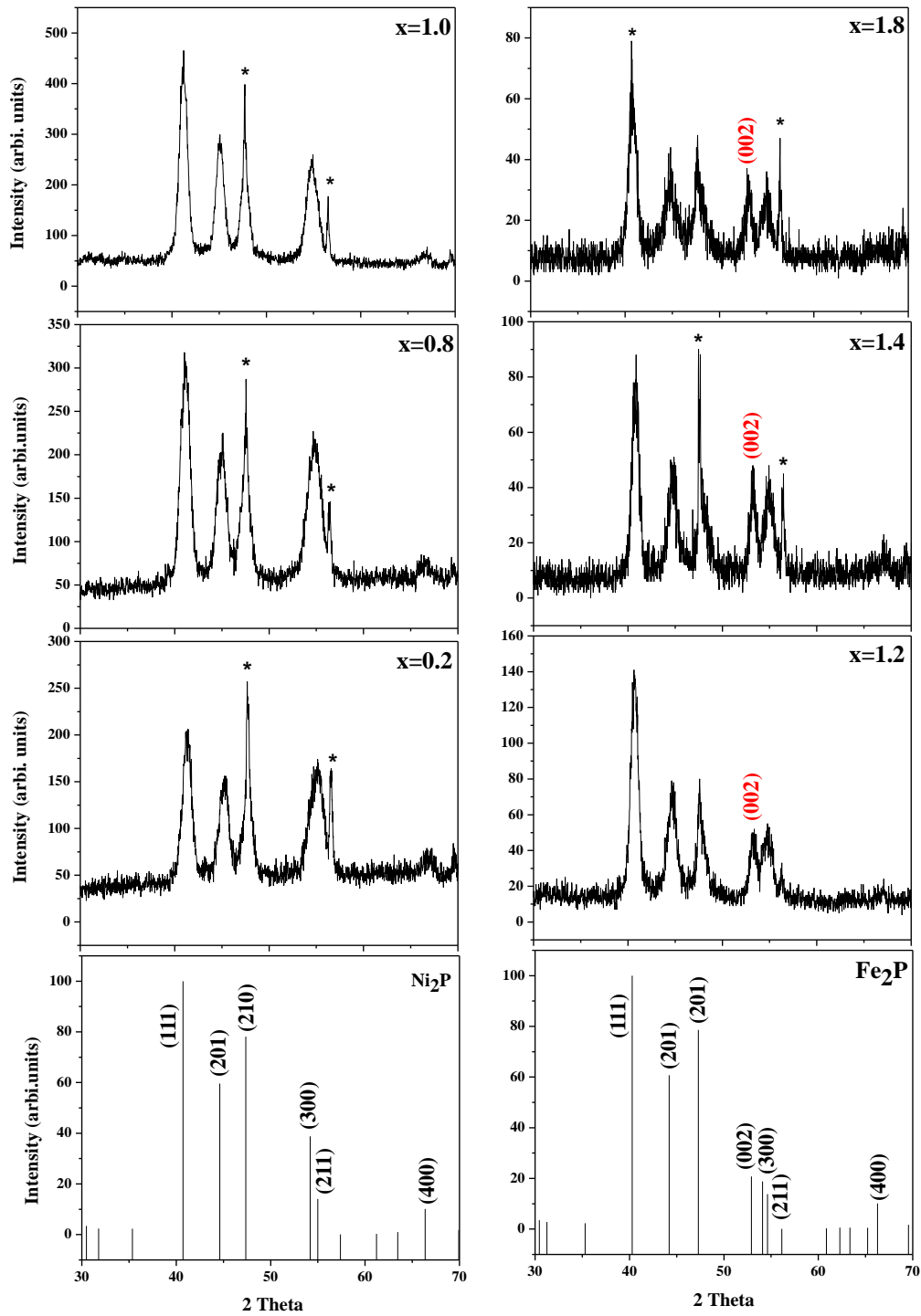
Figure 3.2 PXRD patterns for $Fe_xNi_{2-x}P$ nanocrystals (x=0.2, 0.8, 1.0, 1.2, 1.6, and 1.8) and ICSD-PDF reference patterns for Ni_2P (74-1385) and Fe_2P (85-1727)

3.3.2 Crystal Structure and Morphology

As for Ni_2P and Fe_2P, the $Fe_xNi_{2-x}P$ phases crystallize in the hexagonal Fe_2P structure-type (P62m space group). Figure 3.2 shows the PXRD patterns for x = 0.2, 0.8, 1.0, 1.2, 1.4, and 1.8 compositions along with Ni_2P and Fe_2P ICSD-PDF reference patterns. As x is increased to 1.2 or above, the appearance of the (002) peak, observed in Fe_2P but not in Ni_2P, but otherwise the patterns are very similar. The refined lattice constants for ternary nanoparticles were calculated by using high intensity PXRD peaks calibrated using an internal silicon standard. For x<1.2, peaks corresponding to the (111), (201), (300), and (400) planes were refined, whereas for x≥1.2, the (111), (201), (002), and (300) planes were refined. Lattice refined data are shown in the Table 3.1 along with the targeted and observed (by EDS analysis of Fe and Ni). The data showed a decrease in *a* (and *b*) and increase in *c* as x is increased (Figure 3.3). The overall change in *a* was smaller than for *c* (40 pm vs. 135 pm). A similar trend has been reported for bulk $Fe_xNi_{2-x}P$ system. The lattice parameters did not exhibit the linear behavior that would be expected for an alloy, which would obey Vegard's Law. This deviation from Vegard's Law has been reported for both bulk and nano $Fe_xNi_{2-x}P$ solid solutions and is attributed to an unequal distribution of the two different metals in the two sites.

The M(1) site has a tetrahedral geometry and the M(2) site has a square pyramidal geometry. Both Fe_2P and Ni_2P have similar lattice parameters, but the atomic radius of Ni is slightly smaller than that of Fe (121 pm vs 125 pm). Among the two available sites, the tetrahedral M(1) site (223 pm) is smaller than the square pyramidal M(2) site (243 pm). Ni would normally be expected to occupy the smaller M(1) site; however, composition-dependent site occupancy of Fe for $Fe_xNi_{2-x}P$ suggests that for low Fe metal fractions, the pyramidal site is preferentially occupied by Ni (Figure 3.4).[55] The atypical site preferences in bulk ternary Fe_xNi_{2-}

$_x$P phases were previously observed and Goodenough hypothesized that electron transfer from Fe to Ni may be the reason for Ni's preferred occupancy of the larger M(2) square pyramidal site.[72] X-ray photoelectron spectroscopy (XPS) and X-ray absorption near-edge spectroscopy (XANES) investigations of the $Fe_xNi_{2-x}P$ system have revealed that the electron density of Ni atoms has been increased due to the electron transfer from Fe to the more electronegative Ni atoms, consistent with this hypothesis. Mössbaure data collected on the $Fe_xNi_{2-x}P$ samples prepared in the dissertation research revealed that, Fe preferentially occupies M(1) sites when x<0.8; otherwise, Fe shows a slight preference for M(2) sites (Figure 3.4b). For example, 30% of Ni atoms in $Fe_{0.1}Ni_{1.9}P$ are observed to occupy M(1) sites whereas 63% of Ni is in M(1) sites for $Fe_{1.0}Ni_{1.0}P$. A further decrease in the Ni amount resulted in an increase in Fe occupancy of the M(2) site, and the site distributions get close to parity as x approaches 2 (45% Fe in M(1) sites for x=1.9). This trend closely mirrors the trend observed $Fe_xNi_{2-x}P_y$ prepared by the TPR method (Figure 3.4b).[55]

Table 3.2 Compositions, lattice parameters and crystallite sizes of $Fe_xNi_{2-x}P$ nanoparticles

Targeted composition	Actual composition	a (Å)	c (Å)	Scherrer crystallite size for (111) peak (nm)
$Fe_{0.3}Ni_{1.7}P$	$Fe_{0.2}Ni_{1.8}P$	5.813(09)	3.338(19)	9.4±0.2
$Fe_{0.9}Ni_{1.1}P$	$Fe_{0.8}Ni_{1.2}P$	5.807(02)	3.320(03)	9.4±0.4
$Fe_{1.0}Ni_{1.0}P$	$Fe_{1.0}Ni_{1.0}P$	5.812(09)	3.334(15)	9.2±0.6
$Fe_{1.2}Ni_{0.8}P$	$Fe_{1.2}Ni_{0.8}P$	5.783(11)	3.437(05)	10.5±0.5
$Fe_{1.5}Ni_{0.5}P$	$Fe_{1.4}Ni_{0.6}P$	5.775(12)	3.443(05)	15.5 (>10)
$Fe_{1.9}Ni_{0.1}P$	$Fe_{1.8}Ni_{0.2}P$	5.772(18)	3.473(08)	14.8 (>10)
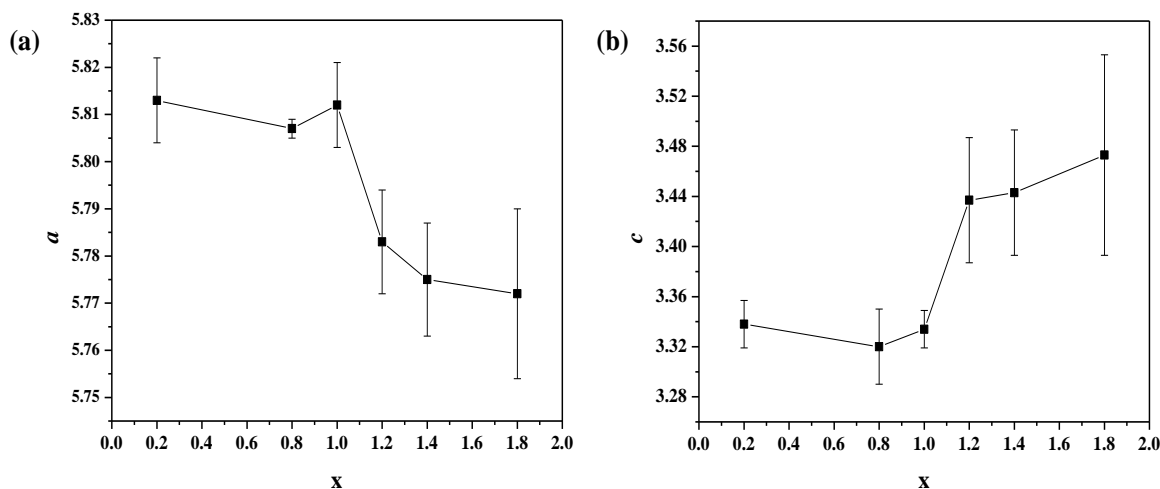
Figure 3.3 Lattice parameters (a) *a* and (b) *c* of $Fe_xNi_{2-x}P$ nanoparticles as a function of x

TEM analyses of $Fe_xNi_{2-x}P$ nanoparticles showed distinct composition-dependent morphologies. As seen in Figures 3.5 and 3.6, with the increase in the amount of Fe incorporation (x≥1.2), nanocrystals transition from a sphere to a rod morphology. Likewise, as the Fe content of the ternary phosphide phase increases, greater polydispersity is seen in the rod length while less polydispersity was observed in the width of nanorods (Figure 3.6). Hyeon and co-workers observed that Fe_2P and $Fe_xNi_{2-x}P$ (x>1.5) rods grow along the [001] direction.[45, 58] Their explanation was that TOP preferentially binds to lattice planes that are perpendicular to the (00*l*) planes, and as a result, rods are growing along the [00*l*] direction. This was further confirmed by the requirement of having an optimum amount of TOP for rod formation; below that amount, formation of spherical particles has been reported. We presume a similar effect is occurring in our case. When x≤1.2 spherical monodisperse nanoparticles are formed with an average particle size of ~11 nm and standard deviation of less than 10%. The crystallite sizes calculated corresponding to the (111) plane showed an average size ~9.5-10.0 nm with less than

10% standard deviation for x≤1.2. When x>1.2 an increase in both the crystallite size and the polydispersity of the nanoparticles were observed which probably reflects the anisotropy in the crystal shape. The average particle diameters were larger by 10-20% than the crystallite sizes determined by PXRD.
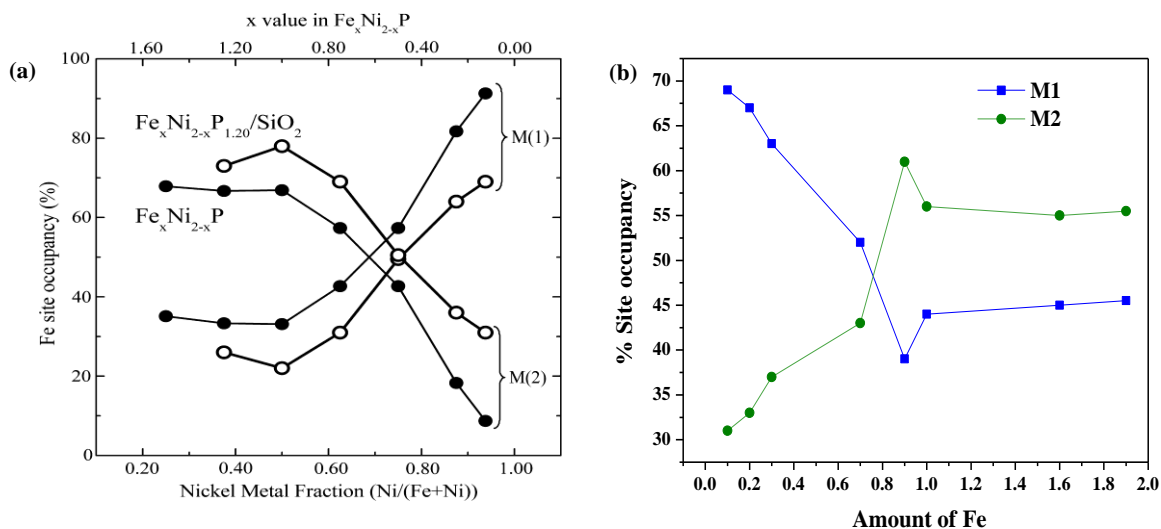
Figure 3.4 Site preferential occupancy of Fe in M(1) and M(2) sites in the hexagonal crystal structure as assessed by Mössbauer spectroscopy (a) unsupported and supported $Fe_xNi_{2-x}P$ prepared by the TPR method and (b) $Fe_xNi_{2-x}P$ (Copyright 2014, Elsevier)[55]
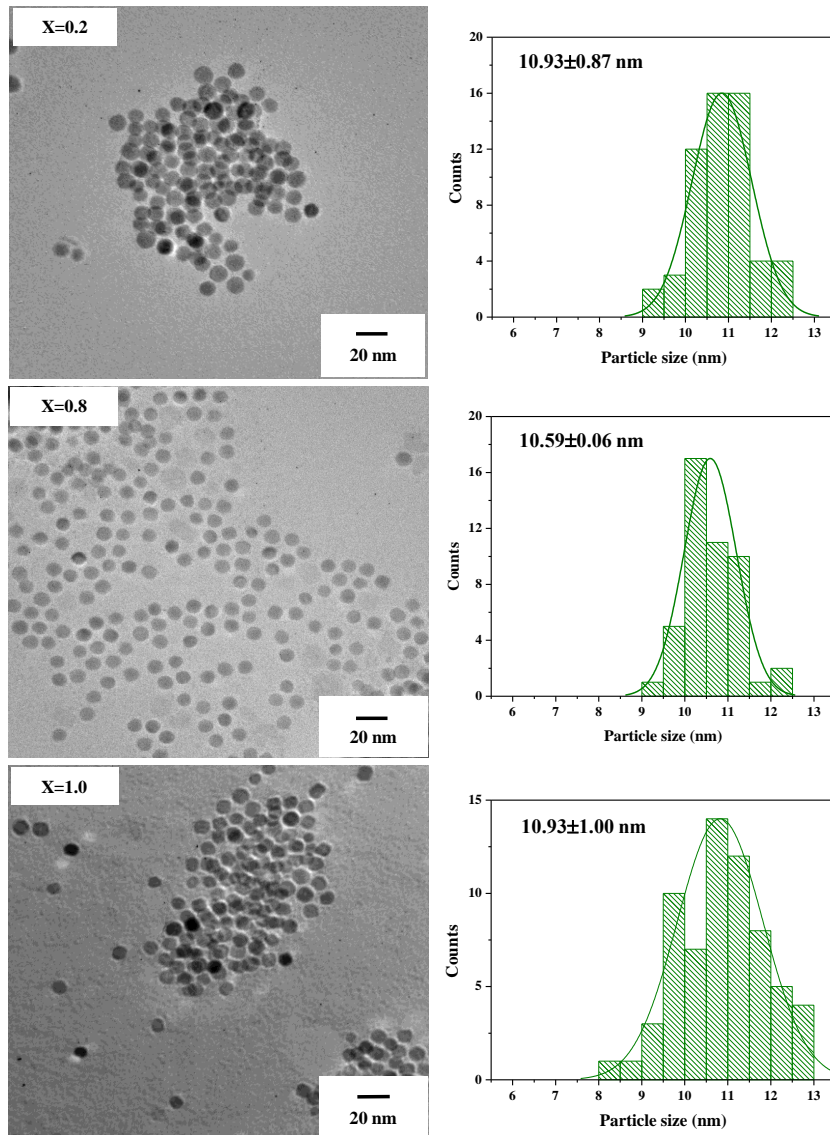
Figure 3.5 TEM micrographs and particle size distributions of $Fe_xNi_{2-x}P$ nanoparticles for x=0.2, 0.8, and 1.0)
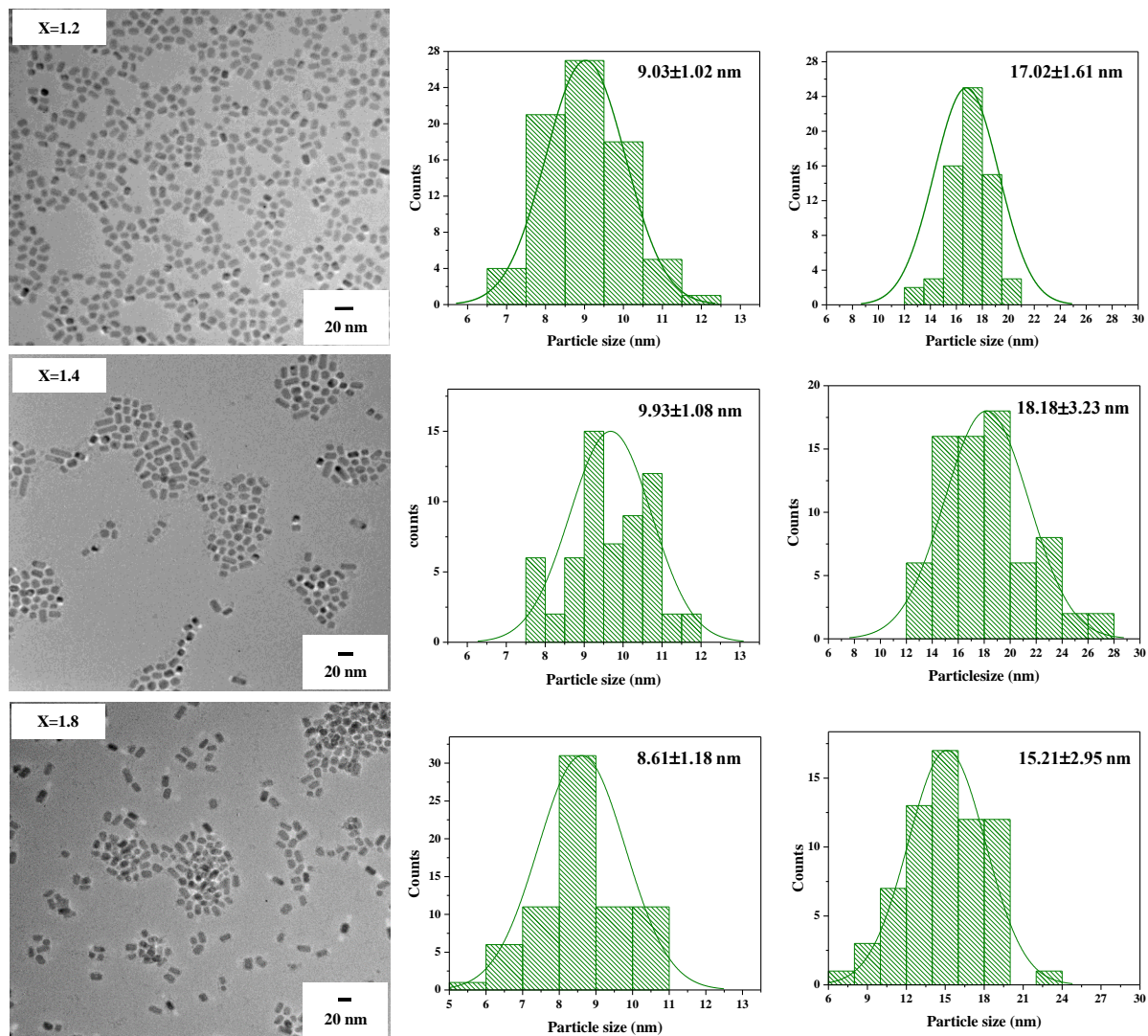
Figure 3.6 TEM micrographs and particle size distributions of $Fe_xNi_{2-x}P$ nanoparticles for x=1.2, 1.4, and 1.8)

3.3.3 The Effects of the Nature and Sequence of Addition of Metal Precursor on Homogeneous Phase Formation

Initial attempts to prepare ternary nanocrystals focused on substitution of some $Fe(acac)_3$ $Ni(acac)_2$. However, the use of $Fe(acac)_3$ led to formation of iron oxide phases (Figure 3.7). Although the synthesis of Fe_2P using $Fe(acac)_3$ has been reported with

tris(trimethylsilyl)phosphine as the phosphorous precursor, use of the less reactive (and less expensive) trioctylphosphine is typically done with a reduced Fe-source ($Fe(CO)_5$).[43, 45] Accordingly, combination of the metal precursors $Ni(acac)_2$ and $Fe(CO)_5$ with TOP was attempted (350 °C, 3-10 h). PXRD analysis of the product showed a material with Fe_2P-type structure was formed (Figure 3.8a). TEM analyses of the sample looking at different areas of same grid revealed formation of both nanorods and nanoparticles with inconsistent chemical compositions (probed by EDS), as shown in Figure 3.8. Notably, even though the targeted Fe:Ni ratio was 1:1, the sample was Fe rich and some areas had no observable Ni at all. The phase separation and inhomogeneity can be attributed to the different reactivities of the two metal precursors, with $Ni(acac)_2$ being considerably less reactive compared to $Fe(CO)_5$, leading to Ni poor samples. Accordingly, the synthetic procedure was modified by introducing $Fe(CO)_5$ after formation of the precursor particles at 230 °C (IP-1). These precursor particles served as a template for ternary nanoparticle formation.
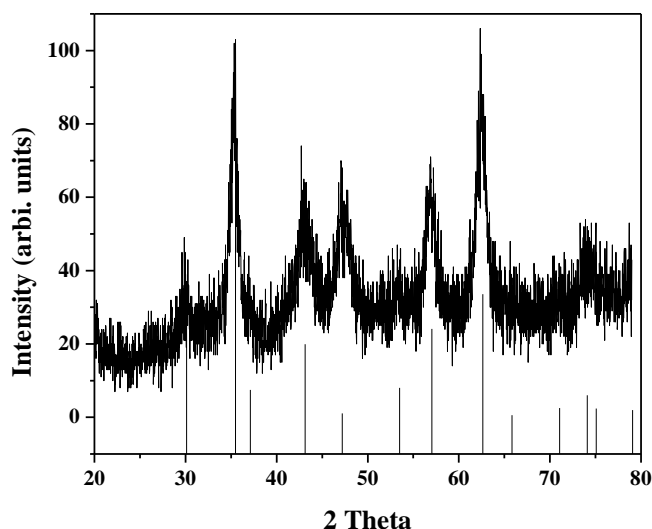
Figure 3.7 PXRD pattern of sample prepared using $Fe(acac)_3$ and $Ni(acac)_2$ with TOP (x=1.0). The vertical lines are correspond to the ICSD-PDF pattern for Fe_3O_4 (75-0033)
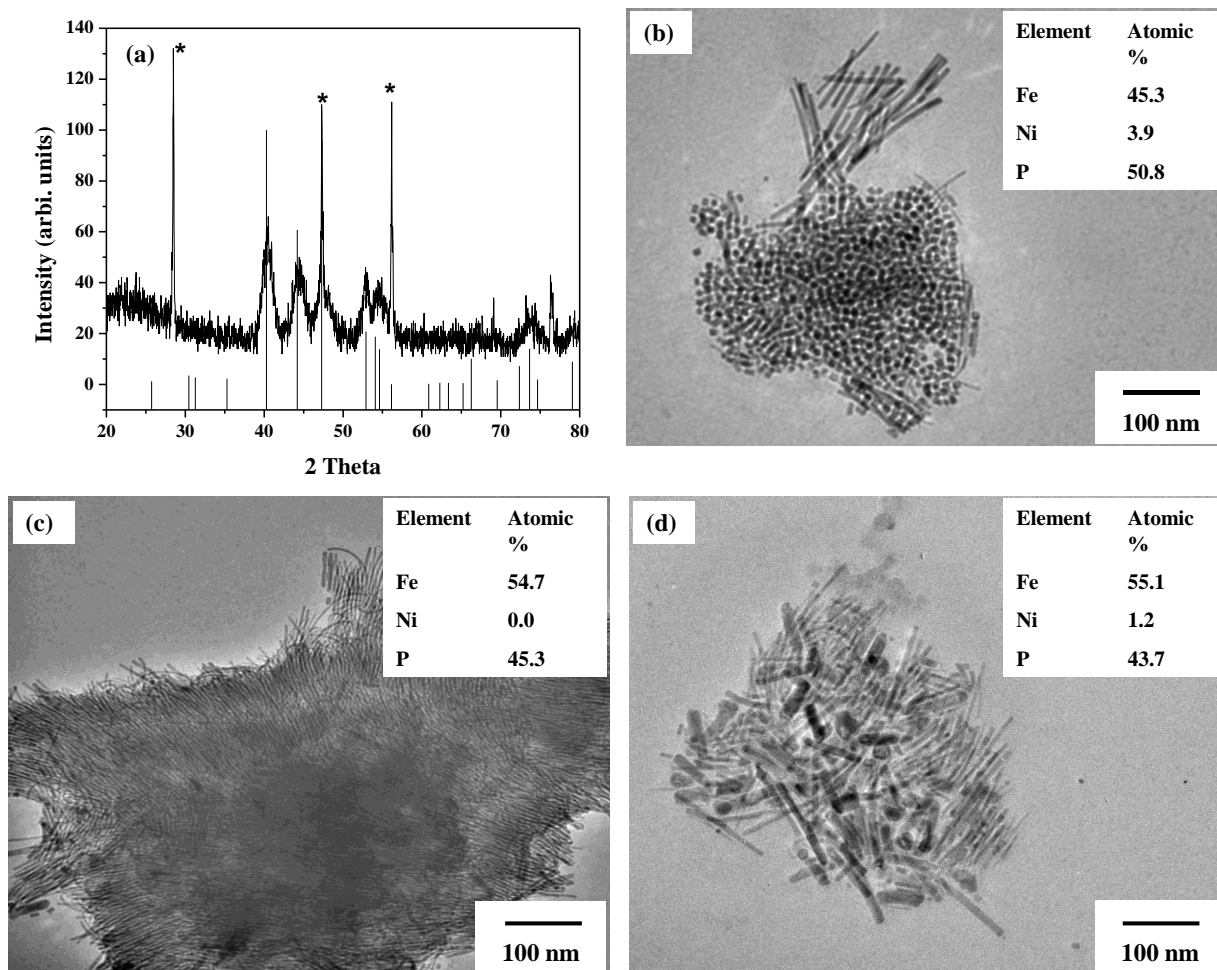
Figure 3.8 (a) PXRD pattern, (b)-(d) TEM micrographs (different areas of the same grid) of nanoparticles prepared by taking both Fe(CO)$_5$ and Ni(acac)$_2$ with TOP together for x=1.0. Insets of (b)-(d) show EDS analyses of the corresponding area. Peaks in PXRD marked with * are from the internal Si standard

3.3.4 The Evolution of Rod Morphology

In order to understand how spherical nanoparticles of IP-1 convert to crystalline nanorods of Fe$_x$Ni$_{2-x}$P when x≥1.2, aliquots of the reaction mixture (x=1.3) were taken at specified time

intervals while heating at 230 and 350 °C. The TEM images of aliquots that were taken at 230 ℃ before and after $Fe(CO)_5$ injection showed a spherical morphology (Figure 3.9a and b). When the temperature was raised to 350 ℃, irregular shaped and hollow particle formation was observed (Figure 3.9c) due to the phosphide formation through the Kirkendall effect. The PXRD of the aliquot taken after heating at 350 ℃ for 1 h showed Fe_2P-type crystal structure but with no (002) evident (Figure 3.9f).When the reaction mixture was further heated, TEM analyses showed transformation of the irregular shaped hollow particles into short rods and longer rods (Figure 3.9d and e). The (002) reflection, indicative of formation of more Fe-rich phases appeared after heating for 2-3 h (Figure 3.9g and h). In addition to changes in crystal structure and morphology, the amount of Fe incorporation also changed during the heating (Figure 3.9). As the reaction time at 350 ℃ increases, the Fe incorporation increased until the targeted value (x=1.3). Further heating beyond 10 h did not lead to an increase the amount of Fe, suggesting Fe was completely depleted by nanoparticle formation.
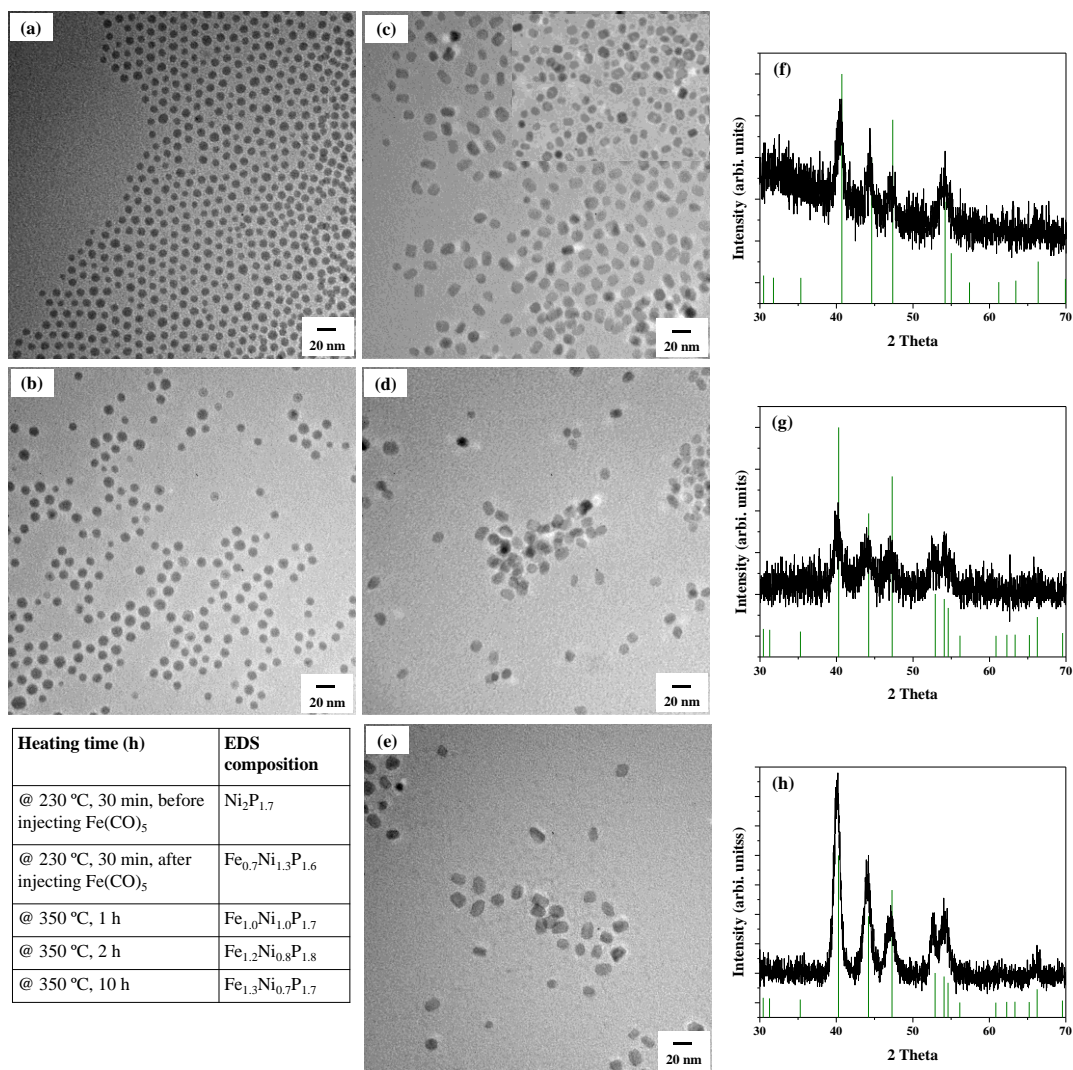
Figure 3.9 TEM micrographs of $Fe_{1.3}Ni_{0.7}P$ particles heating at (a) 230 ºC, 30 min, (d) 230 ºC, 30 min after $Fe(CO)_5$ injection, (b) 350 ºC, 1 h, (e) 350 ºC, 2 h, and (g) 350 ºC, 1 h. The table shows the variation in chemical composition of nanoparticles over time. PXRD patters after heating at 350 °C for (f) 1 h, (g) 2 h, and (h) 3h.

To study whether we are able to tune the rod diameter and/or aspect ratio for x≥1.2 phases, P:M ratio was varied while maintaining the same OA:M ratio (2.2). To eliminate possible effects from dilution, excess octylether was added. As the P:M increases, the average

nanorod length and width decreased and the aspect ratios increased (Figure 3.10). When 3 mL (6.72 mmol) of TOP (P:M=3.4) is used, nanocrystals were formed with several different morphologies and varying sizes with a relatively low aspect ratio (1.6) (Figure 3.10a). The use of 5 mL (11.2 mmol) of TOP (P:M=5.6) or 7 mL of TOP (P:M=7.8) reduced resulted in increased aspect ratio (2.3-2.4) and improved the monodispersity of the nanorods by decreasing the standard deviation (Figure 3.10 b and c). Further addition of TOP resulted formation of the more phosphorous rich FeP phase. The decrease in rod length and width as P:M ratio increases may be due to the stabilization of nuclei by excess TOP leading to form smaller particles.
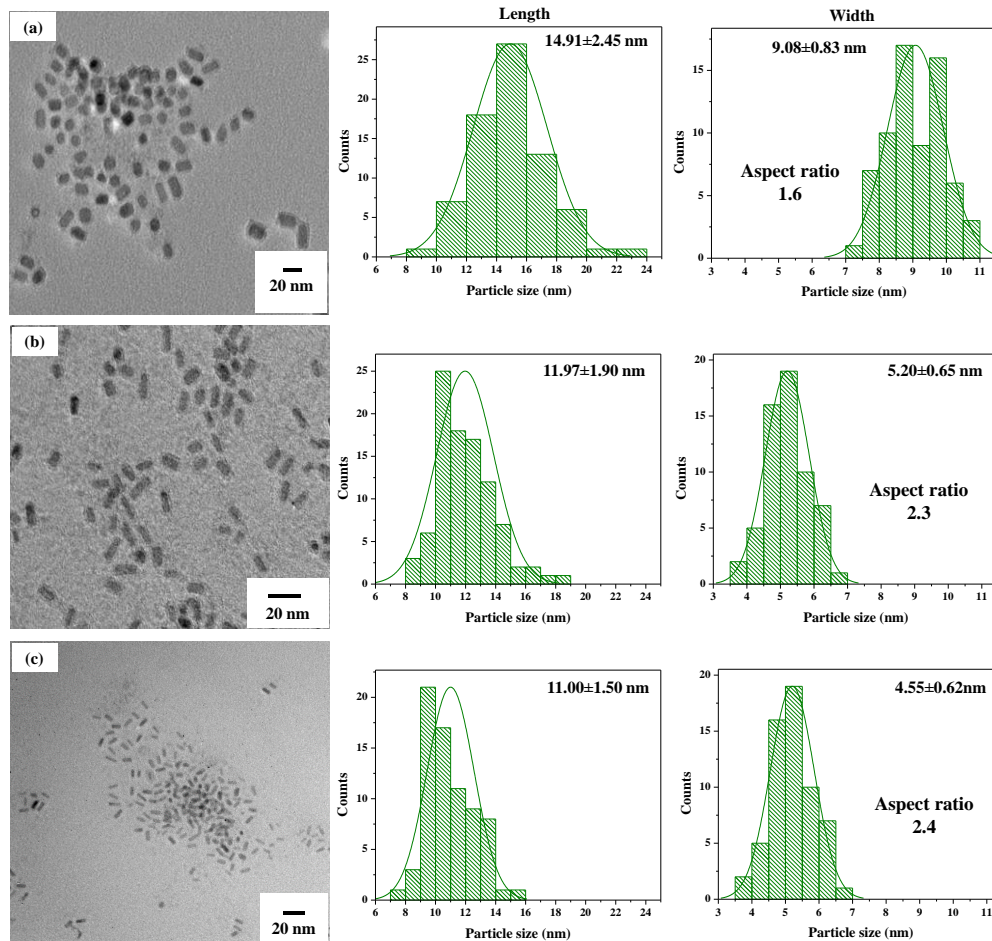
Figure 3.10 TEM micrographs of $Fe_{1.7}Ni_{0.3}P$ nanoparticles (a) 3, (b) 5, and (d) 7 mL of TOP were used

3.3.5 Magnetic Properties of $Fe_xNi_{2-x}P$ Nanoparticles

Motivated by the augmented T_C (>217 K for Fe_2P) as Ni is incorporated into $Fe_xNi_{2-x}P$ for x≥1.4, nanoparticles with compositions on the Fe-rich (x=1.8) and Fe-poor (x=1.2) end of this cut off, as well as x=1.4, were prepared with similar sizes and aspect ratios and their magnetic properties investigated (Table 3.3). Figure 3.11 shows the temperature (T) dependence of the magnetization (M) recorded under zero-field-cooled (ZFC) and field-cooled (FC) conditions in the temperature range 50-350 K under an external magnetic field of 1000 Oe for $Fe_{1.4}Ni_{0.6}P$ and $Fe_{1.8}Ni_{0.2}P$. Both samples showed maxima in their ZFC curves near the intersection of the FC with the ZFC and their blocking temperatures (T_B) were 200 and 185 K for $Fe_{1.4}Ni_{0.6}P$ and $Fe_{1.8}Ni_{0.2}P$, respectively. For $Fe_{1.2}Ni_{0.8}P$ we did not see a maximum in the ZFC curve in the range of 50-350 K (inset of Figure 3.11), suggesting T_B is <50 K.

Table 3.3. Sizes, aspect ratios, T_C, and T_B of ternary $Fe_xNi_{2-x}P$ nanorods

Sample	Size (nm)	Aspect ratio	T_C (K)	T_{Cbulk} (K)	T_B (K)
$Fe_{1.8}Ni_{0.2}P$	15.21±2.95 x 8.61±1.18	1.8	250	340	185
$Fe_{1.4}Ni_{0.6}P$	18.18±3.23 x 9.93±1.08	1.8	265	230	200
$Fe_{1.2}Ni_{0.8}P$	17.02±0.61 x 9.03±1.02	1.9	125	140	<50 K
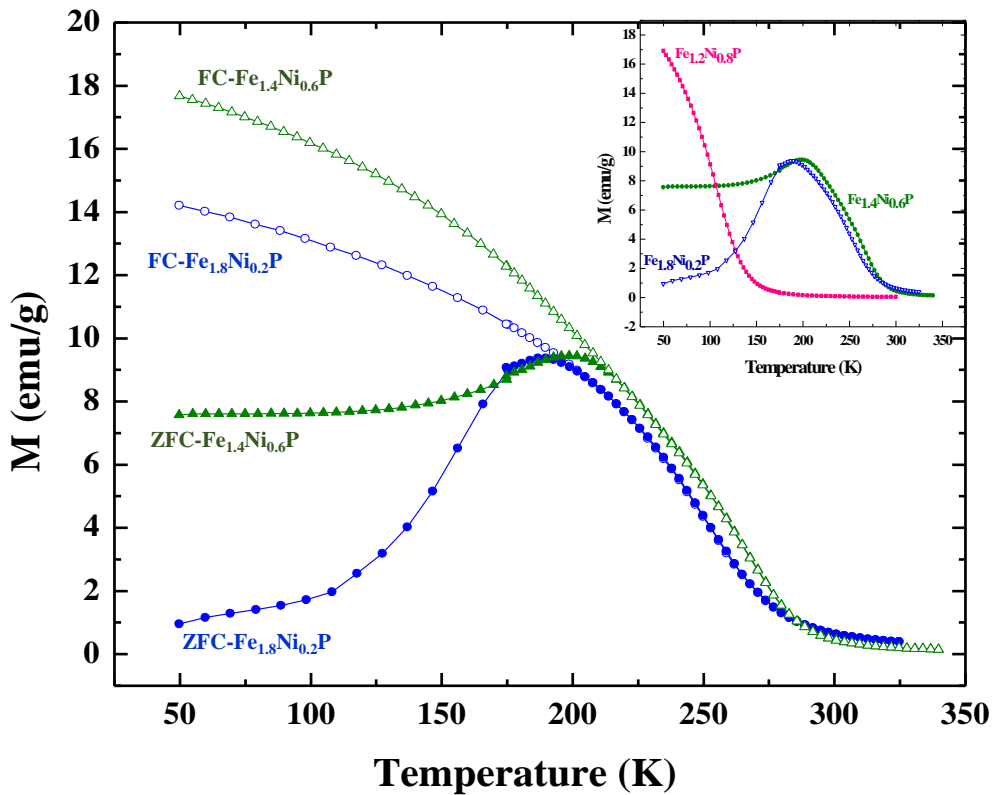
Figure 3.11 ZFC and FC plots of $Fe_{1.4}Ni_{0.6}P$ (green) and $Fe_{1.8}Ni_{0.2}P$ (blue). The inset shows the ZFC plots for $Fe_xNi_{2-x}P$ (x=1.2, 1.4, and 1.8) nanorods

To determine the Curie temperature (T_C), Arrott plots (M^2 vs. H) were acquired in the dissertation research (Figure 3.12). Composition-dependent T_C was observed for the ternary $Fe_xNi_{2-x}P$ nanoparticles (Table 3.3). The highest T_C was observed for $Fe_{1.4}Ni_{0.6}P$ (265 K). A drastic decrease in T_C was observed for $Fe_{1.2}Ni_{0.8}P$ (125 K) due to the increased Ni doping (40%). Mössbauer spectroscopy studies of these nanocrystals showed that ~55% of Fe occupies Fe(II) site when x>1.0. Therefore the effects from preferential ordering of Fe in the crystal structure on the total magnetic moment is similar for all three compositions. As indicated previously, the bulk $Fe_xNi_{2-x}P$ system also shows composition-dependent T_C. Specially, in the

range $2 > x > 1.3$, the reordered T_C is greater than that for Fe_2P (217 K) with a maximum of 342

K achieved for $Fe_{1.84}Ni_{0.16}P$ (8% Ni doping).[24]
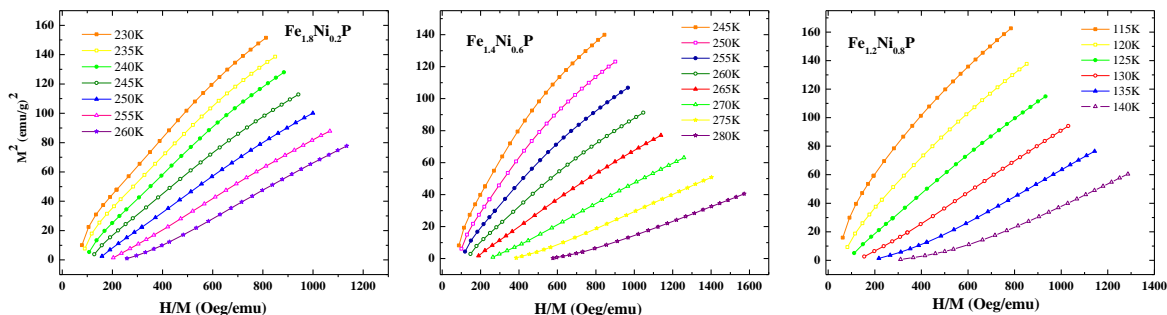
Figure 3.12 Arrott plots for $Fe_xNi_{2-x}P$ (x=1.2, 1.4, and 1.8) nanorods

The field dependent (*H*) magnetization (*M*) of ternary nanocrystals showed that all

compositions have hysteresis at low T (50 K) and similar coercivities (~30-35 emu/g). As the Ni

incorporation increases, the hysteresis loops become smaller and coercivity decreases (Figure

3.13). All show an asymmetry in the hysteresis, a thinning of the loop, near zero applied field,

consistent with some degree of metamagnetism. A similar trend was reported for FeNi bimetallic

phosphides by Hyeon and co-workers for x=1.8, 1.6, and 1.5.[58] The fact that x=1.2 demonstrates

hysteresis at 50 K suggests that T_B>50 K, despite the absence of a knee in the M vs. T plot. The

highest per gram saturation magnetization, T_C, and well as the highest T_B were observed for

$Fe_{1.4}Ni_{0.6}P$ phase. This is unexpected based on the trends in bulk ternary phases, where T_C is

maximum for x=1.84, and may suggest that limiting the size is also effecting the spin alignment

in these phases.
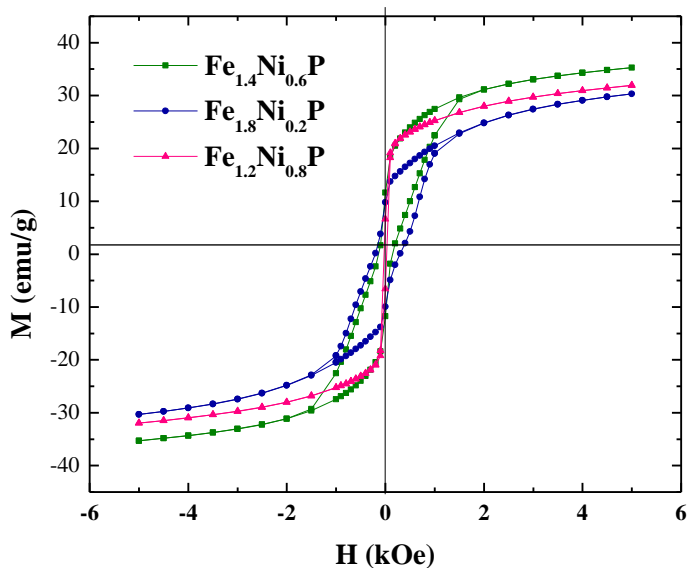
Figure 3.13 Magnetization (*M*) of ternary $Fe_xNi_{2-x}P$ nanorods as a function of applied field (*H*) at 50 K

3.4 Conclusions

A solution phase synthetic method for $Fe_xNi_{2-x}P$ (0 < x < 2) was developed. Ternary $Fe_xNi_{2-x}P$ nanoparticles crystallized in the hexagonal Fe_2P-type structure and showed a composition-dependent ordering of the metal atoms in the crystal structure, as well as a composition-dependent morphology.

The substitution of Ni into Fe_2P produced an increase in T_C, which reached a maximum of 265 K at x=1.4, decreasing rapidly with large x. Intriguingly, T_C for our ternary $Fe_xNi_{2-x}P$ nanocrystals are lower than the reported values of the bulk composition and do not follow the expected trend. However, we did establish augmentation of T_C from 217 K (Fe_2P) to 265 K ($Fe_{1.4}Ni_{0.6}P$).

CHAPTER 4

HYDRODESULFURIZATION ACTIVITY OF SILICA ENCAPSULATED $FE_xNI_{2-x}P$

NANOCRYSTALS

4.1 Introduction

$Fe_xNi_{2-x}P/SiO_2$ prepared by the TPR method has shown composition-dependent catalytic activity for HDS of dibenzothiophene (DBT) and 4, 6-dimethyldibenzothiophene (4, 6-DMDBT) with $Fe_{0.03}Ni_{1.97}P/SiO_2$ showing a 40% enhancement in DBT HDS activity relative to an optimized Ni_2P catalyst.[55, 73] Since the TPR method does not allow for control of particle size, the composition and size-dependent activities of these ternary nanoparticles have not been studied systematically. Recently, DBT HDS catalytic activity of Ni_2P nanoparticles prepared by solution-phase arrested-precipitation method was reported.[115] In this study, pre-formed narrow polydispersity Ni_2P particles were encapsulated in mesoporous silica to prevent sintering during the catalytic process. Use of pre-formed nanoparticles allows control of the particle properties on the atomic scale. As described Chapter 3, we were able to develop a synthetic method which allows for the preparation of ternary $Fe_xNi_{2-x}P$ phases as well-formed nanoparticles with control of size, shape, and composition. In this chapter we present preliminary DBT HDS catalytic data for silica-encapsulated $Fe_xNi_{2-x}P$ (x=0.03, 0.1, 0.2, and 0.3) nanoparticles.

I performed the synthesis and characterization of $Fe_xNi_{2-x}P@mSiO_2$ nanoparticles and HDS catalytic data were collected by the Bussell group in the Department of Chemistry at Western Washington University.

4.2 Experimental

All the chemicals used in this chapter are listed in Chapter 2.1.

4.2.1 Synthesis of $Fe_xNi_{2-x}P$ Particles

A detailed description of the synthesis of $Fe_xNi_{2-x}P$ particles is given in Chapter 3.2.1.

4.2.2 Synthesis of $Fe_xNi_{2-x}P@mSiO_2$

Encapsulation of $Fe_xNi_{2-x}P$ in mesoporous silica was carried out following a previously reported method, and is summarized in Scheme 4.1.[115] As-prepared $Fe_xNi_{2-x}P$ nanoparticles (135 mg dry weight) were dispersed in 5 mL of $CHCl_3$ by sonicating for 30-60 min. This dispersion was added to 20 mL of a 0.1 M CTAB solution drop-wise at room temperature under vigorous stirring. The reaction mixture was heated at 75 °C until the solution becomes clear (after evaporation of $CHCl_3$ and the organic to aqueous phase transfer is complete). The resultant nanoparticle solution was diluted with 130 mL of nanopure water. The solution was heated to 50 °C and 3 mL of 1 M NaOH was added followed by drop-wise addition of 4.5 mL of tetraethylorthosilicate (TEOS). Base-catalyzed silica polymerization initiated after 5 min and the solution was kept at 50 °C for another 30 min under vigorous stirring to complete the polymerization. The silica encapsulated nanoparticles were isolated by centrifugation and washed with nanopure water and methanol (three times with each) to remove remaining NaOH and the by-products of silica polymerization. The isolated silica-encapsulated $Fe_xNi_{2-x}P$ nanoparticles were dried under active vacuum overnight and calcined at 420 °C for 2-3 h to remove moisture and CTAB. The calcined sample was reduced in a flow furnace with a 5% H_2/Ar gas mixture in the presence of triphenylphosphine (PPh_3P) at 420 °C for 2 h to convert any oxides formed during calcination into phosphides.

Scheme 4.1 Silica encapsulation of $Fe_{2-x}Ni_xP$ nanoparticles
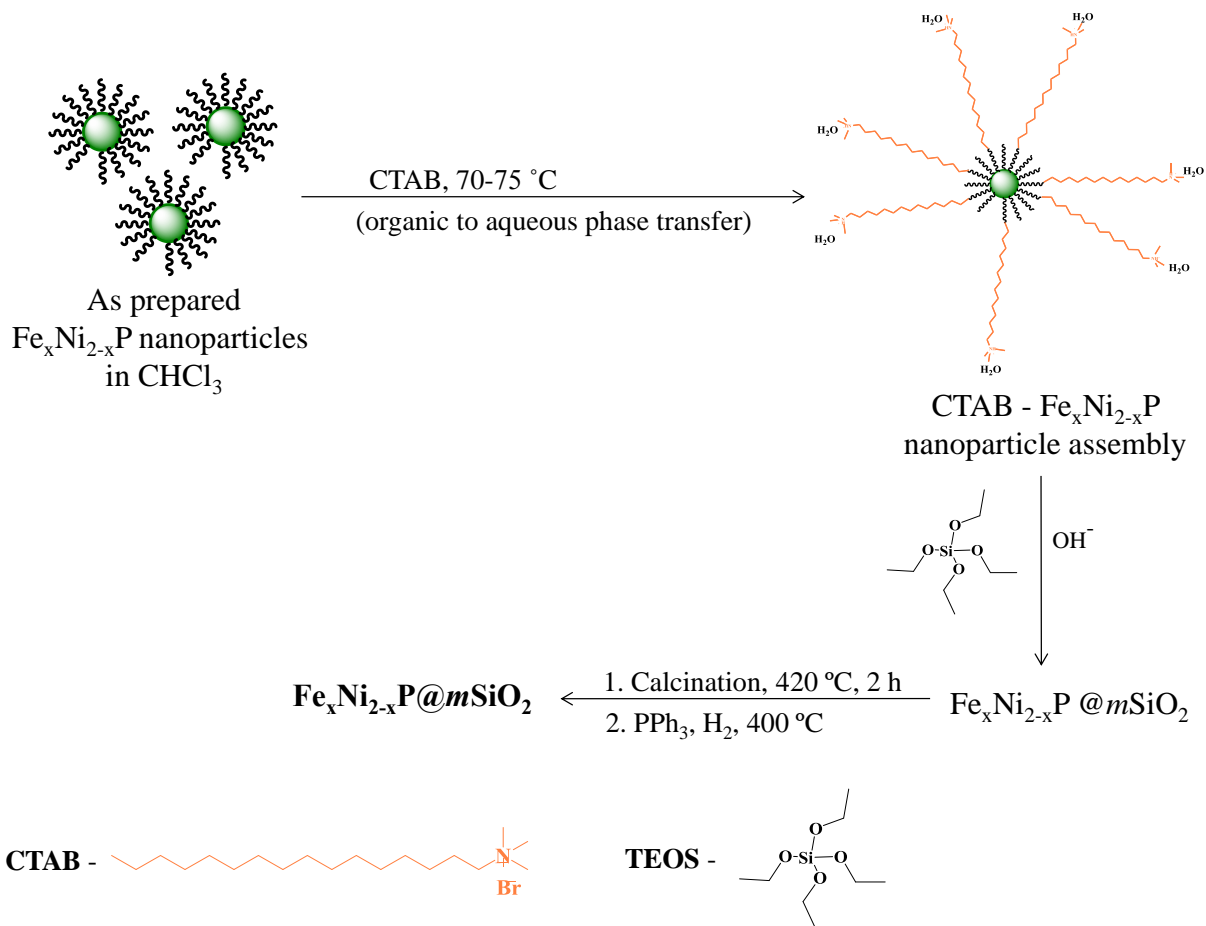
4.2.3 Dibenzothiophene (DBT) Hydrodesulfurization (HDS) Catalytic Measurements

A fixed-bed flow reactor operating at a total pressure of 3.0 MPa and temperature range of 498-537 K (225-400 °C) was used to carry out HDS catalytic measurements. A decalin solution containing dibenzothiophene (3000 ppm) and dodecane (500 ppm, internal standard for gas chromatography) was injected into a 100 mL/min flow of hydrogen and vaporized before entering the reactor. The liquid feed rate was 5 mL/h. Approximately 0.15 g of the catalyst is used. The catalyst temperature was increased by 25 K increments in 12 h intervals and the samples of the reactor effluent were analyzed using an offline gas chromatograph.[55]

4.3 Results and Discussion

4.3.1 Synthesis and Characterization of $Fe_xNi_{2-x}P@mSiO_2$

Previous studies on DBT HDS of discrete Ni_2P nanoparticles dispersed on a silica support (Cab-O-Sil) using the incipient wetness method resulted in sintering of nanoparticles under catalytic conditions due to weak interactions between the catalyst and the support.[115] The encapsulation of Ni_2P particles in mesoporous silica minimized sintering and dramatically improved the catalytic activity. In this dissertation study, $Fe_xNi_{2-x}P$ was encapsulated in mesoporous silica following a similar method to that used for Ni_2P to produce $Fe_xNi_{2-x}P@mSiO_2$. After silica encapsulation, the particles were characterized using PXRD (particle size and phase), TEM (morphology), nitrogen physisorption (surface area and pore size distribution), and ICP-MS (composition and catalyst wt%).

The PXRD patterns of as-prepared $Fe_xNi_{2-x}P@mSiO_2$ nanoparticles (x= 0.03, 0.1, 0.2, and 0.3) are shown in Figure 4.1 along with reference patterns for Ni_2P (ICDD-PDF # 74-1385) and $Ni_{12}P_5$ (ICDD-PDF # 74-1381). $Ni_{12}P_5$ is the most common impurity phase of nickel phosphide that can form under our reaction conditions.[115] A low intensity peak around 48.9° was observed for as-prepared $Fe_{0.1}Ni_{1.9}P_{1.1}@mSiO_2$ and $Fe_{0.3}Ni_{1.7}P@mSiO_2$, attributed to the presence of this $Ni_{12}P_5$ impurity (Figure 4.1d). However other two samples appeared pure by routine PXRD standards. The average particle sizes before and after silica encapsulation were calculated by applying the Scherrer formula to the (111) reflection (Table 4.1). A slight increase in crystallite size was observed by PXRD after the encapsulation. However, the TEM micrograph analyses showed no evidence for particle sintering. TEM micrographs of $Fe_xNi_{2-x}P$ before and after silica encapsulation are shown in Figure 4.2. The particles (high contrast) remain separated and dispersed in the silica support (low contrast) even after heating under reducing conditions.
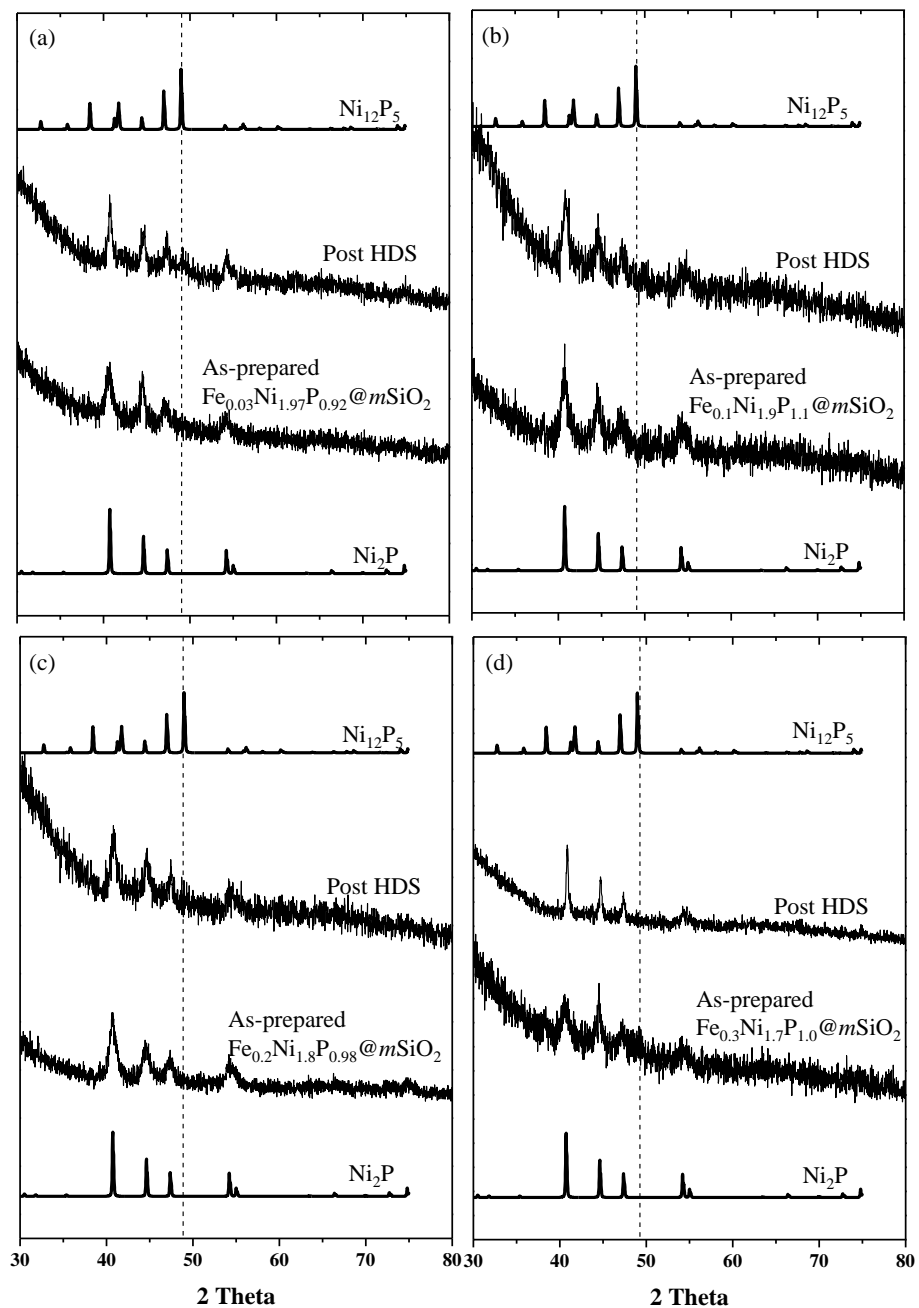
Fgure 4.1 PXRD patterns of as-prepared and post HDS $Fe_xNi_{2-x}P@mSiO_2$ nanoparticles for x =

0.03, 0.1, 0.2, and 0.3). Ni_2P and $Ni_{12}P_5$ reference patterns are provided for comparison

Table 4.1 PXRD particle sizes, BET surface areas, average BJH pore sizes, and sample loadings

of $Fe_xNi_{2-x}P@mSiO_2$ nanoparticles

Sample composition (determined by ICP-MS)	Crystalline size before silica encapsulation (nm) (from PXRD)	Crystalline size after silica encapsulation (nm) (from PXRD)	BET surface area (m^2/g)	BJH average pore diameter (nm)	Sample loading (%)
$Fe_{0.03}Ni_{1.97}P_{0.92}$ (P:M = 0.46)	9.5±0.4	10.7±1.3	932	3.2	9.3
$Fe_{0.1}Ni_{1.9}P_{1.1}$ (P:M = 0.55)	10.2±0.3	11.9±1.0	806	4.0	10.3
$Fe_{0.2}Ni_{1.8}P_{0.98}$ (P:M = 0.49)	10.7±0.3	12.2±1.0	1304	5.2	8.1
$Fe_{0.3}Ni_{1.7}P_{1.0}$ (P:M = 0.50)	10.2±0.3	12.4±1.1	787	5.0	9.5
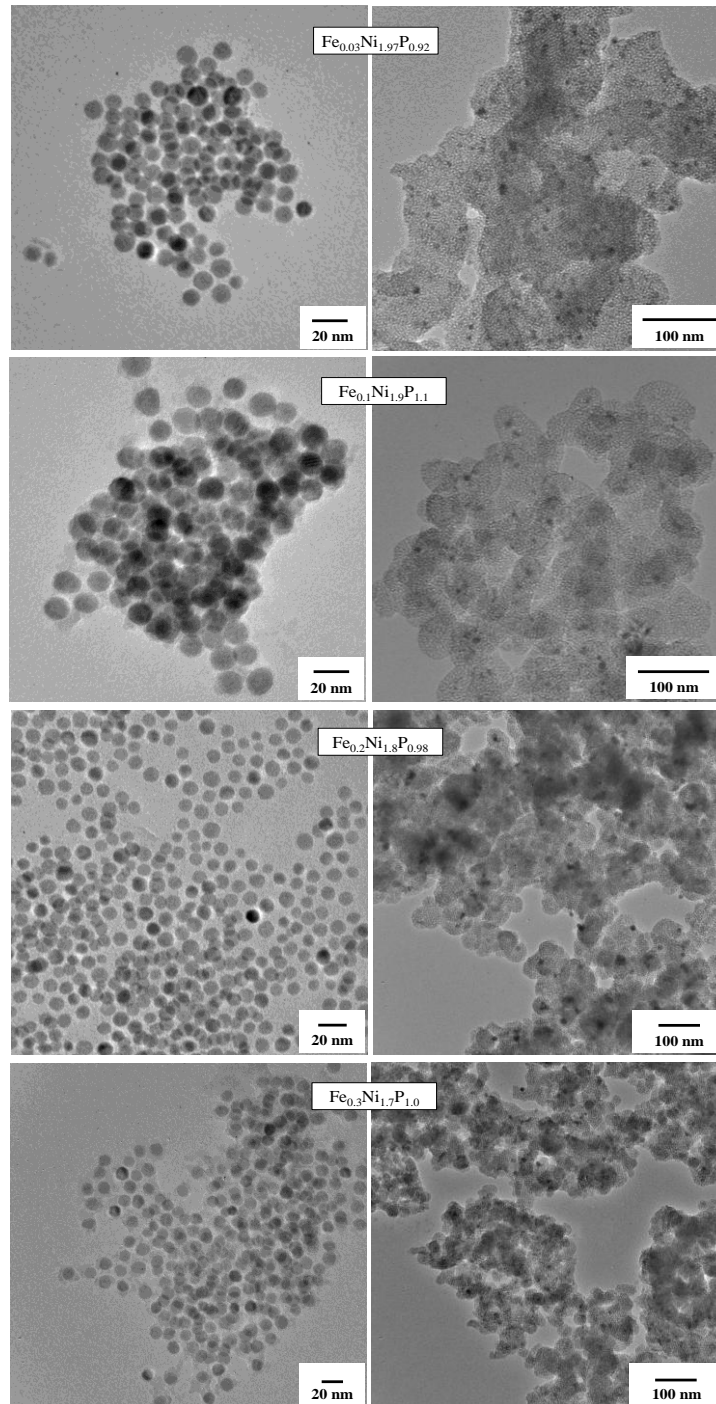
Figure 4.2 TEM micrographs of Fe$_x$Ni$_{2-x}$P@mSiO$_2$ nanoparticles before (left) and after (right) silica encapsulation

For DBT to access the active catalytic sites of the nanoparticles, the presence of a reasonable pore size (> 3 nm) in the mesoporous silica shell is important. To evaluate the pore structure and surface area of $Fe_xNi_{2-x}P@mSiO_2$ catalysts, nitrogen physisorption analyses were carried out (described in Chapter 2.3.2). The nitrogen adsorption/desorption isotherms for $Fe_xNi_{2-x}P@mSiO_2$ and the BJH pore size distribution are shown in Figure 4.3. All $Fe_xNi_{2-x}P@mSiO_2$ samples showed similar type IV isotherms, characteristic of mesoporous materials.[116] The BET surface areas were above 700 m^2/g due to the mesoporous silica support. All these materials showed pore size distributions in the range of 2-10 nm demonstrating the mesoporous nature of the silica shell (Figure 4.3). The BJH average pore sizes were in the range 3-5 nm. Even though 10% sample loadings were targeted, the actual loading varied between 8-10% (as determined by ICP-MS) and this can be attributed to incomplete silica polymerization.
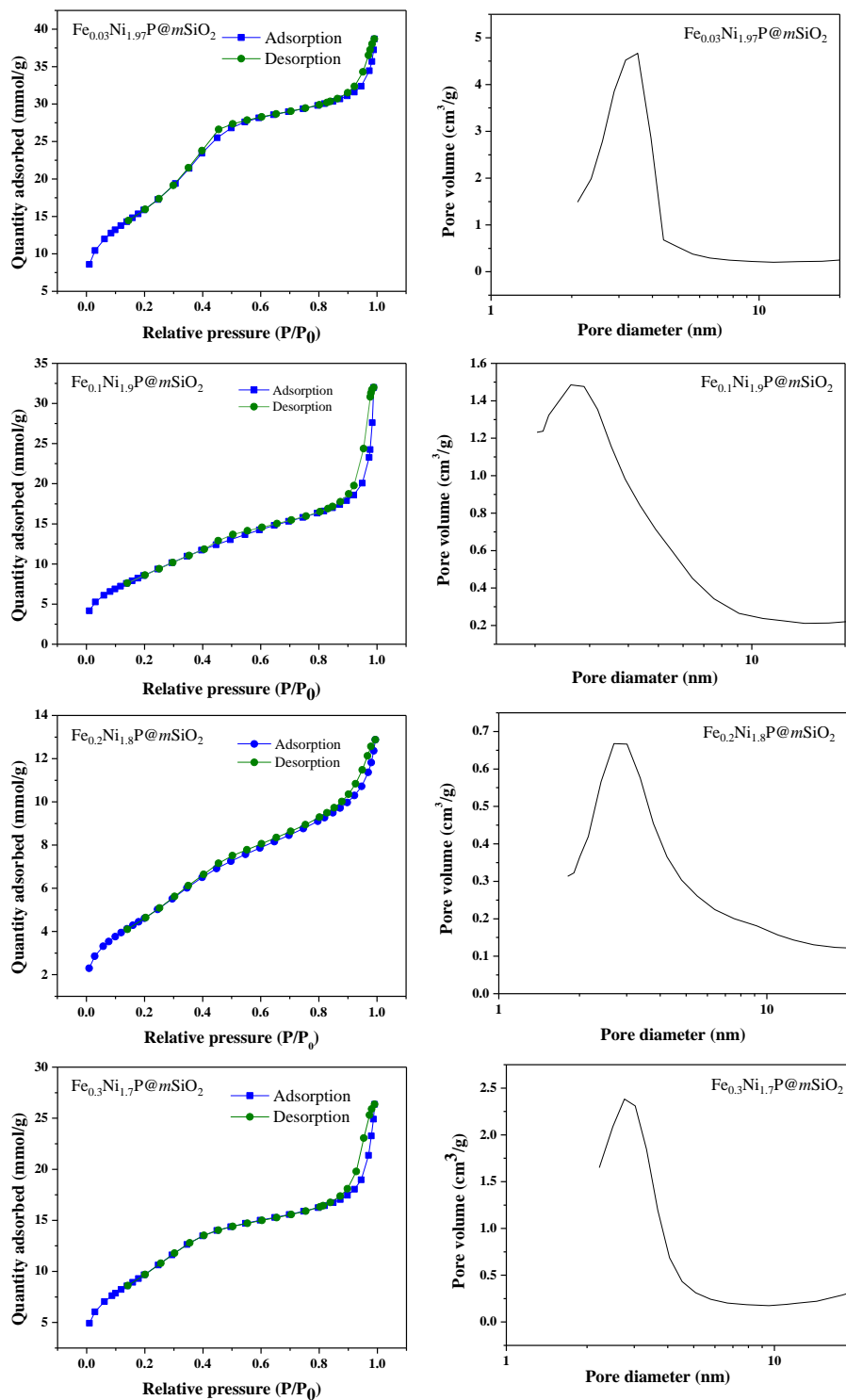
Figure 4.3 Nitrogen adsorption/desorption isotherms (left) and BJH pore size distributions (right) of $Fe_xNi_{2-x}P@mSiO_2$ (x= 0.03, 0.1, 0.2, and 0.3)

4.3.2 Dibenzothiophene (DBT) HDS Catalytic Activity of $Fe_xNi_{2-x}P@mSiO_2$ Nanoparticles

Previous studies on dibenzothiophene (DBT) and 4, 6-dimethyldibenzothiphene (4, 6-DMDBT) HDS catalysis with $Fe_xNi_{2-x}P$ revealed a decrease in activity when x>0.03.[55, 73] However, a catalyst having a nominal composition $Fe_{0.03}Ni_{1.97}P/SiO_2$ was measured to have 40% more DBT HDS activity than the optimized nickel phosphide catalyst at 643 K. The higher activity of $Fe_{0.03}Ni_{1.97}P/SiO_2$ is correlated to the preferential Ni occupation of M(2) sites and surface termination by Ni(2) sites. The increased active site densities resulted in improved catalytic activity. Mössbauer studies of our unsupported $Fe_xNi_{2-x}P$ (Chapter 3.3.2) revealed that at very Ni-rich end, Fe preferentially occupies M(1) sites and M(2) sites occupied preferentially by Ni (Figure 3.3). Therefore, a similar trend in DBT HDS activities can be expected for the $Fe_xNi_{2-x}P@mSiO_2$ catalysts.

Based on previous studies, four catalysts of $Fe_xNi_{2-x}P@mSiO_2$, where x= 0.03, 0.1, 0.2, and 0.3 were studied.[55, 73] DBT HDS of $Fe_xNi_{2-x}P@mSiO_2$ was carried out as described in 4.2.2. The percentage conversion of DBT by HDS as a function of temperature for $Fe_xNi_{2-x}P@mSiO_2$, (x= 0.03, 0.1, 0.2, and 0.3) is shown in Figure 4.4. Composition-dependent catalytic activity of $Fe_xNi_{2-x}P@mSiO_2$ was observed. As the amount of Fe increases, the DBT HDS decreased as expected. At 623 K $Fe_{0.1}Ni_{1.9}P@mSiO_2$ showed a similar catalytic activity as $Ni_2P@mSiO_2$ whereas other compositions showed lower activities. Unfortunately we did not observe an increase for activity in the $Fe_{0.03}Ni_{1.97}P_{0.98}@mSiO_2$ phase, in contrast to TPR-prepared samples. In fact, this phase showed an anomalously low activity relative to all other samples measured.

PXRD analyses after HDS did show the presence of impurity $Ni_{12}P_5$ phase for $Fe_{0.03}Ni_{1.97}P_{0.92}@mSiO_2$, $Fe_{0.1}Ni_{1.8}P_{0.98}@mSiO_2$, and $Fe_{0.3}Ni_{1.7}P_{1.0}@mSiO_2$ where $Ni_{12}P_5$ was observed for $Fe_{0.1}Ni_{1.9}P_{1.1}@mSiO_2$ and $Fe_{0.3}Ni_{1.7}P_{1.0}@mSiO_2$ samples even before HDS analysis

(Figure 4.1). $Ni_{12}P_5$ is known to be a poor HDS catalyst. The presence of $Ni_{12}P_5$ phase can be a major contributor for lower HDS activity of $Fe_xNi_{2-x}P@mSiO_2$ (x=0.03, 0.1, and 0.3) catalyst samples. Moreover, PXRD analyses of spent catalyst showed sharp peaks for $Fe_{0.03}Ni_{1.97}P_{0.92}@mSiO_2$ and $Fe_{0.3}Ni_{1.7}P_{1.0}@mSiO_2$ suggesting that significant particle sintering has taken place during DBT HDS catalysis.

HDS analysis of $Fe_{0.03}Ni_{1.97}P_y/SiO_2$ prepared via the TPR method has shown that the catalytic activity depends on the phosphorous amount for the same x and the catalytic activities were in the order of $Fe_{0.03}Ni_{1.97}P_{1.2}/SiO_2$ < $Fe_{0.03}Ni_{1.97}P_{1.8}/SiO_2$ < $Fe_{0.03}Ni_{1.97}P_{2.0}/SiO_2$. The presence of excess phosphorous has enhanced the resistance towards sulfur poisoning leading to higher activity.[53] In this study the most active catalyst, $Fe_{0.1}Ni_{1.9}P_{1.1}$ was the most P-rich and $Fe_{0.03}Ni_{1.97}P_{0.92}$ was slightly P-deficient, relative to the other compositions (Table 1.1). However, P:M ratio remained in the range of 0.46-0.55. Therefore the effects from P amount is not significant as in the case of the TPR-prepared $Fe_{0.03}Ni_{1.97}P_y/SiO_2$ (P:M=0.6-1.0).

There was some inconsistency in sample loading, with $Fe_{0.1}Ni_{1.9}P_{1.1}@mSiO_2$ having the highest sample loading (10.3%) and $Fe_{0.2}Ni_{1.8}P_{0.98}@mSiO_2$ had the lowest sample loading (8.1%).

The above mentioned factors including composition (Fe and P contents), $Ni_{12}P_5$ impurity phase, particle sintering, and sample loading can contribute towards the lower HDS activity of $Fe_xNi_{2-x}P@mSiO_2$ samples. The lower activities of $Fe_{0.03}Ni_{1.97}P_{0.92}@mSiO_2$ and $Fe_{0.3}Ni_{1.7}P_{1.0}@mSiO_2$ samples can be attributed to the presence of $Ni_{12}P_5$ impurity phase, particle sintering, and higher Fe content of $Fe_{0.3}Ni_{1.7}P_{1.0}@mSiO_2$ sample. The lower sample loading and higher Fe content may be the reasons for lower activity in $Fe_{0.2}Ni_{1.8}P_{0.98}@mSiO_2$ catalyst. The presence of $Ni_{12}P_5$ may have lowered the HDS activity of $Fe_{0.1}Ni_{1.9}P_{1.1}@mSiO_2$.
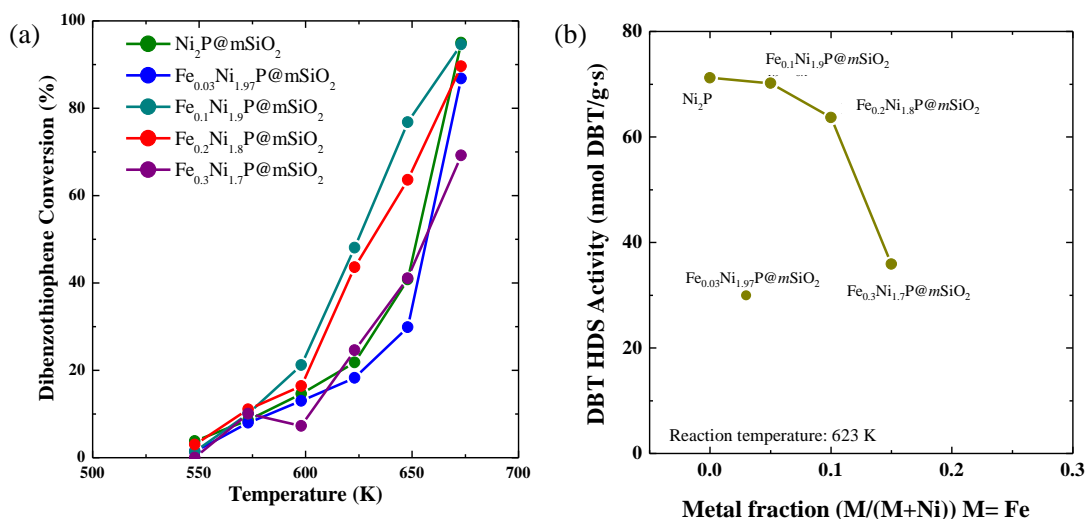
Figure 4.4 (a) Percentage HDS conversion of DBT vs. reaction temperature and (b) DBT HDS activity at 623 K as a function of Fe fraction of $Fe_xNi_{2-x}P@mSiO_2$

The HDS reaction pathway selectivity of these phases was studied by analyzing the products of catalytic conversion of DBT using gas chromatography. Figure 4.5a shows the percentage product selectivity at 598 K for $Fe_xNi_{2-x}P@mSiO_2$ (x=0.1, 0.2, and 0.3), $Ni_2P@mSiO_2$ and Ni_2P/SiO_2 prepared via the TPR method. Ni_2P/SiO_2 prepared by the TPR method only

showed 60% product selectivity to biphenyl (BP), the direct desulfurization (DDS) pathway product for DBT, whereas $Ni_2P@mSiO_2$ showed a significantly larger BP product selectivity (~85%). As iron is incorporated, the BP product selectivity increased relative to HYD (Figure 4.5b). In the study of Bussell and co-workers $Fe_{0.03}Ni_{1.97}P/SiO_2$ exhibited 68% selectivity towards DDS of DBT, an increase in selectivity towards HYD pathway relative to optimized $Ni_{2.00}P_{1.60}/SiO_2$ catalyst.[55] This increase is ascribed to higher site densities and increased sulfur resistance of bimetallic phosphide catalysts due to higher Ni(2) surface site concentration, which are purported to be responsible for the HYD pathway. Although we see a similar trend in site occupancy of Ni in $Fe_xNi_{2-x}P$, a decrease in the HYD pathway was observed. The reduction in activity may be due to the decreased tendency toward HYD as Fe is incorporated. This decreased tendency toward the HYD pathway may be the reason for the overall decrease in activity with increasing Fe, as HYD sites may be being lost.
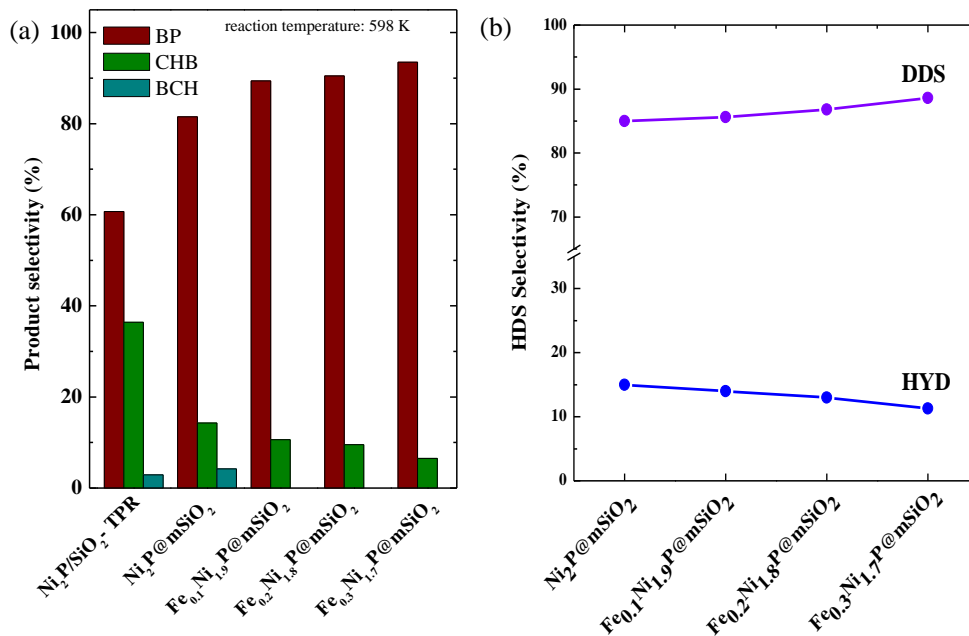
Figure 4.5 Percentage product selectivity (left) and percentage HDS activity of $Fe_xNi_{2-x}P@mSiO_2$ nanoparticles. (Note, product selectivity data for $Fe_{0.03}Ni_{1.97}P_{0.92}@mSiO_2$ are not presented due to the low activity of this catalyst)

4.4 Conclusions

DBT HDS activity of $Fe_xNi_{2-x}P@mSiO_2$ (x=0.03, 0.1, 0.2, and 0.3) showed composition dependent catalytic activity. When x=0.1 the highest activity was observed and higher values of x showed a systematic decrease in activity consistent with prior work on TPR-prepared catalysts. $Fe_{0.03}Ni_{1.97}P/SiO_2$ composition is reported to have a higher catalytic activity than optimized nickel phosphide when prepared by the TPR method. However, in the study of mesoporous silica encapsulated $Fe_xNi_{2-x}P$ the same composition showed a lower activity than $Ni_2P@mSiO_2$ and does not follow the trend of other samples studied. The reasons for this anomalous behavior is due to the formation of $Ni_{12}P_5P$ and particle sintering during HDS catalysis. The overall decrease

in catalytic activity in $Fe_xNi_{2-x}P@mSiO_2$ (x=0.03, 0.1, 0.2, and 0.3) may be due to decreased selectivity towards HYD pathway. To quantitatively and qualitatively interpret HDS activities of the samples, surface composition and active site densities need to be examined using X-ray photoelectron spectroscopy and CO chemisorption measurements respectively.

With the exception of $Fe_{0.03}Ni_{1.97}P_{0.92}@mSiO_2$ the $Fe_xNi_{2-x}P@mSiO_2$ mimicked the $Fe_xNi_{2-x}P/SiO_2$ catalysts prepared by TPR. This study lays the foundation for studying the size dependent HDS of $Fe_xNi_{2-x}P@mSiO_2$. To address the problems associated with original samples and further study 4,6-dimethyldibenzothiophene HDS I have prepared a new set of $Fe_xNi_{2-x}P@mSiO_2$ (x=0.03, 0.15, 0.27, 0.46, 0.63, and 0.76) samples. The characterization data of these samples are reported in Appendix A.

CHAPTER 5

FORMATION OF GELS AND AEROGELS OF PHOSPHIDES[3]

5.1 Introduction

Aerogels are an important class of nanostructured materials consisting of nanoscale building blocks that are interconnected, leading to a porous network structure. Because of the unique physical nature of aerogels, they have a wide range of applications as catalysts, adsorbents, and thermal insulators. Aerogel compositions were traditionally focused on oxides, especially SiO_2, but expanded to embrace carbon in the 1990's.[91, 92, 117-120] In 2004, metal chalcogenide (MQ) aerogels were reported for the first time via supercritical drying of gels produced by a nanoparticle assembly route in which discrete nanoparticles were capped with a thiolate ligand, followed by controlled oxidation of the ligand to form a gel.[95] This approach has been extended to a wide range of compositions, including CdS, PbS, ZnS, CdSe, CdTe, Bi_2Te_3, and PbTe.[85, 95, 97, 102] These quantum dot aerogels are linked together by interparticle Q_n^{2-} ($n \geq 2$) bridging units arising from surface oxidation of Q^{2-} species. These are robust to cation exchange, a fact that has been exploited to make new materials (e.g. Ag_2Se) and remove heavy metals (Pb^{2+} and Hg^{2+}) from aqueous systems, but are susceptible to disaggregation by chemical reduction.[100, 101, 121] These metal chalcogenide quantum dot aerogels comprise the characteristic optical properties of their quantum dot particle components, translating the nano-scopic properties into macroscopic "handle-able" materials.

The successful application of the nanoparticle condensation strategy to such a diverse range of chalcogenide ions led us to consider whether this approach would be similarly applicable to group 15 elements—phosphides. In contrast to metal chalcogenide gelation, there is

---

[3] Portions of the text in this chapter were reprinted or adapted with permission from: *ACS Nano*, 2013, 7, 1163-1170 and *Chem. Mater.* 2014, 26, 6251-6256

no precedence in the literature for metal phosphide gelation. In this chapter we demonstrate the applicability of the sol-gel nanoparticle assembly method that has proven to be robust for a range of metal chalcogenides, to metal phosphides; specifically, InP and Ni$_2$P.

The content in this chapter is already published.[122, 123] Preliminary studies were performed by Keerthi Senevirathne and are reported in his dissertation.

5.2 Experimental

The chemicals used this chapter are listed in Chapter 2, section 2.1.

5.2.1 Synthesis of InP Nanoparticles, Gels, and Aerogel

Synthesis of 3.5 nm Particles

A mixture of InCl$_3$ (1.36 mmol) and TOPO (5.0 g) was degassed at 110 °C for 20 min and heated at 260 °C for 30-60 min. The phosphorous precursor, tris(trimethylsilyl)phosphine (1.36 mmol), was diluted in 1-octadecene (7 mL) and injected into the pre-heated In precursor solution mixture at 260 °C. The reaction mixture was maintained at 260 °C for 24 h. Nanoparticles were isolated at 60 °C by precipitation with absolute ethanol followed by centrifugation, and washed twice with a CHCl$_3$/ethanol solvent mixture.

Synthesis of 6.0 nm Particles

6.0 nm InP nanoparticles were synthesized using a continuous injection method. Briefly, tris(trimethylsilyl)phosphine (1.36 mmol) was mixed with InCl$_3$ (1.36 mmol) dissolved in TOP (7 mL) at room temperature. The reactant mixture was injected into TOPO at 260 °C at a varying rate profile using a syringe pump. First, 2 mL of solution was injected at a rate of 2 mL/min and the reaction allowed to proceed for 1.5 h, then a 1 mL aliquot was injected at a rate of 1 mL/min. Thereafter, 0.5 mL was injected every 30 min at a rate of 0.5 mL/min. The rest of the reaction procedure is as described for the single injection method.

Thiolate Exchange of InP Nanoparticles

The TOPO ligands on the InP nanoparticles' surface were subsequently exchanged with 11-mercaptoundecanoic acid (MUA). The amount of MUA used was determined relative to the mole amount of metal precursor used in the nanoparticle synthesis (the targeted metal precursor: MUA ratio was 1:3). The requisite amount of MUA was dissolved in 10-15 mL of absolute ethanol and the pH was adjusted to 10-11 by the addition of tetramethylammonium hydroxide pentahydrate (TMAH). Nanoparticles were dispersed in this solution and stirred for 24 hours at room temperature under periodic argon flushes. Ethylacetate was used to wash the MUA capped nanoparticles and remove excess MUA and TOPO. Thiolate capped nanoparticles were dispersed in 2-4 mL of absolute ethanol for gelation.

InP Gel Formation

Wet gels of InP were formed through oxidative sol-gel assembly using 3% H_2O_2 as the oxidant. MUA-capped nanoparticles were dispersed in 4 mL of absolute ethanol by sonication. 0.1-0.5 mL of 3% H_2O_2 was added with agitation and then allowed to sit on the bench for gelation. The gel formation started within 30 min and gels were aged for 2 weeks before aerogel formation.

InP Aerogel Formation

The wet gel solvent was exchanged with acetone (3 times) without disturbing the gel structure. The sample vial was placed inside the critical point dryer at 19 °C. The chamber was filled with liquid CO_2 and drained after 1 hour. This process was repeated 3 times over a time period of 4 hours. For supercritical drying, the chamber was half filled with CO_2 at 19 °C and the temperature was raised to 39 °C. With the increase of the temperature, the pressure inside the

chamber increased (1300-1500 psi). The gel was kept at that temperature and pressure for 1 hour and then the pressure was released to dry the gel.

5.2.2 Synthesis of Ni_2P Nanoparticles, Gels and Aerogels

Synthesis of Ni_2P Nanoparticles

For the synthesis of Ni_2P nanoparticles, a method developed by Muthuswamy et. al. was employed with minor variations.[49] Briefly, a mixture of $Ni(acac)_2$ (0.5140 g, 2 mmol), TOP (5 mL, 11.2 mmol), octyl ether (10 mL), and oleylamine (2 mL) was heated at 230 °C for 30 min, followed by raising the temperature to 350 °C and maintaining this temperature for 3 h. Nanocrystals were isolated as described for InP (Chapter 5.2.1).

Thiolate Exchange of Ni_2P Nanoparticles

In the case of Ni_2P, exchange was performed with three ligands, MUA, 4-fluorothiophenol, and 1-dodecanethiol. For all cases, the thiol: metal molar ratio targeted was 4:1 for thiol exchange. The amount of nickel was estimated using the formula weight of Ni_2P and disregarding contributions of surface ligands to the mass of product. MUA ligand exchange was carried out as described for InP. In the case of 4-fluorothiophenol, Ni_2P nanoparticles were dispersed in hexane and 4-fluorothiophenol and tetraethylamine (TEA, thiol: TEA molar ratio=1) were added. The reaction mixture was stirred overnight and the precipitate formed was washed with toluene. When 1-dodecanethiol was used as the thiol, no base was used in the exchange. Nanocrystals were dispersed in diethyl ether (8-10 mL) and 1-dodecanethiol was added. The reaction was stirred overnight and washed with ethanol.

Ni_2P Gel Formation

Ni_2P wet gels were formed using two oxidants, 3% aqueous H_2O_2 and tetranitromethane (TNM). The thiolate-capped nanoparticles (MUA and 4-fluorothiophenol, ca. 135 mg) were

dispersed in absolute ethanol (ca. 5 mL) in a polyethylene vial under ambient conditions. The oxidant (0.1 mL) was added and the solution was allowed to sit on the bench top or in the glove box until gelation occurred. For 1-dodecanethiolate-capped nanoparticle gelation, the procedure was the same except nanoparticles were dispersed in a hexane/acetone solvent mixture, the 3% H_2O_2 solution was prepared by diluting 30% H_2O_2 (aq) with acetone and the 3% TNM was prepared in acetone. In all cases, the gelation started after ca. 30-60 minutes and gels were subsequently aged for 5-6 days.

Metal-assisted Ni$_2$P Gel Formation

100 mL of an ethanolic solution of Ni^{2+} (0.5×10^{-3} M) was prepared by dissolving $NiCl_2$ in absolute ethanol. Depending on the targeted Ni^{2+}:Ni$_2$P ratio, Ni^{2+} was added to MUA/4-fluorothiophenolate-capped nanoparticles dispersed in 5 mL of absolute ethanol and 1-dodecanethiolate-capped nanoparticles dispersed in a hexane/acetone solvent mixture. Several Ni^{2+}:N$_2$P molar ratios (1:10, 1:5, 1:2, and 1:1) were targeted (computed based on the formula weight of Ni$_2$P and neglecting that of surface ligands on the particles).

Ni$_2$P Aerogel Formation

Ni$_2$P aerogels were formed using the same procedure as InP aerogel formation (Chapter 5.2.1).

5.2.3 Dispersion Studies of InP Aerogels

MUA Dispersion

A solution of MUA was prepared by dissolving 1 mmol (0.202 g) of MUA in 5 mL of absolute ethanol and the pH was adjested to 12 by adding TMAH. This was added to InP wet gel (0.250 mmol) and left over night.

NaBH₄ Dispersion

1 mmol (0.04 g) of NaBH₄ and 0.125 mmol of InP aerogel were taken together into a Schlenk flask under Ar atmosphere. Then 10 mL of ethanol purged with Ar and cooled (4 °C) in an ice bath was added to the previous reactant mixture. This was stirred at 4 °C in an ice bath for 6 hours. A control reaction was carried out without adding NaBH₄.

5.3 Results and Discussion

5.3.1 InP Nanoparticles, Gels, and Aerogels

A method employed by Heath and co-workers was applied for InP nanoparticles formation, with slight modifications. A rapid injection of a phosphorous precursor (a phosphine) into a hot coordinating solvent (trioctylphosphine oxide, TOPO), in which the indium precursor (InCl₃) is dissolved, causes a rapid nucleation of InP nanoparticles, as observed by a reaction color change from colorless to reddish brown (ca. 3-5 min). Although the relatively inexpensive $P[(CH_3)_2N]_3$ has been reported to yield InP, it did not yield any isolable product in our hands, necessitating the use of the more reactive phosphine $P[Si(CH_3)_3]_3$. The TOPO ligands on the InP nanoparticle surface were subsequently exchanged with 11-mercaptoundecanoic acid (MUA). Upon treatment with 3% H_2O_2, we observed the initiation of gel formation within approximately 30 min. Moreover, capped sols left under ambient fluorescent lighting in the lab also yielded gels, but this process is slow and takes approximately 3 weeks before gel formation becomes apparent. Presumably, in the latter case gelation is occurring by photooxidation with O_2 from air, consistent with our previous work on chalcogenide gels. The gels were aged for 10-14 days to provide the gel network more mechanical integrity, then the mother liquor was thoroughly exchanged with acetone, taking care not to disturb the gel network. Supercritical drying was employed to maintain the pore structure in the solid state, generating an aerogel.

5.3.1.1 Structure and Morphology of InP Nanoparticles and Aerogels

InP aerogels (AG) are structurally identical to the nanoparticles (NP) from which they were assembled. Structural phase identification was carried out using powder X-ray diffraction (PXRD). The PXRD patterns of InP nanoparticles (NP) prepared by multiple precursor injection synthesis is shown in Figure 5.1a. There are three distinct peaks that correlate to the expected pattern for cubic InP. The peaks are broad, consistent with formation of nanoparticles. Crystallite sizes of nanoparticles prepared by both single and multiple injection methods were calculated by applying the Scherrer formula to the (220) peak. The calculated particle sizes were 3.5 ± 0.2 nm for a single precursor injection synthesis and 6.0 ± 0.3 nm for a synthesis employing multiple injections of precursor. No change in peak breath is observed for aerogels, suggesting that the crystallite size is not changed in the oxidative gelation and drying processes.
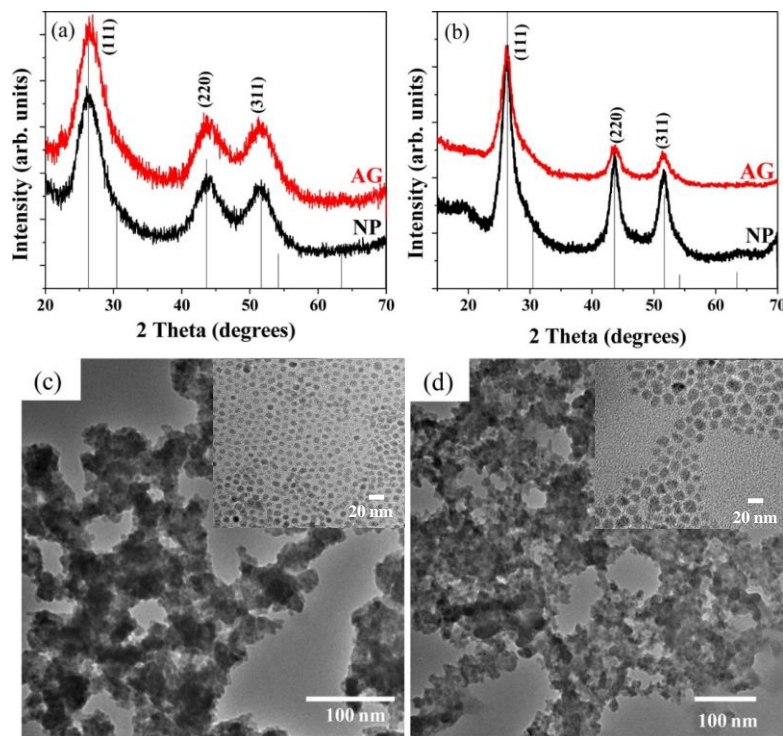
Figure 5.1 (a), (b) are PXRD patterns and (c), (d) are TEM micrograph of 3.5 and 6.0 nm NPs and AGs

Transmission electron microscopy (TEM) was used to study the morphology of InP nanoparticles and aerogels. A TEM micrograph of 3.5 and 6.0 nm InP nanoparticles are shown as insets of Figure 5.1c and d. Both sizes of nanoparticles are narrowly polydisperse and showed average sizes of 4.0 ± 0.9 and 8.0 ± 0.9 nm, slightly larger than values obtained by application of the Scherrer formula to the PXRD data (from this point forward when referring to the particle size, the sizes computed from the Scherrer formula will be used). InP aerogels display the distinctive pearl necklace morphology of colloidal aggregates, similar to base catalyzed silica gels, as shown in Figure 5.1a and d and the material has an interconnected network morphology with an extensive network of pores spanning a range of sizes.

5.3.1.2 Surface Area Measurements of InP Nanoparticles and Aerogels

In order to further probe the porous nature of the network, nitrogen adsorption-desorption isotherms were acquired. Surface areas of InP nanoparticles and aerogels were determined by application of the Brunauer-Emmett-Teller (BET) model and the pore-size distribution and average pore diameter were determined using the Barrett-Joyner-Halenda (BJH) model. The adsorption-desorption isotherms of all four samples (3.5 nm NP and AG, and 6.0 nm NP and AG), are similar in shape and represent a type IV curve, characteristic of a mesoporous (2-50 nm pore diameter) material, with a sharp upturn in the high relative pressure region due to liquid condensation in macro pores (>50 nm, Figure 5.2).[112] There was a bimodal distribution of mesopores in both AG samples (insets of Figure 5.2 b and d) with average pore sizes of 8.7 nm (AG from 3.5 nm particles) and 7.7 nm (AG from 6.0 nm particles). These pore size distributions are atypical for aerogels, where a broad range of pores extending from the micro to the upper macropore region is normally observed and usually what we see for the chalcogenide systems.

This bimodal distribution, observed consistently from sample to sample, is not evident in TEM micrographs.

InP aerogels have comparable surface areas to chalcogenide aerogels of similar mass. The surface areas of the precursor nanoparticles were very low compared to theoretical surface areas; less than 25% of the theoretical surface area was achieved (Table 5.1). However, by assembling nanoparticles into aerogels we were able to improve the accessible surface area by incorporation of an interconnected pore network. Thus, more than 60% of the theoretical surface area was achieved for aerogels (Table 5.1). As expected from our calculations, the 3.5 nm NP and AG samples showed higher surface areas and higher cumulative pore volumes compared to 6.0 nm NP and AG samples (Table 5.1).

Table 5.1. Theoretical and experimental surface areas, experimental pore sizes, and pore volumes of NPs and AGs

Sample	Theoretical surface area (m^2/g)	Experimental surface area[a] (m^2/g)	Average pore size (nm)	Cumulative pore volume (cm^3/g)
3.5 nm NP	356	82	4.8	0.12
3.5 nm AG	356	212	8.7	0.46
6.0 nm NP	208	50	7.0	0.13
6.0 nm AG	208	195	7.7	0.41

Surprisingly, nanoparticle isotherms also can be modeled by BJH as having a pore size distribution, but these are largely in the lower mesopore region (<10 nm). This bears some similarity to the first peak in the aerogel plot, but there is no corresponding broader feature at

larger pore diameters as observed for aerogels. The appearance of <10 nm pores may be attributable to filling of void spaces between packed nanoparticles.
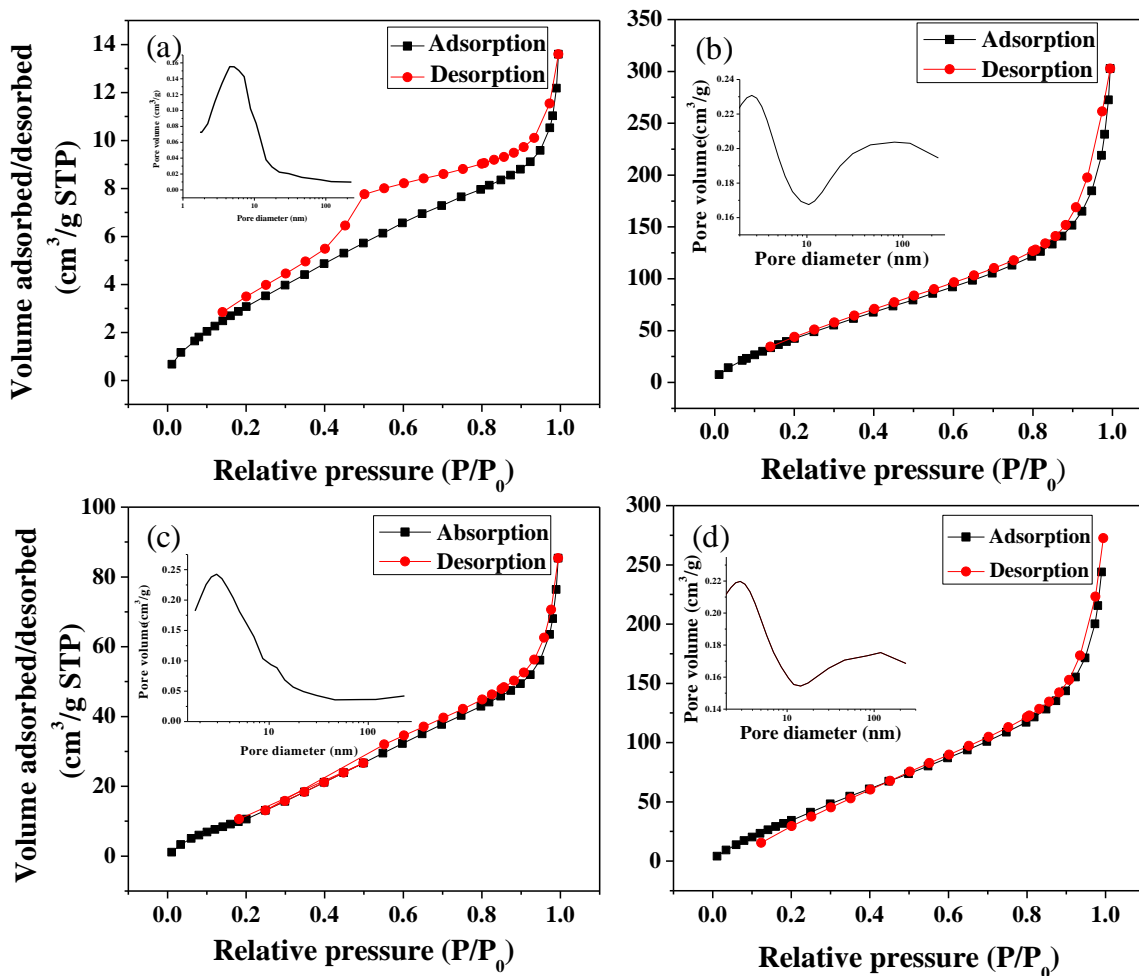
Figure 5.2 Nitrogen adsorption/desorption isotherms for (a) and (b) 3.5 nm NPs and AG and (c) and (d) 6.0 nm NPs and AG. The insets of (a), (b), (c), and (d) show the BJH pore size distributions for 3.5 nm and 6.0 nm NPs and AGs.

5.3.1.3 Gelation Mechanism

The gel network formation mechanism for thiolate (11-mercaptoundecanoic acid) capped CdSe has been reported by Brock and co-workers.[96] The gel network of CdSe nanoparticles

appears to be held together by interparticle Se-Se bonds that form due to oxidation of surface Se^{2-} species. The process of gelation can accordingly be reversed by reduction of Se–Se bonds using agents such as thiolates, leading to dispersion. This mechanism appears to extend to all metal chalcogenides (MQ) (i.e. Q–Q bonds are responsible for gel networks). If we consider a similar mechanism for metal phosphide particles, as shown in Figure 5.3, thiolates on the surface of the nanoparticles will be oxidized to form disulfides, which will leave the surface of the particles exposed to the oxidant. Subsequent solubilization of metal ions will result in a surface rich in P^{3-} species. If oxidation of P^{3-} species occurs analogously to S, Se, and Te we expect to see formation of P–P bonds, as P_2^{4-}. Such P_2^{4-} species are well established in the solid state chemistry of phosphides.[124]

Previous studies on InP nanoparticles and aerogels found that gelation has led exclusively to an increase in the band gap.[125] The absorbance onsets for 3.5 nm InP nanoparticles and the resultant aerogel are 1.7 and 2.1 eV (730 and 590 nm), respectively, and are significantly greater than the band gap of bulk InP (1.35 eV, 919 nm). The blue shift relative to the bulk value of InP suggests that both InP nanoparticles and aerogels are quantum confined. The fact that aerogels demonstrate higher band gap values than their precursor nanoparticles, indicates that gelation has resulted in a decrease in the size of the chromophore (i.e. enhanced quantum confinement), despite the fact that they are connected in a 3D linked architecture. This is in direct contrast to what is observed in metal chalcogenide gels. Brock and co-workers have reported optical band gaps for CdSe nanoparticles, wet gels, aerogels, and xerogels.[126] All of the above mentioned nanostructures had wider band gaps relative to bulk CdSe. However both aerogels and xerogels of CdSe show a distinct red shift in the band gap relative to the precursor nanoparticles, due to

delocalization through the network. This trend has been reported for many other metal chalcogenide systems as well.[96, 100]

Thus the blue shift in absorbance onset of InP upon gelation suggests a different mechanism is operable in this phosphide system. This has led us to re-evaluate our hypothesis and consider the possibility of surface etching and/or formation of a thick oxidized shell during the process of oxidation with H_2O_2. Formation of a phosphate/phosphite shell, if it occurred by sacrifice of part of the InP core, would result in an increase in quantum confinement relative to the precursor nanoparticles (Figure 5.3b). We note that, in contrast to phosphide gels, there is considerable evidence in the literature for phosphate gels. Thus, sol–gel techniques are used to make mesoporous, high surface area amorphous $AlPO_4$–SiO_2 and other phosphate gels and glasses.[127, 128]

If the hypothesis of oxygenation (Figure 5.3b) is valid, we expect that use of a non-oxygen transferring oxidizing agent, such as tetranitromethane (TNM), would not lead to gelation.[129] Moreover, if phosphates or phosphites are forming, the surface phosphorous will be transformed from a negative to a positive oxidation state, and this change in oxidation state should be evident by X-ray photoelectron spectroscopy (XPS).

Accordingly, we attempted to prepare InP gels using TNM, under air free conditions, but no gelation was observed. This is in contrast to chalcogenide gelation, which proceeds rapidly with TNM. Surface oxidation of aerogels was confirmed by X-ray photoelectron spectroscopy (XPS). Peaks corresponding to In, P, C, and O are all present in both nanoparticle and aerogel samples (Figure 5.4a). High resolution spectra were also taken for the P 2p regions of nanoparticles and aerogels. The P 2p spectra for nanoparticles (TOPO capped) and aerogels show a peak at 127.9 eV, which corresponds to P from InP (Figure 5.4b). A second peak was

observed for TOPO- capped nanoparticles at around 131.2 eV, corresponding to TOPO on the surface of nanoparticles. In the aerogel, this peak is absent, and a new peak appears at 132.5 eV corresponding to an oxidized form of phosphorus that is distinct from, and in higher formal oxidation state than, the phosphorus in TOPO (Figure 5.4b). The oxidized 'P' species in the aerogel is attributed to the oxidation of surface phosphorus on InP nanoparticles during gelation, as proposed in Figure 5.3b. Thus, XPS data are consistent with the formation of a phosphate/phosphite layer on the surface of nanoparticles during gelation. After the formation of the surface phosphate/phosphite layer, presumbly hydrolysis and condensation would lead to formation of P-O-P bonds between particles. There is no evidence for phosphate/phosphite formation in the PXRD of aerogels, suggesting that any phosphate/phosphite layer formed during gelation is amorphous.
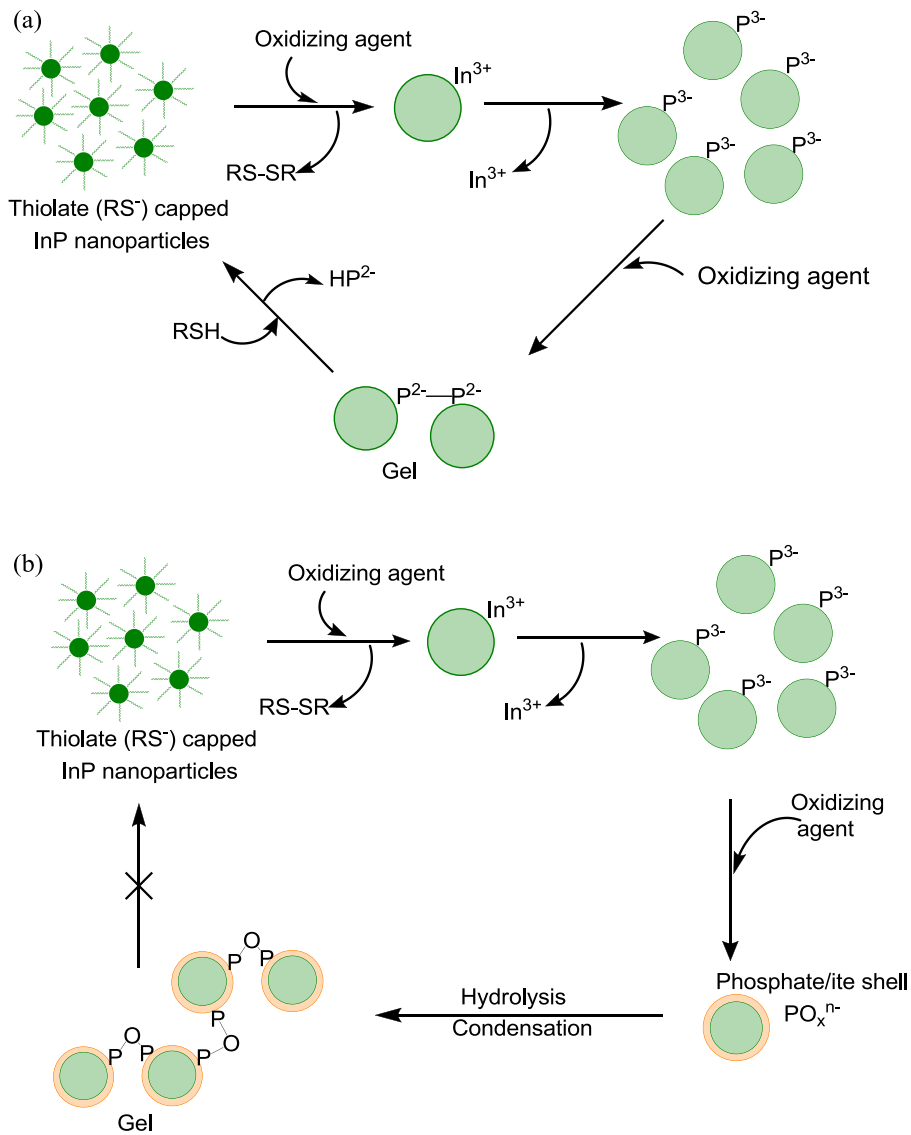
Figure 5.3 (a) Initial hypothesis for metal phosphide gel network formation and (b) modified hypothesis
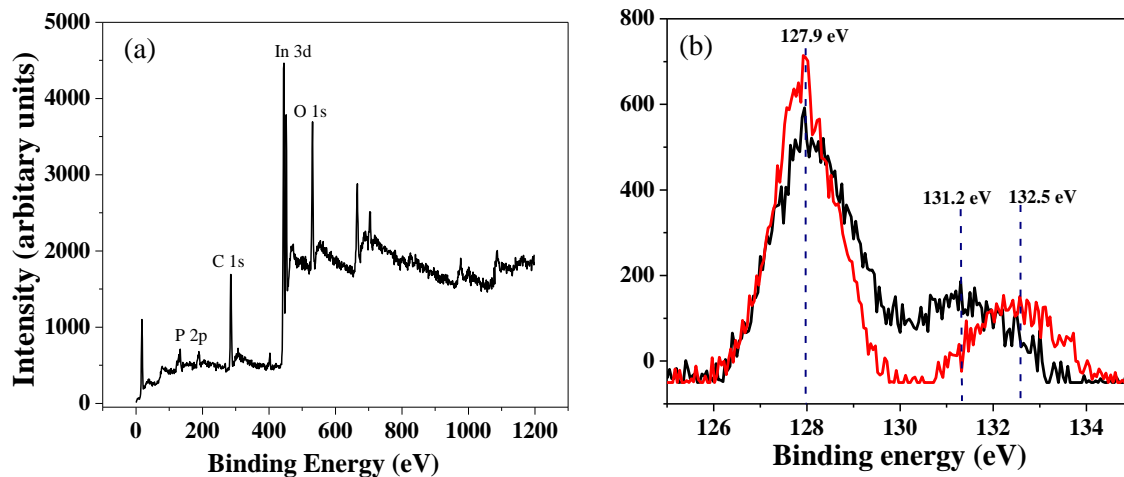
Figure 5.4 (a) XPS survey spectra of (a) AG. (b) High resolution XPS spectrum of the P 2p of TOPO-NP (black) and AG (red)

As a final check of our hypothesis, we considered that, if there are P-P bonds between the nanoparticle components of the aerogel, we should be able to disperse InP aerogels using mild reducing agents such as thiolates or phosphines, which are used for the dispersion of metal chalcogenide aerogels (bond strengths Se-Se < P-P < S-S < P-O). However, metal phosphide gels were not dispersible using MUA or even stronger reducing agents (NaBH$_4$). Therefore, the oxidation–induced metal phosphide gelation mechanism does not involve P-P bond formation and is not reversible, unlike the case for metal chalcogenide gelation.

5.3.2 Ni$_2$P nanoparticles, gels, and aerogels

Ni$_2$P gels were synthesized following the same procedure as for InP, the oxidation induced sol−gel method. Briefly, oleylamine/trioctylphosphine-capped Ni$_2$P were synthesized.[49] The surface ligands were exchanged with a thiolate, 11-mercaptoundeconoic acid (MUA), under basic conditions (pH >10), and then gelled by the addition of an oxidant (H$_2$O$_2$), resulting in the

formation of a black, gelatinous monolith (Figure 5.5). Gelation occurred within 30−60 min, demonstrating that the gelation process noted for InP can be applied to other phosphides, as expected.

Figure 5.5 Pictures of a wet gel (left) and an aerogel (right) prepared via the oxidation-induced route (MUA + H_2O_2). The monolith (right) has a density of ∼0.027 g/cm^3

Presuming that the proposed phosphate/phosphite bridging gelation mechanism noted for InP is also operative for Ni_2P (Figure 5.6, Path 1), we sought to rule out gel formation in the presence of non-oxygen transferring oxidants. Accordingly, tetranitromethane (TNM) was added to a sol of MUA-capped Ni_2P nanoparticles under inert atmosphere. To our surprise, and in direct contrast to observations with InP, a gel was formed with similar rapidity to that produced with H_2O_2 and the TNM gels were visually identical to those gels formed with H_2O_2. However, when MUA is replaced with either 1-dodecanethiolate or 4-fluorothiophenolate capping groups, gels form exclusively with H_2O_2 (Table 5.2); gel formation with TNM is limited to MUA-capped particles. The key difference between the ligands studied is the presence of a pendant carboxylate group in MUA that is absent in 4-fluorothiophenol and 1-dodecanethiol (replaced

with a fluoro or alkyl functionality, respectively). In fact, both S^- and COO^- functionalities of MUA are capable of bonding to Ni^{2+} (based on hard/soft acid/base theory).[130] However, for the sake of simplicity, we have rendered all schematic drawings showing thiolate binding to the particle surface and carboxylate as pendant. Eychmüller and co-workers have shown that metal cross-linking of carboxylates and other chelating terminal groups can lead to gel formation for nanoparticles of metals and metal chalcogenides.[131, 132] Accordingly, we hypothesized that the TNM is not acting as an active oxidant to produce phosphate, but is etching Ni^{2+} ions from the surface in the process of oxidation-induced thiolate decomplexation. ICP-MS analysis confirmed the presence of Ni^{2+} in the supernatant of a wet gel after addition of TNM. These Ni^{2+} ions subsequently act to link together carboxylates (thiolates) in adjoining particles. Divalent transition metals display a strong coordination ability with carboxylate groups. The fact that gel formation due to metal ion cross-linking was not observed for InP may be due to the weak complexation ability of In^{3+} by carboxylates under our gelation conditions and/or minimal etching of In from InP with TNM.[133]

Table 5.2 The effect of capping group on gelation

Capping agent	H_2O_2	TNM	Ni^{2+}
MUA	gel	gel	gel
4-fluorothiophenol	gel	no gel	no gel
1-dodecanethiol	gel	no gel	no gel

To prove that gel formation can occur *via* cross-linking, Ni^{2+} was added to a portion of the MUA-capped Ni_2P sol (Figure 5.6, Path 2). Gels were formed within a relatively short time

depending on the amount of Ni^{2+} added. When the Ni^{2+}: Ni_2P ratio is 1:5, gels were formed within 5-10 min, whereas higher concentrations of Ni^{2+} (Ni^{2+}: Ni_2P >1:5) resulted in the formation of precipitates in 1-3 min (Figure 5.7). The addition of Ni^{2+} into a 4-fluorothiophenolate-capped nanocrystal sol did not yield a precipitate or a gel. The use of ligands with pendant arms featuring coordinating moieties as nanoparticle surface capping groups opens the door to metal-assisted assembly of nanocrystals based on the strong complexation of metal ions by carboxylates, tetrazolates, pyridines, and other functional moieties.[131, 134, 135]
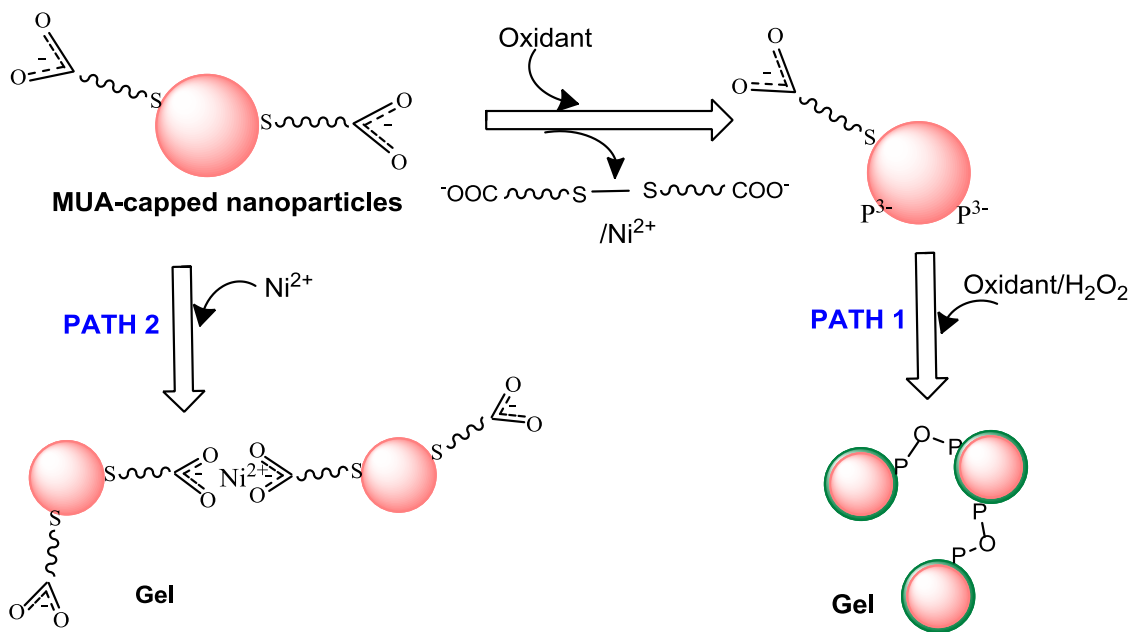
Figure 5.6 Possible gelation pathways for Ni_2P nanoparticles

On the basis of these experiments, there are two possible gelation pathways as shown in Figure 5.6. PATH 1 shows the oxidation-induced sol-gel phosphate/phosphite formation route originally discovered for InP. PATH 2 (metal-assisted gelation) involves cross-linking of the terminal carboxylate (thiolate) groups of MUA by Ni^{2+}. The availability of Ni^{2+} in the solution

due to oxidative etching enables cross-linking of carboxylate (thiolate) groups without the intentional addition of Ni^{2+}.
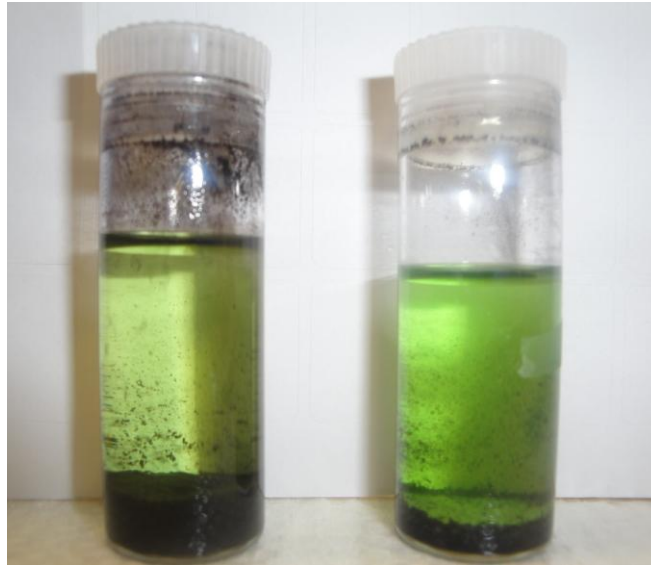
Figure 5.7 Pictures of gels prepared via the metal-assisted route: $Ni^{2+}:Ni_2P = 10:1$ (right) and $Ni^{2+}:Ni_2P^+ = 5:1$ (left)

In order to compare the effect of inter-particle bonding (by phosphate/phosphite or metal-ligand bridging) on the physicochemical properties of the materials, aerogels of MUA-capped Ni_2P were formed by both the traditional oxidation-induced sol-gel method ($MUA+H_2O_2$) and the metal-assisted route (addition of Ni^{2+}, $MUA+Ni^{2+}$). Gels formed via the oxidation-induced sol-gel method remained as monoliths after supercritical drying, however, we were not able to obtain monoliths via the metal-assisted gelation route ($Ni^{2+}: Ni_2P=1:5$). The strongest gel networks were obtained when particles capped with MUA (relative to dodecanethiolate or 4-fluorophenylthiolate) were oxidized by H_2O_2. This may be due to the presence of metal-bridging of the MUA carboxylate functionalities, in addition to oxo-condensation, due to etching of metal

ions from the particle surface during the oxidative gelation process. The presence of multiple cross-linking types (oxo condensation and metal bridging) leads to more robust gel networks.

The powder X-ray diffraction (PXRD) patterns of both kinds of Ni_2P aerogels ($MUA+H_2O_2$ and $MUA+Ni^{2+}$) show the hexagonal crystal structure of the as-prepared (oleylamine/TOP capped) nanocrystals from which they originated (Figure 5.8). The particle sizes were calculated by applying the Scherrer formula to the (111) reflection. The aerogels prepared from the oxidation-induced gelation route ($MUA+H_2O_2$) showed a decrease in crystallite diameter relative to the precursor particles (7.9 ± 0.5 nm vs. 9.0 ± 0.6 nm). This is attributed to oxidation of the particle surface in the process of gel formation, resulting in transformation of the crystalline Ni_2P shell to an amorphous phosphate/phosphite shell. In contrast, an increase in particle size was observed for the aerogels prepared from the metal-assisted gelation method ($MUA+Ni^{2+}$) relative to the precursor particles (10.4 ± 0.7 nm vs 9.0 ± 0.6 nm). This may be due to a ripening process or re-crystallization of amorphous phosphorus on the particle surface with the free metal ions in solution. The increased crystallite radius of 0.7 nm corresponds roughly to addition of a monolayer of Ni_2P on the particle surface (0.5 nm, based on the average unit cell parameter).

Both kinds of aerogels ($MUA+H_2O_2$ and $MUA+Ni^{2+}$) appeared to be morphologically similar to metal oxide and metal chalcogenide aerogels, where particles are interconnected to form a highly porous colloidal network with a broad pore size distribution ranging from microporous (<2 nm), through mesoporous (2-50 nm), and into the macroporous (>50 nm) regime (Figure 5.8). In the $MUA+H_2O_2$ AG the oxidized layer can be seen in the high resolution TEM images (marked in red, Figure 5.9c). In contrast, clear spacing between particles is

observed in aerogels prepared from the metal-assisted route (Figure 5.9d), attributed to a lack of contrast from the ligand linking groups.
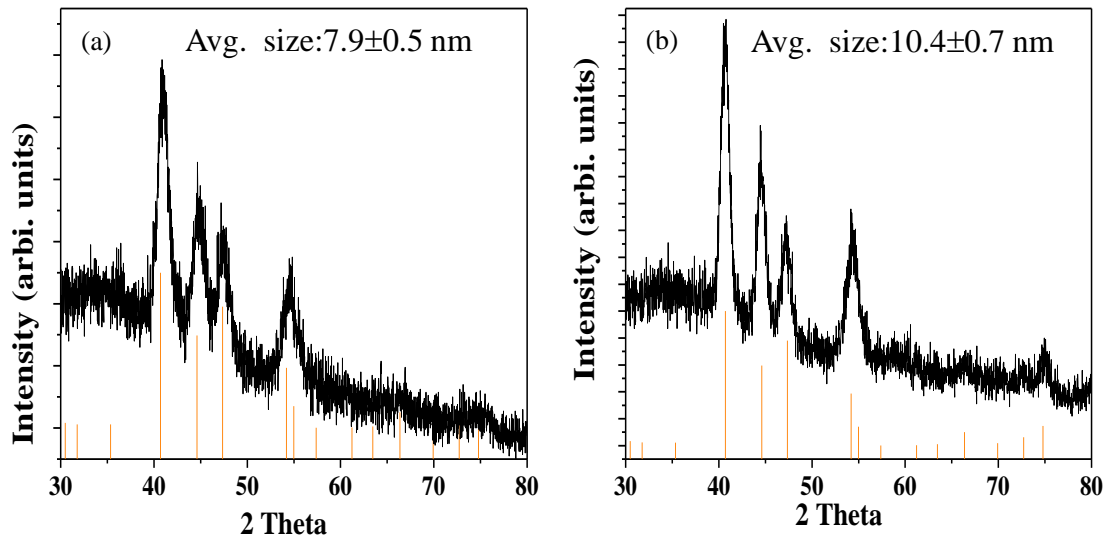
Figure 5.8 PXRD patterns of aerogels: (a) MUA+H_2O_2 AG and (b) MUA+Ni^{2+} AG. The ICDD-PDF overlay of Ni_2P (PDF#74-1385) is shown as vertical lines in (a) and (b)

To further prove that the surface oxidation of nanoparticles is taking place only when H_2O_2 is used as the oxidant, high resolution XPS spectra for nanoparticles and aerogels were collected for the P 2p region, ranging from 125-140 eV (Figure 5.10). Two distinct peaks were observed for as-prepared nanoparticles at 129.9 eV and 133.6 eV. The peak at lower binding energy can be assigned to P from Ni_2P (Figure 5.10a), whereas the peak at 133.6 eV is attributed to the P in trioctylphosphine (presumably residual ligand bound to the particle surface). The peak for Ni_2P can be seen in both kinds of aerogels (Figure 5.10b and c), but the peak intensity is very low for the MUA+H_2O_2 AG. In the MUA+H_2O_2 AG, a relatively intense peak at 134.2 eV is observed (Figure 5.9b) consistent with 'oxidized P' in phosphate (P^{5+}).[136] This suggests the

presence of significant surface oxidation in the MUA + H_2O_2 AG, consistent with the oxidation-induced gelation mechanism. Likewise, the absence of a peak at 134.2 eV in the MUA+Ni^{2+} AG suggests that condensation of phosphate groups is not responsible for gelation in this case (Figure 5.10c).
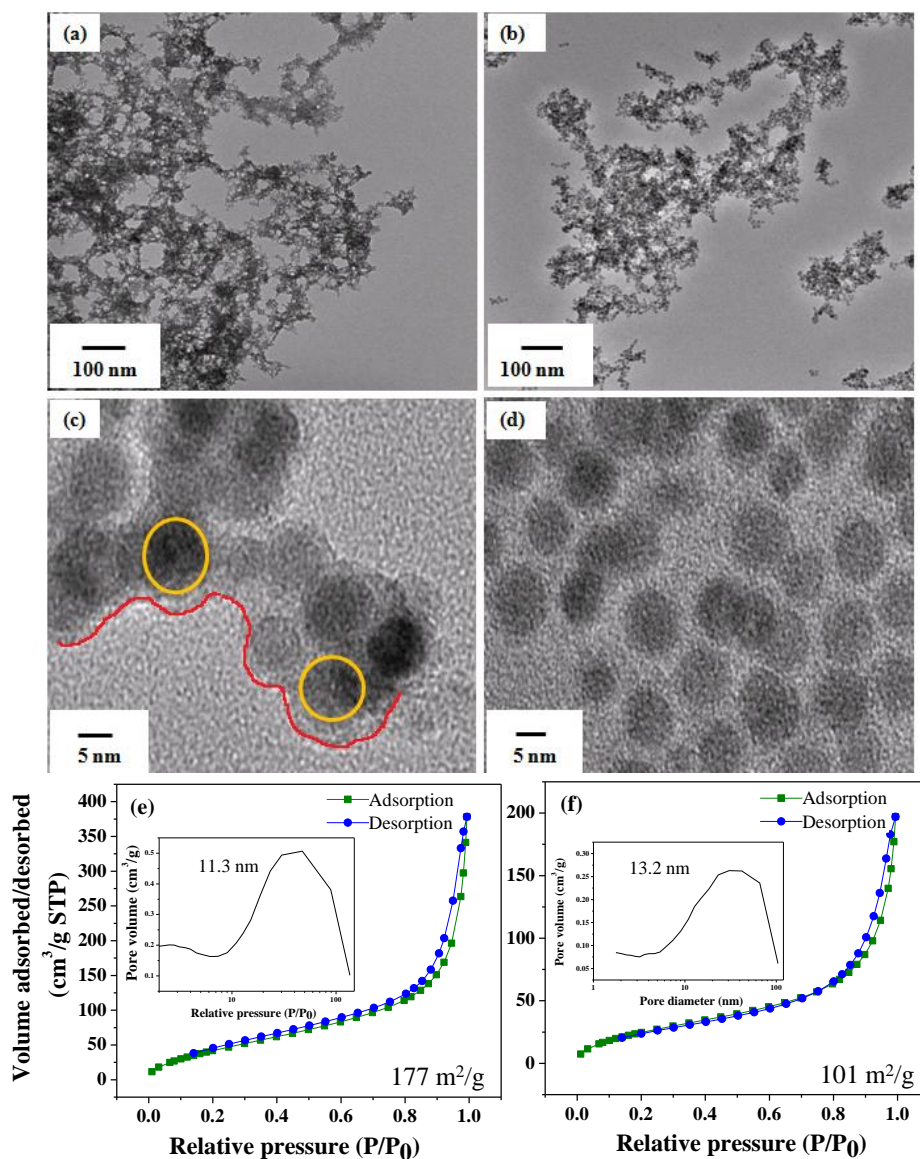
Figure 5.9 TEM micrographs of AGs: (a) MUA+H_2O_2 and (b) MUA+Ni^{2+}; (c) and (d) are high resolution TEM images of MUA+H_2O_2 and MUA+Ni^{2+} AGs, respectively. Nanoparticles are circled in yellow and the oxidized layer is marked in red in image (c). N_2 adsorption/desorption

isotherms of AGs: (e) MUA+H₂O₂ and (f) MUA+Ni^{2+}. The BJH pore size distributions are shown as insets of (e) and (f)
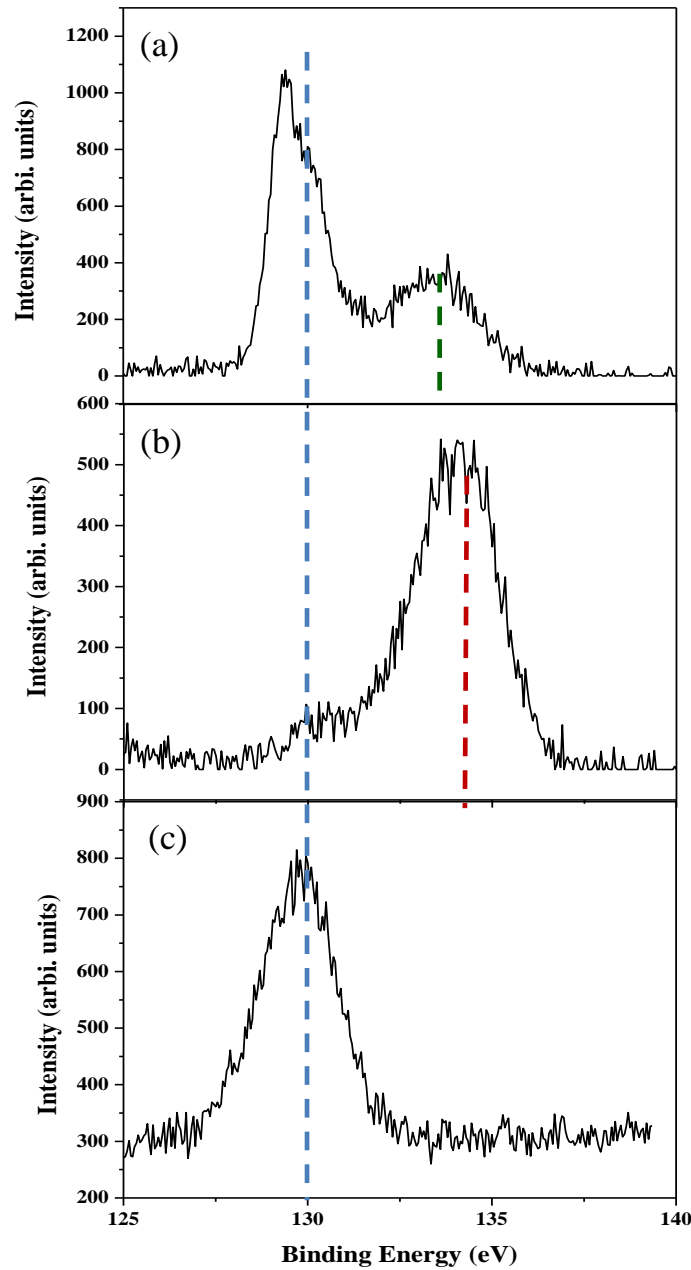
Figure 5.10 High resolution P 2p XPS spectra of (a) as prepared-nanoparticles, (b) MUA+H₂O₂, and (c) MUA+Ni^{2+} AGs

To evaluate the accessibility of Ni_2P aerogels as a function of gelation mechanism, surface area and porosimetry measurements were determined using N_2 physisorption measurements (Figure 5.9e and f). Both kinds of aerogels demonstrated a type IV curve, which is characteristic of a mesoporous material.[112] The oxidation-induced gelation method produced aerogels with surface areas as high as 177 m^2/g. Even though gels formed via the metal assisted route showed lower surface areas (101 m^2/g), they were still greater than those measured for the as-prepared nanoparticles (42 m^2/g). The absence of a pore network limits access to the theoretically high surface area intrinsic to a nanoparticle. The pore size distributions were determined by the Barrett-Joyner-Halenda (BJH) method. Both aerogels showed broad meso (2-50 nm) to macro (>50 nm) pore size distributions (insets of Figure 5.9e and f) with average pore sizes of 11.3 and 13.2 nm respectively, consistent with the morphology observed by TEM.

The concentration of organics (residual ligands) present in the aerogels, and their desorption temperatures, was determined using thermogravimetric analysis (TGA). Both types of aerogels ($MUA+H_2O_2$ and $MUA+Ni^{2+}$) showed weight losses in the range of 350-450 °C, consistent with temperatures noted for organic ligand decomposition in other systems (Figure 5.11). Aerogels produced by the metal-assisted gelation route (PATH 2, Figure 5.6) had a higher weight percentage of organics (25%) relative to those produced by the oxidation-induced gelation route (17%, PATH 1, Figure 5.6). This is not surprising because oxidation-induced gelation involves ligand loss, whereas in the metal-assisted gelation mechanism the ligands are not being removed and are integral to gel formation.
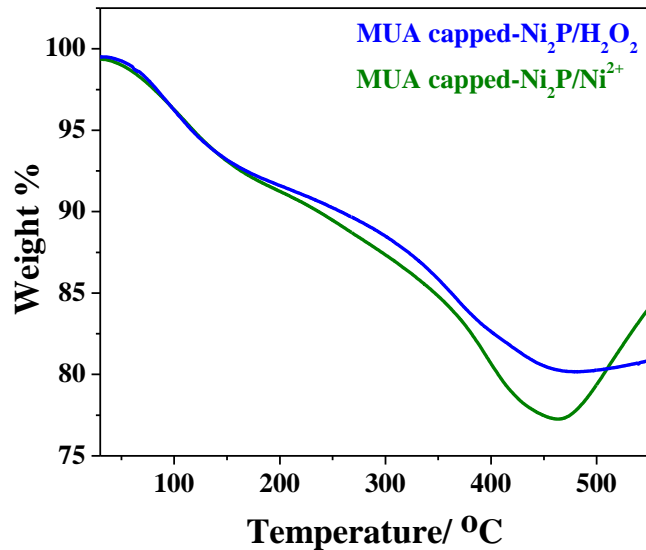
Figure 5.11 Thermogravimetric analyses of aerogels

The presence of a high surface area, interconnected pore structure, and self-supported network is expected to be beneficial for catalysis. However, since hydrotreating catalytic processes are carried out at elevated temperatures, the thermal stability of these materials is a key parameter. To probe the thermal stability of both kinds of aerogels (MUA+H_2O_2 and MUA+Ni^{2+}), *in situ* heating experiments were carried out in the TEM under vacuum. Both kinds of aerogels retained the gel network, even upon heating in vacuum up to 400 °C (Figure 5.12). However, at around 420 °C, aerogels formed in PATH 2 (MUA+Ni^{2+}) started to aggregate, losing the interconnectivity (Figure 5.12 biii and biv). According to TGA data, the decomposition of surface ligands starts near 300 °C and levels off by 450 °C. Since PATH 2 is based on cross-linking of surface bound ligands *via* metal ions, the decomposition of ligands causes the gel network to break down. In contrast, the aerogels formed by oxidation-induced gelation (MUA+H_2O_2), did not start to aggregate until 620 °C (Figure 5.12 aiii and aiv). The high thermal stability of these aerogels can be attributed to their gelation mechanism; in this

case, the gel network is held together by strong P-O-P bonds and the interconnectivity does not depend on the thermal stability of thiolate ligands.
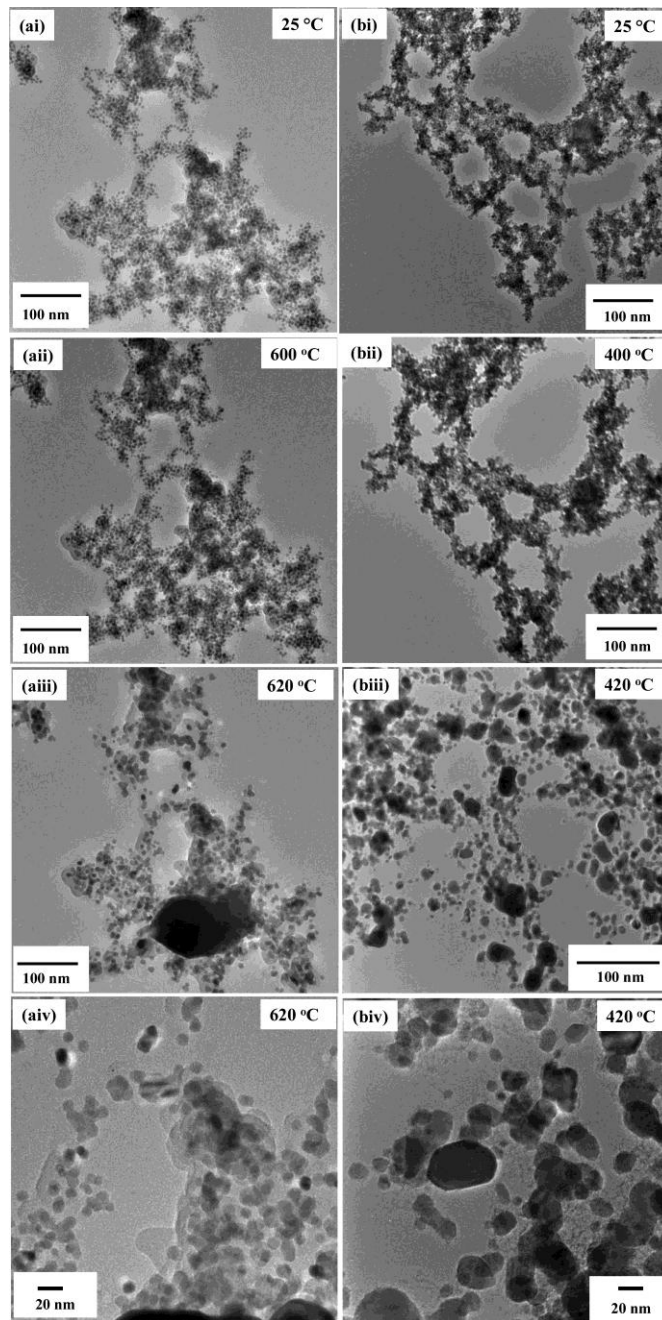
Figure 5.12 TEM micrographs of (a) MUA+H_2O_2 and (b) MUA+Ni^{2+} AGs heated at various temperatures under vacuum in the TEM. (aiv) and (biv) are magnified images of (aiii) and (biii), respectively

5.4 Conclusions

Sol-gel strategies based on nanoparticle assembly, previously established for metal chalcogenides such as CdS and CdSe, can be used to interconnect InP nanoparticles leading to a network in which the extent of quantum confinement is increased relative to precursor nanoparticles. The interconnected 3D architectures of nanoparticles have both meso and macropores, with accessible surface areas of ~200 m^2/g. XPS studies of nanoparticles and aerogels suggest the formation of a surface phosphate/phosphite indicating a gelation mechanism based on phosphorus oxoanion condensation, in contrast to related chalcogenide materials where there is no oxygen incorporation.

Aerogels of Ni$_2$P were prepared by employing the same oxidation-induced gelation method proving the generality of the metal phosphide gelation route *via* phosphate linkages. Since gels formed using non-oxygen transferring oxidants when Ni$_2$P nanocrystals are capped with terminal carboxylate lignds, 3D networks of Ni$_2$P can also be constructed by cross-linking the terminal groups of the surface ligands with Ni^{2+}, providing an alternative gelation mechanism for Ni$_2$P. This simple method, metal-assisted gelation, produced a multi branched interconnected network of nanocrystals similar to those produced from oxidation induced gels. Moreover, metal-assisted gel networks were found to have similar surface areas and pore size distributions to gels formed by the chemical oxidation method.

CHAPTER 6

CONCLUSIONS AND PROSPECTUS[4]

Nanomaterials show distinct catalytic, magnetic, and optoelectronic properties relative to their bulk material counterparts. These properties can be tailored by the varying size and shape depending on the targeted properties of specific applications. Metal phosphides exhibit a wide range of properties including magnetism, catalysis, semiconductivity, the ability to intercalate lithium, and superconductivity.[20, 23, 24, 55, 137] However, as they exist in various stoichiometries and their properties are sensitive to composition, the synthesis of nanoscale metal phosphides is challenging. As a result nanoscale properties of metal phosphides are unexplored compare to metals, metal oxides, and metal chalcogenides. Our group has developed synthetic methods for many metal phosphide nanoparticles including FeP, Fe_2P, Ni_2P, $Ni_{12}P_5$, and MnP.[20, 43, 44, 49] These syntheses enabled the study of their size-dependent properties, including magnetic properties (of interest for magnetic refrigeration and data storage) and catalytic properties. Recently, ternary and quaternary metal phosphide phases have received considerable attention after several reports on improved magnetic and catalytic properties of in these phases.[23, 24, 52, 55] However, there are few reports in the literature of synthesis of discrete ternary and quaternary metal phosphide nanocrystals.[58, 59]

To use nanomaterials in device applications, assembly techniques need to be developed to translate nanoscopic properties into macroscopic "handle-able" materials. It has been demonstrated that the sol-gel method can be used to produce porous high-surface-area interconnected nanoarchitectures while maintaining the inherent properties of the particles. Our group reported the synthesis of metal chalcogenide gels and aerogels that manifested the

---

[4] Portions of the text in this chapter were reprinted or adapted with permission from: *ACS Nano*, 2013, 7, 1163-1170 *and Chem. Mater*. 2014, 26, 6251-6256

characteristic optical properties of their particle components. [85, 95, 97, 99, 101, 102, 138] However, the application of the sol-gel method to metal phosphides has not been reported.

This dissertation was focused on synthesis and characterization of ternary metal phosphide, and assembly of metal phosphide nanoparticles into gels, and aerogels with. Specifically, the two main goals were to (1) develop a synthetic method to prepare ternary $Fe_xNi_{2-x}P$ (where $0<x<2$) phases as well-formed nanocrystals with control of size, shape, and composition to probe the relationship between composition and size on magnetic and catalytic properties and; (2) develop a sol-gel nanoparticle assembly method for metal phosphides; specifically for InP and Ni_2P.

6.1 Synthesis and Characterization of Discrete $Fe_xNi_{2-x}P$ Nanocrystals: Compositional Effects on Magnetic Properties and Dibenzothiophene (DBT) Hydrodesulfurization (HDS) Catalytic Activity

6.1.1 Conclusions

In order to study the magnetic and hydrodesulfurization (HDS) catalytic properties of ternary $Fe_xNi_{2-x}P$ nanocrystals a solution-phase synthetic method to prepare discrete $Fe_xNi_{2-x}P$ nanocrystals was developed. The optimized synthetic conditions for $Fe_xNi_{2-x}P$ ternary nanocrystals over a wide range of compositions ($0<x<2$) are reported in Chapter 3. Phase-pure $Fe_xNi_{2-x}P$ nanocrystals can be synthesized using a three step synthetic method involving: (a) formation of amorphous Ni_xP_y particles at a lower temperature (230 °C), (b) injection of Fe precursor and formation of amorphous Ni-Fe-P particles at 230 °C, and (c) crystallization to form $Fe_xNi_{2-x}P$ at 350 °C. Mössbauer spectroscopy studies of $Fe_xNi_{2-x}P$ nanocrystals revealed that Fe preferentially occupies M(1) sites (tetrahedral sites) when $x<0.8$ relative to the M(2) (square pyramidal sites) in the hexagonal Fe_2P-type crystal structure. The morphology of the

nanocrystals showed a distinct compositional dependence. For $x \leq 1.2$ the resultant spherical nanoparticles have an average particle size ~ 11 nm (less than 10% standard deviation). With the increase in the amount of Fe incorporation, nanocrystals adopt a rod morphology ($x \geq 1.2$) and nanorods showed average rod lengths in the range of 15-19 nm (less than 20% standard deviation). The width of these rods is in the range of 8.5-10.0 nm (less than 15% standard deviation). However, the aspect ratios can be increased by using excess phosphorous precursor. The developed synthetic method enables synthesis of $Fe_xNi_{2-x}P$ nanoparticles with controlled size across all x ($0<x<2$), allowing study of effects of composition on magnetic and catalytic properties of bimetallic FeNi phosphide nanoparticles.

The magnetic properties including the blocking temperature (T_B), Curie temperature (T_C), and hysteresis of $Fe_xNi_{2-x}P$ nanocrystals (x=1.8, 1.4, and 1.2) were aquired. The substitution of Ni into the parent Fe_2P produced an increase in T_C, which reaches a maximum of 265 K at x=1.4, decreasing rapidly with small x. In this study T_C of Fe_2P was improved by 50 K (217 K to 265 K) demonstrating the ability to augment T_C via cation doping.

The preliminary dibenzothiophene (DBT) HDS catalytic activity measurements of Ni-rich $Fe_xNi_{2-x}P$ (x=0.03, 0.1, 0.2, and 0.3) ternary nanocrystals were carried out and reported in Chapter 4. As prepared $Fe_xNi_{2-x}P$ nanocrystals were encapsulated in mesoporous silica to prevent sintering during the catalytic measurements. Composition dependent catalytic activity of $Fe_xNi_{2-x}P@mSiO_2$ was observed. $Fe_{0.1}Ni_{1.9}P@mSiO_2$ showed a similar catalytic activity as $Ni_2P@mSiO_2$ whereas other compositions had lower activities. With the exception of $Fe_{0.03}Ni_{1.9}7P@mSiO_2$ which showed an anomalously low activity these $Fe_xNi_{2-x}P@mSiO_2$ catalysts mimic the behavior TPR prepared $Fe_xNi_{2-x}P/SiO_2$ catalysts suggesting that discrete nanoparticles of $Fe_xNi_{2-x}P$, when encapsulated in mesoporous silica, are useful HDS model

catalyst system. This part of the dissertation work lays the foundation for studying size and composition-dependent HDS catalytic activity of $Fe_xNi_{2-x}P@mSiO_2$ nanocrystals.

6.1.2 Prospectus

A similar approach to that we used for $Fe_xNi_{2-x}P$ nanoparticle synthesis can be applied toward preparing nanoparticles of other ternary (e.g. $Mn_xFe_{2-x}P$ and $Co_xFe_{2-x}P$) and quaternary (e.g. $Mn_xFe_{2-x}As_yP_{1-y}$) phosphide phases. To evaluate the possible use of $Fe_xNi_{2-x}P$ nanocrystals in magnetic refrigeration applications, the magnetocaloric effects of these nanocrystals will be studied. In bulk phases the incorporation of Si and B into the Fe_2P crystal structure has shown augmented T_C relevant to the parent compound Fe_2P.[69] $Fe_xNi_{2-x}P$ can be used as a model to synthesize $Fe_xNi_{2-x}D_yP_{1-y}$ (D=B and Si) nanocrystals and evaluate their magnetic properties as a function of x and y.

X-ray photoelectron spectroscopy (XPS) and chemisorption measurements of $Fe_xNi_{2-x}P$ materials are underway to correlate the surface composition of materials to their HDS performance. To further evaluate the catalytic properties of our ternary nanocrystals, HDS measurements of sterically bulky DBT (4, 6-dimethyldibenzothiophene) are underway. Moreover, because $Fe_{0.03}Ni_{1.97}P/SiO_2$ prepared by the TPR method showed a higher catalytic activity than optimized Ni_2P/SiO_2 testing the HDS activity of this composition is prioritized. The HDS catalytic activity of silica encapsulated ternary nanocrystals can be further improved by reducing the thickness of the silica shell (which will reduce the mean free-pathway of reactants). This will be an avenue of future investigations.

6.2 Formation of Gels and Aerogels of Phosphides

6.2.1 Conclusions

The aim of this part of the dissertation research project was to study the applicability of the sol-gel nanoparticle assembly method that has proven to be robust for a range of metal chalcogenides, to metal phosphides; specifically for InP and Ni_2P. The successful application of the sol-gel methodology to the assembly of discrete nanoparticles of InP and Ni_2P to form aerogels is reported in Chapter 5.

InP aerogel synthesis involves solution-phase synthesis of InP nanoparticles, surface capping with a thiolate ligand, oxidative decomplexation, oxidation-induced gel formation, and supercritical drying of wet gels to obtain aerogels. The interconnected 3D architectures of InP nanoparticles have both meso- and macropores, with accessible surface areas above 200 m^2g^{-1}. InP aerogels showed higher band gap values relative to precursor nanoparticles, an indication of greater quantum confinement suggesting that during the process of assembling nanoparticles into 3D architectures, particle size reduction may have taken place. In contrast to metal chalcogenide gelation, InP gels did not form using tetranitromethane (TNM), a non-oxygen-transferring oxidant. The requirement of an oxygen-transferring oxidant, combined with X-ray photoelectron spectroscopy data showing oxidized phosphorous, suggests gelation is occurring due to condensation of phosphorous oxoanionic moieties generated at the interface. The ability to connect InP nanoparticles through inorganic linkages while maintaining their nanoscopic properties is beneficial where efficient charge transfer between nanoparticles is essential.

Aerogels of Ni_2P were prepared by employing the same oxidation-induced gelation method reported for InP aerogel formation, proving the generality of the metal phosphide gelation route via phosphate linkages. In direct contrast to InP, gels were formed using non-

oxygen-transferring oxidants when Ni_2P nanoparticles are capped with ligands that have pendant carboxylate or thiolate functionalities, suggesting that three dimensional networks of Ni_2P can also be constructed by crosslinking the terminal groups of the surface ligands with Ni^{2+}, providing an alternative gelation mechanism for Ni_2P. Moreover, metal assisted gel networks were found to have surface areas and pore size distributions similar to those of gels formed by the chemical oxidation method. The good thermal stability combined with a large surface area and the interconnected nanostructure of Ni_2P aerogels make these desirable candidates for HDS, water-gas-shift (WGS) reaction, and hydrogen evolution reaction (HER) catalysis.

6.2.2 Prospectus

The high surface area and interconnected pore structure suggest these aerogel materials may be useful in applications such as catalysis and hybrid photovoltaics. Future studies probing post modification strategies to remove oxygen from the interfaces without compromising the network should be carried out to demonstrate the applications of this new class of materials. Because phosphates and phosphites can be reduced to phosphides in a H_2 flow at ~500 °C,[9] and the Ni_2P aerogels prepared via the oxidative sol-gel method are thermally stable above 600 °C, future work should be focused on reducing the oxidation layer at the interface while maintaining matter-pore connectivity.

APPENDIX A

CHARACTERIZATION DATA OF SILICA ENCAPSULATED FE$_{2-X}$NI$_X$P

SAMPLES

Table A1. Compositions and sample loadings of Fe$_x$Ni$_{2-x}$P@mSiO$_2$

Sample	EDS composition	ICP-MS composition	Sample loading (from ICP-MS)
WWU-AB1	Ni$_2$P	Ni$_2$P	9.2
WWU-AB2	Fe$_{0.05}$Ni$_{1.95}$P	Fe$_{0.03}$Ni$_{1.97}$P	7.5
WWU-AB3	Fe$_{0.2}$Ni$_{1.8}$P	Fe$_{0.15}$Ni$_{1.85}$P	10.7
WWU-AB4	Fe$_{0.3}$Ni$_{1.7}$P	Fe$_{0.27}$Ni$_{1.73}$P	9.0
WWU-AB5	Fe$_{0.5}$Ni$_{1.5}$P	Fe$_{0.46}$Ni$_{1.54}$P	7.4
WWU-AB6	Fe$_{0.7}$Ni$_{1.3}$P	Fe$_{0.63}$Ni$_{1.37}$P	11.1
WWU-AB7	Fe$_{1.0}$Ni$_{1.0}$P	Fe$_{0.76}$Ni$_{1.24}$P	11.1

Table A2. BET surface areas and average pore sizes of Fe$_x$Ni$_{2-x}$P@mSiO$_2$

Sample	BET surface area (m^2/g)	Average pore diameter (nm)
WWU-AB1	510	6.7
WWU-AB2	670	4.8
WWU-AB3	602	4.9
WWU-AB4	583	4.7
WWU-AB5	571	4.8
WWU-AB6	662	5.1
WWU-AB7	612	5.3
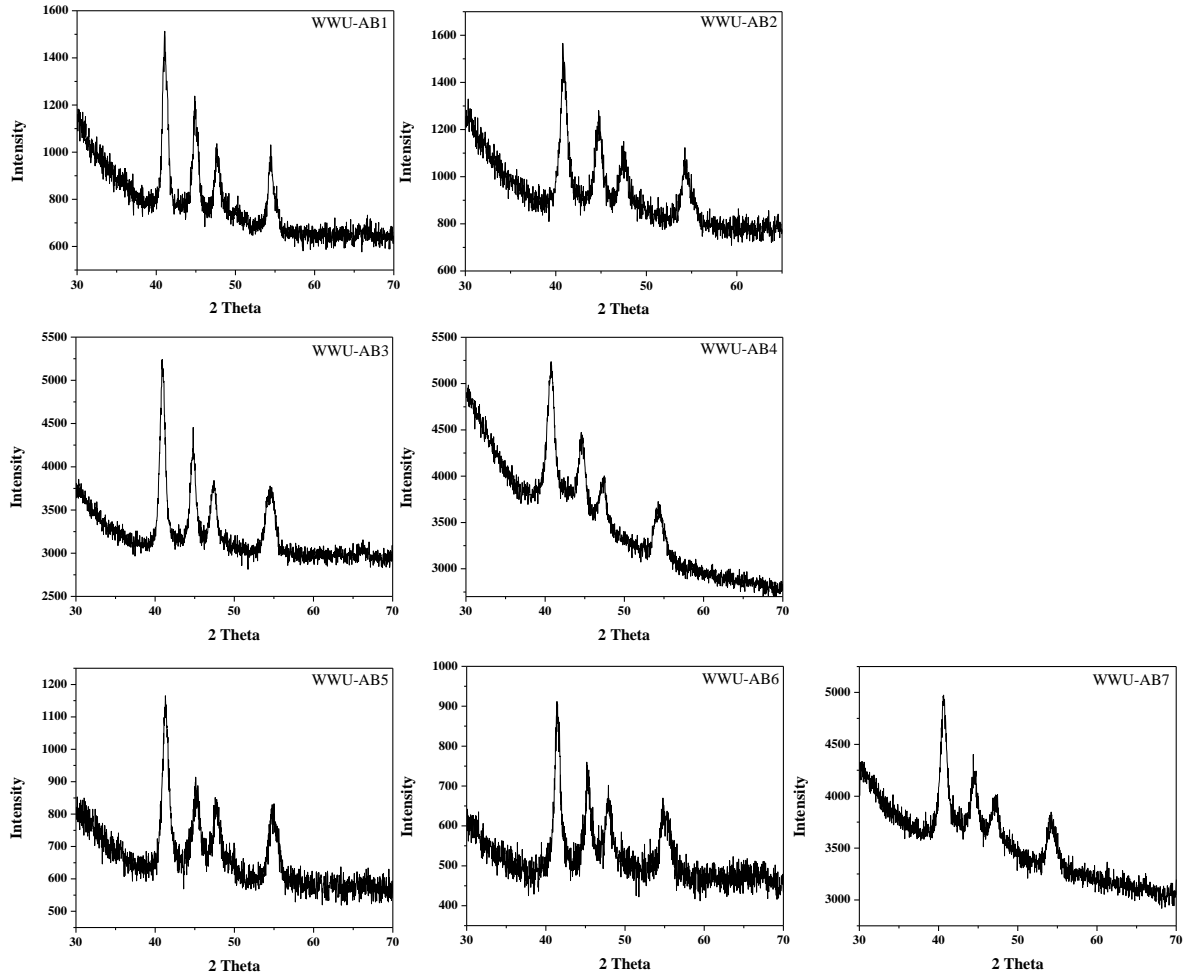
Figure A1. PXRD patterns of $Fe_xNi_{2-x}P@mSiO_2$
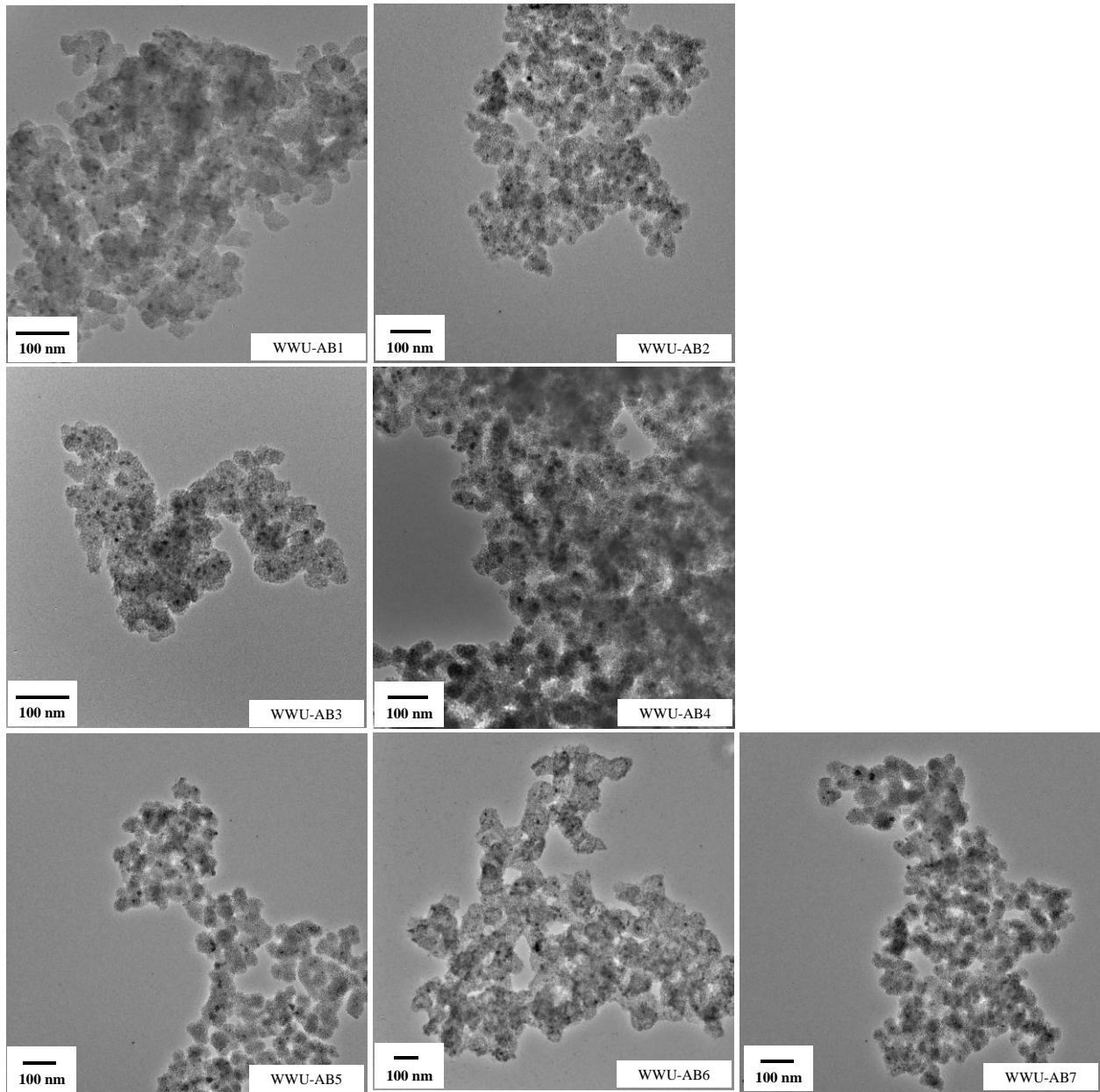
Figure A2. TEM micrographs of $Fe_xNi_{2-x}P@mSiO_2$

APPENDIX B

PERMISSION/LICENCE AGREEMENT FOR COPYRIGHT MATERIALS

Copyright Clearance Center

RightsLink®

JOURNAL OF CATALYSIS

Title:	Mössbauer spectroscopy investigation and hydrodesulfurization properties of iron–nickel phosphide catalysts	Logged in as: Asha Mudiyanselage Account #: 3000848864
Author:	Amy F. Gaudette,Autumn W. Burns,John R. Hayes,Mica C. Smith,Richard H. Bowker,Takele Seda,Mark E. Bussell	**LOGOUT**
Publication:	Journal of Catalysis	
Publisher:	Elsevier	
Date:	25 May 2010	

Copyright © 2010 Elsevier Inc. All rights reserved.

Order Completed

Thank you very much for your order.

This is a License Agreement between Asha Mudiyanselage ("You") and Elsevier ("Elsevier"). The license consists of your order details, the terms and conditions provided by Elsevier, and the payment terms and conditions..

License Number	3507480575352
License date	Nov 14, 2014
Licensed content publisher	Elsevier
Licensed content publication	Journal of Catalysis
Licensed content title	Mössbauer spectroscopy investigation and hydrodesulfurization properties of iron–nickel phosphide catalysts
Licensed content author	Amy F. Gaudette,Autumn W. Burns,John R. Hayes,Mica C. Smith,Richard H. Bowker,Takele Seda,Mark E. Bussell
Licensed content date	25 May 2010
Licensed content volume number	272
Licensed content issue number	1
Number of pages	10
Type of Use	reuse in a thesis/dissertation
Portion	figures/tables/illustrations
Number of figures/tables/illustrations	1
Format	both print and electronic
Are you the author of this Elsevier article?	No

Will you be translating?	No
Title of your thesis/dissertation	SYNTHESIS AND CHARACTERIZATION OF DISCRETE Fe2-xNixP NANOCRYSTALS; ASSEMBLY OF PHOSPHIDE NANOPARTICLES INTO POROUS NETWORKS
Expected completion date	Dec 2014
Estimated size (number of pages)	100
Elsevier VAT number	GB 494 6272 12

JOHN WILEY AND SONS LICENSE
TERMS AND CONDITIONS

Nov 06, 2014

This is a License Agreement between Asha Mudiyanselage ("You") and John Wiley and Sons ("John Wiley and Sons") provided by Copyright Clearance Center ("CCC"). The license consists of your order details, the terms and conditions provided by John Wiley and Sons, and the payment terms and conditions.

All payments must be made in full to CCC. For payment instructions, please see information listed at the bottom of this form.

License Number	3503140270650
License date	Nov 06, 2014
Licensed content publisher	John Wiley and Sons
Licensed content publication	Angewandte Chemie International Edition
Licensed content title	Reversible Gelation of II–VI Nanocrystals: The Nature of Interparticle Bonding and the Origin of Nanocrystal Photochemical Instability
Licensed copyright line	Copyright © 2010 WILEY-VCH Verlag GmbH & Co. KGaA, Weinheim
Licensed content author	Irina R. Pala,Indika U. Arachchige,Daniel G. Georgiev,Stephanie L. Brock
Licensed content date	Apr 9, 2010
Start page	3661
End page	3665
Type of use	Dissertation/Thesis
Requestor type	University/Academic
Format	Print and electronic
Portion	Figure/table
Number of figures/tables	1
Original Wiley figure/table number(s)	Scheme 1
Will you be translating?	No
Title of your thesis / dissertation	SYNTHESIS AND CHARACTERIZATION OF DISCRETE Fe2-xNixP NANOCRYSTALS; ASSEMBLY OF PHOSPHIDE NANOPARTICLES INTO POROUS NETWORKS
Expected completion date	Dec 2014

Copyright Clearance Center

RightsLink®

ACS Publications Most Trusted. Most Cited. Most Read.

Title: Bottom-Up Assembly of Ni2P Nanoparticles into Three-Dimensional Architectures: An Alternative Mechanism for Phosphide Gelation

Author: Asha Hitihami-Mudiyanselage, Keerthi Senevirathne, Stephanie L. Brock

Publication: Chemistry of Materials

Publisher: American Chemical Society

Date: Oct 1, 2014

Copyright © 2014, American Chemical Society

Logged in as:

Asha Mudiyanselage

Account #: 3000848864

LOGOUT

PERMISSION/LICENSE IS GRANTED FOR YOUR ORDER AT NO CHARGE

This type of permission/license, instead of the standard Terms & Conditions, is sent to you because no fee is being charged for your order. Please note the following:

- Permission is granted for your request in both print and electronic formats, and translations.
- If figures and/or tables were requested, they may be adapted or used in part.
- Please print this page for your records and send a copy of it to your publisher/graduate school.
- Appropriate credit for the requested material should be given as follows: "Reprinted (adapted) with permission from (COMPLETE REFERENCE CITATION). Copyright (YEAR) American Chemical Society." Insert appropriate information in place of the capitalized words.
- One-time permission is granted only for the use specified in your request. No additional uses are granted (such as derivative works or other editions). For any other uses, please submit a new request.

Copyright Clearance Center

RightsLink®

ACS Publications
Most Trusted. Most Cited. Most Read.

Title: Assembly of Phosphide Nanocrystals into Porous Networks: Formation of InP Gels and Aerogels

Author: Asha Hitihami-Mudiyanselage, Keerthi Senevirathne, Stephanie L. Brock

Publication: ACS Nano

Publisher: American Chemical Society

Date: Feb 1, 2013

Copyright © 2013, American Chemical Society

Logged in as:

Asha Mudiyanselage

Account #:
3000848864

LOGOUT

PERMISSION/LICENSE IS GRANTED FOR YOUR ORDER AT NO CHARGE

This type of permission/license, instead of the standard Terms & Conditions, is sent to you because no fee is being charged for your order. Please note the following:

- Permission is granted for your request in both print and electronic formats, and translations.
- If figures and/or tables were requested, they may be adapted or used in part.
- Please print this page for your records and send a copy of it to your publisher/graduate school.
- Appropriate credit for the requested material should be given as follows: "Reprinted (adapted) with permission from (COMPLETE REFERENCE CITATION). Copyright (YEAR) American Chemical Society." Insert appropriate information in place of the capitalized words.
- One-time permission is granted only for the use specified in your request. No additional uses are granted (such as derivative works or other editions). For any other uses, please submit a new request.

ELSEVIER LICENSE
TERMS AND CONDITIONS

Nov 25, 2014

This is a License Agreement between Asha Mudiyanselage ("You") and Elsevier ("Elsevier") provided by Copyright Clearance Center ("CCC"). The license consists of your order details, the terms and conditions provided by Elsevier, and the payment terms and conditions.

All payments must be made in full to CCC. For payment instructions, please see information listed at the bottom of this form.

Supplier	Elsevier Limited The Boulevard,Langford Lane Kidlington,Oxford,OX5 1GB,UK
Registered Company Number	1982084
Customer name	Asha Mudiyanselage
Customer address	4727 Anthony Wayne Dr DETROIT, MI 48201
License number	3515520979762
License date	Nov 24, 2014
Licensed content publisher	Elsevier
Licensed content publication	Journal of Catalysis
Licensed content title	Unprecedented selectivity to the direct desulfurization (DDS) pathway in a highly active FeNi bimetallic phosphide catalyst
Licensed content author	S. Ted Oyama,Haiyan Zhao,Hans-Joachim Freund,Kiyotaka Asakura,Radosław Włodarczyk,Marek Sierka
Licensed content date	January 2012
Licensed content volume number	285
Licensed content issue number	1
Number of pages	5
Start Page	1
End Page	5
Type of Use	reuse in a thesis/dissertation
Intended publisher of new work	other

REFERENCES

1.   Huynh, W. U.; Dittmer, J. J.; Alivisatos, A. P. *Science* 2002, 295, 2425-2427.

2.   Liu, J.; Tanaka, T.; Sivula, K.; Alivisatos, A. P.; Fréchet, J. M. J. *J. Am. Chem. Soc.* 2004, 126, 6550-6551.

3.   Eustis, S.; El-Sayed, M. A. *Chem. Soc. Rev.* 2006, 35, 209-217.

4.   Alivisatos, A. P. *The J. Phys. Chem.* 1996, 100, 13226-13239.

5.   Freesone, I.; Meeks, N.; Sax, M.; Higgitt, C. *Gold Bull.* 2007, 40, 270-277.

6.   Gaudette, A. F.; Burns, A. W.; Hayes, J. R.; Smith, M. C.; Seda, T.; Bussell, M. E. *J. Catal.* 2010, 272, 18-27.

7.   Fruchart, R.; Roger, A.; Senateur, J. P. *J. Appl. Phys.* 1969, 40, 1250-1257.

8.   Oyama, S., Ted; Gott, T.; Zhao, H.; Lee, Y.-K. *Catal. Today* 2009, 143, 94-107.

9.   Prins, R.; Bussel, M. E. *Catal. Lett.* 2012, 142, 1413-1436.

10.   Nozaki, F.; Adachi, R. *J. Catal.* 1975, 40, 166-172.

11.   Zuzaniuk, V.; Prins, R. *J. Catal.* 2003, 219, 85-96.

12.   Muetterties, E. L.; Sauer, J. C. *J. Am. Chem. Soc.* 1974, 96, 3410-3415.

13.   Goldstein, A. N.; Echer, C. M.; Alivisatos, A. P. *Science* 1992, 256, 1425-1427.

14.   Tolbert, S. H.; Alivisatos, A. P. *Annu. Rev. Phys. Chem.* 1995, 46, 595-626.

15.   Savithra, G. H.; Muthuswamy, E.; Bowker, R. H.; Carrillo, B. A.; Bussell, M. E.; Brock, S. L. *Chem. Mater.* 2013, 25, 825-833.

16.   Rosi, N. L.; Mirkin, C. A. *Chem. Rev.* 2005, 105, 1547-1562.

17.   Leslie-Pelecky, D. L.; Rieke, R. D. *Chem. Mater.* 1996, 8, 1770-1783.

18.   Brus, L. *J. Phys. Chem.* 1986, 90, 2555-2560.

19.   Talapin, D. V.; Lee, J.-S.; Kovalenko, M. V.; Shevchenko, E. V. *Chem. Rev.* 2009, 110,

389-458.

20.   Muthuswamy, E.; Kharel, P. R.; Lawes, G.; Brock, S. L. *ACS Nano* 2009, 3, 2383-2393.

21.   Senevirathne, K.; Burns, A. W.; Bussell, M. E.; Brock, S. L. *Adv. Funct. Mater.* 2007, 17,

3933-3939.

22.   Klimov, V. I. *Marcel Dekker, Inc.* 2004.

23.   Abu, I. I.; Smith, K. J. *J. Catl.* 2006, 214, 356.

24.   Balli, M.; Fruchart, D.; Gignoux, D.; Tobola, J.; Hlil, E. K.; Wolfers, P.; Zach, R. *J. Mag.

Mag. Mater.* 2007, 316, 358-360.

25.   Barz, H.; Ku, H. C.; Meisner, G. P.; Fisk, Z.; Matthias, B. T. *Proc. Natl. Acad. Sci.* 1980,

77, 3132-3134.

26.   Gaudette, A. F.; Burns, A. W.; Hayes, J. R.; Smith, M. C.; Boewker, R. H. *J. Catl* 2010,

272, 18-27.

27.   Gregg, K. A.; Perera, S. C.; Lawes, G.; Shinozaki, S.; Brock, S. L. *Chem. Mater.* 2006,

18, 879-886.

28.   Henkes, A. E.; Schaak, R. E. *Inorg. Chem* 2008, 48, 671-677.

29.   Jasinski, J.; Leppert, V. J.; Lam, S.-T.; Gibson, G. A.; Nauka, K.; Yang, C. C.; Zhang-

Lin, Z. *Solid State Commun.* 2007, 141, 624-627.

30.   Mine, T.; Yanagi, H.; Kamiya, T. *Solid State Commun.* 2008, 147, 111-113.

31.   Muthuswamy, E.; Brock, S. L. *ACS Nano* 2009, 3, 2383-2393.

32.   Park, J. K.; Koo, B.; Hwang, Y.; Bae, C. J.; An, K.; Park, J.-G.; Park, H. M.; Hyeon, T.

Angew. Chem. Int. Ed. 2004, 43, 2282-2285.

33.   Paul, C.; Li, W.; Oyama, S. T. J. C., 200, 140. *J. Catal.* 2011, 200.

34.   Perera, S. C.; Tsoi, G.; Wenger, L. E.; Brock, S. L. *J. Am. Chem. Soc* 2003, 125, 13960-13961.

35.   Rotello, V. *Nanoparticles: Building Blocks for Nanotechnology*. Springer: 2004.

36.   Franco, V.; Blazquez, J. S.; Ingale, B.; Conde, A. *Annual Review of Material Research* 2012, 42, 305-342.

37.   Carenco, S.; Portehault, D.; Boissière, C.; Mézailles, N.; Sanchez, C. Nanoscaled Metal Borides and Phosphides: Recent Developments and Perspectives. *Chem. Rev.* 2013, 113, 7981-8065.

38.   Sharon, M.; Tamizhmani, G. *Journal of Materials Science* 1986, 21, 2193-2201.

39.   Trindade, T.; O'Brien, P.; Pickett, N. L. *Chem. Mater.* 2001, 13, 3843-3858.

40.   Panneerselvam, A.; Malik, M. A.; Afzaal, M.; O'Brien, P.; Helliwell, M. *J. Am. Chem. Soc.* 2008, 130, 2420-2421.

41.   Liu, C.; Dai, L.; You, L. P.; Xu, W. J.; Ma, R. M.; Yang, W. Q.; Zhang, Y. F.; Qin, G. G. *J. Mater. Chem.* 2008, 18, 3912-3914.

42.   George, P. P.; Pol, V. G.; Gedanken, A. *J. Nanoparticle Res.* 2007, 9, 1187-1193.

43.   Perera, S. C.; Fodor, P. S.; Tsoi, G. M.; Wenger, L. E.; Brock, S. L. *Chem. Mater.* 2003, 15, 4034-4038.

44.   Perera, S. C.; Tsoi, G.; Wenger, L. E.; Brock, S. L. *J. Am. Chem. Soc.* 2003, 125, 13960-13961.

45.   Park, J.; Koo, B.; Hwang, Y.; Bae, C.; An, K.; Park, J. G.; Park, H. M.; Hyeon, T. *Angew. Chem.* 2004, 116, 2332-2335.

46.   Park, J.; Koo, B.; Yoon, K. Y.; Hwang, Y.; Kang, M.; Park, J.-G.; Hyeon, T. *J. Am. Chem. Soc.* 2005, 127, 8433-8440.

47.   Henkes, A. E.; Vasquez, Y.; Schaak, R. E. *J. Am. Chem. Soc.* 2007, 129, 1896-1897.

48.   Henkes, A. E.; Schaak, R. E. *Chem. Mater.* 2007, 19, 4234-4232.

49.   Muthuswamy, E.; Savithra, G.; Brock, S. L. *ACS Nano* 2011, 5, 2402-2411.

50.   Carenco, S.; Boissere, C.; Nicole, L.; Sanchez, C.; Le Floch, P.; Mezailles, N. *Chem. Mater.* 2010, 22, 1340-1349.

51.   Brück, E.; Tegus, O.; Zhang, L.; Li, X. W.; de Boer, F. R.; Buschow, K. H. J. *J. Alloys Compd.* 2004, 383, 32-36.

52.   Brück, E.; Tegus, O.; Thanh, D. T. C.; Buschow, K. H. J. *J. Magn. Magn. Mater.* 2007, 310, 2793-2799.

53.   Brück, E.; Ilyn, M.; Tishin, A. M.; Tegus, O. *J. Magn. Magn. Mater.* 2005, 290–291, Part 1, 8-13.

54.   Tegus, O.; Brück, E.; Li, X. W.; Zhang, L.; Dagula, W.; Boer, F. R. d.; Buschow, K. H. J. *J. Magn. Magn. Mater.* 2004, 272–276, Part 3, 2389-2390.

55.   Gaudette, A. F.; Burns, A. W.; Hayes, J. R.; Smith, M. C.; Bowker, R. H.; Seda, T.; Bussell, M. E. *J. Catal.* 2010, 272, 18-27.

56.   Burns, A. W.; Gaudette, A. F.; Bussell, M. E. *J. Catal.* 2008, 260, 262-269.

57.   Balli, M.; Fruchart, D.; Gignoux, D.; Tobola, J.; Hlil, E. K.; Wolfers, P.; Zach, R. *J. Mag. Mag. Mater.* 2007, 316, 358-360.

58.   Yoon, K. Y.; Jang, Y.; Park, J.; Hwang, Y.; Koo, B.; Park, J.-G.; Hyeon, T. *J. Solid State Chem.* 2008, 181, 1609-1613.

59.   Colson, A. C.; Whitmire, K. H. *Chem. Mater.* 2011, 23, 3731-3739.

60.   West, A. R. Basic Solid State Chemistry. August 2000, 2nd Edition.

61.   Gregg, K. A.; Perera, S. C.; Lawes, G.; Shinozaki, S.; Brock, S. L. *Chem. Mater.* 2006, 18, 879-886.

62.   Phan, M.-H.; Yu, S.-C. *J. Magn. Magn. Mater.* 2007, 308, 325-340.

63.   Brock, S., L.; Perera, S.; Stamm, K. L. *Chem. - A Eur. J.* 2004, 10, 3364-3371.

64.   Feichter, S.; Tributsch, H.; Evain, M.; Brec, R. *Mater. Res. Bull.* 1987, 22, 543-549.

65.   Blanchard, P. E. R.; Grosvenor, A. P.; Cavell, R. G.; Mar, A. *Chem. Mater.* 2008, 20, 7081-7088.

66.   Grosvenor, A. P.; Cavell, R. G.; Mar, A. Bonding and Electronic Structure of Phosphides, Arsenides and Antimonides by X-ray Photoelectron Spectroscopy. In Structure and Bonding. *Springer: Berlin* 2009.

67.   Dagula, W.; Tegus, O.; Li, X. W.; Song, L.; Brück, E.; Cam Thanh, D. T.; de Boer, F. R.; Buschow, K. H. J. *J. Appl. Phys.* 2006, 99.

68.   Caron, L.; Hudl, M.; Dung, N. H.; Gomez, C. P.; Sahlberg, M.; Bruck, E.; Andersson, Y.; Nordblad, P. *Phys. Rev. B* 2013, 88, 094440.

69.   Delczeg-Czirjak, E. K.; Bergqvist, L.; Eriksson, O.; Gercsi, Z.; Nordblad, P.; Szunyogh, L.; Johansson, B.; Vitos, L. *Phys. Rev. B* 2012, 86, 045126.

70.   Zach, R.; Toboła, J.; Średniawa, B.; Kaprzyk, S.; Casado, C.; Bacmann, M.; Fruchart, D. *J. Alloys Compd.* 2004, 383, 322-327.

71.   Kumar, S.; Krishnamurthi, a.; Srivastava, B. K.; Paranjpe, S. K. *J. Phys.: Condens. Matter* 2007, 19, 196217.

72.   Goodenough, J. B. *J. Solid State Chem.* 1973, 7, 428.

73.   Oyama, T. S.; Zhao, H.; Freund, H.-J.; Asakura, K.; Wlodarczyk, R.; Sierka, M. *J. Catal.* 2012, 285, 1-5.

74.   Dolia, S. N.; Krishnamurthi, A.; Ghose, V.; Srivastava, B. K. *J. Phys.: Condens. Matter* 1993, 5, 451-458.

75.   Lo, C.-T.; Kuo, P.-Y. *J. Phys. Chem. C* 2010, 114, 4808-4815.

76.   Pawlec, B.; Navarro, R. M.; Cam Thanh, D. T.; Fierro, J. L. G. *Catal. Sci. & Techno.* 2011, 1, 23-42.

77.   Topsøe, H.; Clausen, B.; Massoth, F. E. Hydrotreating Catalysis, In Catalysis: Science and Technology. *Springer-Verlag Berlin* 1996, 11, 1-300.

78.   Topsøe, H. The role of Co–Mo–S type structures in hydrotreating catalysts. *Applied Catalysis A: General* 2007, 322, 3-8.

79.   Li, K.; Wang, R.; Chen, J. *Energy & Fuels* 2011, 25, 854-863.

80.   Popczun, E. J.; McKone, J. R.; Read, C. G.; Biacchi, A. J.; Wiltrout, A. M.; Lewis, N. S.; Schaak, R. E. *J. Am. Chem. Soc.* 2013, 135, 9267-9270.

81.   Oyama, S. T. *J. Catal.* 2003, 216, 343-352.

82.   Ted Oyama, S.; Zhao, H.; Freund, H.-J.; Asakura, K.; Włodarczyk, R.; Sierka, M. *J. Catal.* 2012, 285, 1-5.

83.   Sawhill, S. J.; Layman, K. A.; Van Wyk, D. R.; Engelhard, M. H.; Wang, C.; Bussell, M. E. T*J. Catal.* 2005, 231, 300-313.

84.   Wang, L.; Xu, L.; Kuang, H.; Xu, C.; Kotov, N. A. *Acc. Chem. Res.* 2011, 45, 1916-1926.

85.   Mohanan, J. L.; Arachchige, I. U.; Brock, S. L. *Science* 2005, 307, 397-400.

86.   Grzelczak, M.; Vermant, J.; Furst, E. M.; Liz-Marzán, L. M. *ACS Nano* 2010, 4, 3591-3605.

87.   Shavel, A.; Gaponik, N.; Eychmüller, A. *Eur. J. Inorg. Chem.* 2005, 2005, 3613-3623.

88.	Srivastava, S.; Kotov, N. A. *Acc. Chem. Res.* 2008, 41, 1831-1841.

89.	Murray, C. B.; Kagan, C. R.; Bawendi, M. G. *Annu. Rev. Mater. Sci.* 2000, 30, 545-610.

90.	Kistler, S. S. *Nature* 1931, 127, 741.

91.	Hüsing, N.; Schuber, U. *Angew. Chem. Int. Ed.* 1998, 37, 22–45.

92.	Rolison, D. R.; Long, J. W.; Lytle, J. C.; Fischer, A. E.; Rhodes, C. P.; McEvoy, T. M.; Bourga, M. E.; Lubersa, A. M. *Chem. Soc. Rev.* 2009, 38, 226-252.

93.	Pierre, A.; Pajonk, G. M. *Chem. Rev.* 2002, 102, 4243-4265.

94.	Gacoin, T.; Mailier, L.; Boilot, J.-P. *Chem. Mater.* 1997, 9, 1502-1504.

95.	Mohanan, J. L.; Brock, S. L. *J. Non-Cryst. Solids* 2004, 350, 1-8.

96.	Pala, I. R.; Arachchige, I. U.; Georgiev, D. G.; Brock, S. L. *ngew. Chem. Int. Ed.* 2010, 49, 3661-3665.

97.	Ganguly, S.; Brock, S. L. *J. Mater. Chem.* 2011, 21, 8800-8806.

98.	Yao, Q.; Brock, S. L. *Nanotechnology* 2010, 21, 115502.

99.	Yao, Q.; Brock, S. L. *Inorg. Chem.* 2011, 50, 9985-9992.

100.	Arachchige, I. U.; Brock, S. L. *Acc. Chem. Res* 2007, 40, 801-809.

101.	Pala, I. R.; Brock, S. L. *ACS Applied Materials & Interfaces* 2012, 4, 2160-2167.

102.	Ganguly, S.; Zhou, C.; Morelli, D.; Sakamoto, J.; Brock, S. L. *J. Phys. Chem. C* 2012, 116, 17431-17439.

103.	Yu, B. F.; Gao, Q.; Zhang, B.; Meng, X. Z.; Chen, Z. *Int. J. Refrig.* 2003, 26, 622-636.

104.	Warburg, E. *Ann Physics* 1881, 13, 141-164.

105.	Phan, M.-H.; Yu, S.-C. *J.Mag. Mag. Mater.* 2007, 308, 325-340.

106.	Tegus, O.; Bruck, E.; Buschow, K. H. J.; de Boer, F. R. *Nature* 2002, 415, 150-152.

107.	Goodenough, J. B. *J. Appl. Phys.* 1969, 40, 12501258.

108. Ninh, T. K. T.; Massin, L.; Laurenti, D.; Vrinat, M. *Appl. Catal. A: General* 2011, 407, 29-39.

109. Williams, D. B.; Carter, C. B. Transmission Electron Microscopy. *Springer* 2010, 2nd Volume.

110. Fultz, B.; Howe, J. Transmission Electron Microscopy and Diffractometry of Materials. *Springer* 2000.

111. Gregg, S. J.; Sing, K. S. W. Adsorption, Surface Area and Porosity. *Academic Press* 1982, 2nd Edition.

112. Webb, P. A.; Orr, C. Analytical Methods in Fine Particle Technology. *Micromeritics Instrument Corporation* 1997.

113. Skoog, D. A.; Holler, F. J.; Nieman, T. A. *Principles of Instrumental Analysis*. Brooks?Cole: New York, 1998; Vol. 5.

114. Clarke, J.; Braginski, A. I. The SQUID Handbook Vol. I Fundamentals and Technology of SQUIDs and SQUID systems. *Wiley VCH* 2004.

115. Savithra, G. H. L.; Muthuswamy, E.; Bowker, R. H.; Carrillo, B.; Bussell, M. E.; Brock, S. L. *Chem. Mater.* 2013, 25, 825-833.

116. Webb, P. A.; Orr, C. *Analytical Methods in Fine Particle Technology*. 1997.

117. Pekala, R. W. *J. Mater. Sci.* 1989, 24, 3221-3227.

118. King, J. S.; Wittstock, A.; Biener, J.; Kucheyev, S. O.; Wang, Y. M.; Baumann, T. F.; Giri, S. K.; Hamza, A. V.; Baeumer, M.; Bent, S. F. *Nano Lett.* 2008, 8, 2405-2409.

119. Worsley, M. A.; Pauzauskie, P. J.; Olson, T. Y.; Biener, J.; Satcher, J. H.; Baumann, T. F. *J. Am. Chem. Soc.* 2010, 132, 14067-14069.

120. Mulik, S.; Sotiriou-Leventis, C.; Leventis, N. *Chem. Mater.* 2007, 19, 6138-6144.

121.   Yao, Q.; Arachchige, I. U.; Brock, S. L. *J. Am. Chem. Soc.* 2009, 131, 2800.

122.   Hitihami-Mudiyanselage, A.; Senevirathne, K.; Brock, S. L. *ACS Nano* 2013, 7, 1163-1170.

123.   Hitihami-Mudiyanselage, A.; Senevirathne, K.; Brock, S. L. *Chem. Mater.* 2014, 26, 6251-6256.

124.   Hoffmann, R.; Zheng, C. *J. Phys. Chem* 1985, 89, 4175-4181.

125.   Senevirathne, K. Wayne State University, Detoir, 2008.

126.   Arachchige, I. U.; Brock., S. L. *J. Am. Chem. Soc* 2006, 128, 7964-7971.

127.   Araujo, C.; Zhang, L.; Eckert, H. *J. Mater. Chem* 2006, 16, 1323-1331.

128.   Zhang, L.; Eckert, H. *J. Mater. Chem.* 2004, 14, 1605-1615.

129.   Evans, B. H.; Doi, J. T.; Musker, W. K. *J. Org. Chem* 1990, 55, 2337-2344.

130.   Pearson, R. G. *J. Am. Chem. Soc.* 1963, 85, 3533.

131.   Lesnyak, V.; Voitekhovich, S. V.; Gaponik, P. N.; Gaponik, N.; Eychmüller, A. *ACS Nano* 2010, 4, 4090-4096.

132.   Lesnyak, V.; Wolf, A.; Dubavik, A.; Voitekhovich, S. V.; Gaponik, N.; Kaskel, S.; Eychmüller, A. *J. Am. Chem. Soc.* 2011, 133.

133.   Lin, Z.; Chen, L.; Jiang, F.; hong, M. *Inorg. Chem. Commun.* 2005, 8.

134.   Chen, S.; Pei, R. *J. Am. Chem. Soc.* 2001, 123, 10607.

135.   Zamborini, F.; Hicks, J.; Murray, R. W. *J. Am. Chem. Soc.* 2000, 122, 4514.

136.   J., S. S.; Layman, K. A.; Wyk, D. R.; Engelhard, M. H.; Wang, C.; Bussell, M. E. *J. Catal.* 2005, 231, 300-313.

137.   Senevirathne, K.; Burns, A. W.; Bussel, M. E.; Brock, S. L. *Adv. Funct. Mater.* 2007, 17, 3933-3939.

138.   Kalebaila, K. G.; Brock, S. L. *J. Non-Crystalline Solids* 2006, 352, 232-240.

ABSTRACT

SYNTHESIS AND CHARACTERIZATION OF DISCRETE FE$_X$NI$_{2-X}$P NANOPARTICLES; ASSEMBLY OF PHOSPHIDE NANOPARTICLES INTO POROUS NETWORKS

by

ASHA HITIHAMI MUDIYANSELAGE

May 2015

Advisor: Dr. Stephanie L. Brock

Major :   Chemistry

Degree :   Doctor of Philosophy

This dissertation research is focused on synthesis, characterization and assembly of metal phosphide nanoparticles of relevance to catalysis, magnetism, and optoelectronic applications. These include (1) synthesis of discrete $Fe_xNi_{2-x}P$ ternary nanocrystals of relevance to hydrodesulfurization (HDS) catalysis and magnetism, and (2) 3-dimensional nanostructures (gels and aerogels) of InP and Ni_2P.

A three-step solution-phase arrested precipitation method was employed for bimetallic nanocrystal synthesis. The synthesis of nanocrystals involves preparation of amorphous Ni_xP_y amorphous particles, introduction of the Fe precursor to form amorphous Fe-Ni-P particles, and high temperature conversion of Fe-Ni-P particles into crystalline ternary phosphide nanocrystals. Ternary $Fe_xNi_{2-x}P$ nanocrystals crystalize in the hexagonal Fe_2P-type structure and the morphology of the nanocrystals showed a distinct compositional dependence. With the increase in the amount of Fe incorporation ($x \geq 1.2$), nanocrystals transition from a sphere to a rod morphology. Likewise, as the Fe content of the ternary phosphide phase increases, more polydisperse samples are produced. Magnetic measurements of $Fe_xNi_{2-x}P$ (x=1.8, 1.4, and 1.2)

phases were carried out to determine the blocking temperature (T_B) and Curie temperature (T_C). Both T_B and T_C showed composition-dependence and the highest T_B (200 K) and T_C (265 K) were observed when x=1.4. Preliminary dibenzothiophene (DBT) HDS activity of mesoporous silica encapsulated (to prevent sintering) $Fe_xNi_{2-x}P$ ($Fe_xNi_{2-x}P@mSiO_2$) was also investigated. $Fe_xNi_{2-x}P@mSiO_2$ (x=0.03, 0.1, 0.2, and 0.3) showed composition dependent catalytic activity. The phase $Fe_{0.1}Ni_{1.9}P_{1.1}@mSiO_2$ showed similar catalytic activity to $Ni_2P@mSiO_2$, whereas all other compositions demonstrated lower DBT HDS activities.

The applicability of sol gel nanoparticle assembly routes, previously employed for metal chalcogenides, to phosphides is reported for the case of InP and Ni_2P. With respect to InP gelation, two different sizes (3.5 and 6.0 nm) of InP nanoparticles were synthesized by solution-phase arrested precipitation, capped with thiolate ligands, and oxidized with H_2O_2 to induce gel formation. The gels were aged, solvent-exchanged, and then supercritically dried to obtain aerogels with both meso- (2-50 nm) and macropores (>50 nm); surface areas of ~200 m^2/g can be achieved. InP aerogels showed higher band gap values relative to precursor nanoparticles, suggesting that during the process of assembling nanoparticles into 3D architectures, particle size reduction may have taken place. In contrast to metal chalcogenide gelation, InP gels did not form using tetranitromethane, a non-oxygen-transferring oxidant. The requirement of an oxygen-transferring oxidant, combined with X-ray photoelectron spectroscopy data showing oxidized phosphorus, suggests gelation is occurring due to condensation of phosphorus oxoanionic moieties generated at the interfaces. In addition to the oxidative sol gel method, for Ni_2P gel formation a second method, metal-assisted gelation was developed. Gelation occurs by cross-linking of pendant carboxylate or thiolate functionalities on surface-bound thiolate ligands via metal ions to yield an interconnected particle network. Metal assisted gel networks were found to

have surface areas and pore size distributions similar to those of gels formed by the chemical oxidation method. The method of gel network formation can be tuned by changing the surface ligand terminal functionalities and the nature (oxygen-transferring or non-oxygen transferring) of the oxidant. Both methods produce porous, high surface area materials with thermal stabilities above 400 °C.

AUTOBIOGRAPHICAL STATEMENT

ASHA HITIHAMI MUDIYANSELAGE

Education
- **2009-2014 Ph. D**., Inorganic Chemistry Wayne State University, Detroit, MI
Dissertation: "Synthesis and Characterization of Discrete $Fe_xNi_{2-x}P$
Nanoparticles; Assembly of Phosphide Nanoparticles into Porous Networks"
Advisor: Dr. Stephanie L. Brock
- **2001-2006 B. S.** in Chemistry (Hons.) University of Sri Jayewardenepura, Colombo, Sri Lanka

Research Skills
- Air-free (Schlenk line), glove box and sol-gel synthesis techniques, Supercritical CO_2 extraction, Powder X-ray diffraction, Transmission electron microscopy, Thermogravimetric analysis, Surface area analysis and porosimetry, Energy dispersive spectroscopy (EDS), UV-Visible, PL, FT-IR

Research and Teaching Experience
- **08/2011 – 08/2014** Graduate Research Assistant, Wayne State University, Detroit, MI
- **08/2009 – 08/2011** Graduate Teaching Assistant, Wayne State University, Detroit, MI

Publications

A. Hitihami-Mudiyanselage, K. Senevirathne, S. L. Brock *Chem. Mater,* **2014**, *26(21),* 6251-6256.

A. Hitihami-Mudiyanselage, K. Senevirathne, S. L. Brock *ACS Nano* **2013**, *7 (2),* 1163–1170.

A. Hitihami Mudiyanselage, M. Palihawadana Arachchige, T. Seda, G. Lawes, S. L. Brock *Manuscript in preparation*, **2014**.

Affiliations
- American Chemical Society—Member
- Phi Lambda Upsilon (Chemistry Honor Society)

Awards
Graduate Student/Professional Travel Award, Wayne State University – 2014
Thomas Rumble Fellowship, Wayne State University – 2013
Summer Dissertation Fellowship, Wayne State University – 2013
Prof. Tuley de Silva Gold Medal, University of Sri Jayewardenepura – 2006
Chemical Industries (Colombo) Ltd. Prize, University of Sri Jayewardenepura – 2006
Chemical Industries (Colombo) Ltd. Prize, University of Sri Jayewardenepura – 2005